A Description of Midlatitudes Eddies within the Moist Isentropic Meridional Circulation

by

Frédéric Laliberté

A dissertation submitted in partial fulfillment

of the requirements for the degree of

Doctor of Philosophy

Department of Mathematics

New York University

January 2011

Professor Olivier Pauluis

à Catherine

Acknowledgements

I would like to thank Lorenzo Polvani and Olivier Pauluis, my advisor, for their ongoing support throughout the years. I want to especially acknowledge the numerous hours spent by Tiffany Shaw reading preliminary versions of this thesis. I also credit Edwin Gerber for suggestions that greatly improved the final thesis. Finally, I express my gratitude to Esteban Tabak for all the time he devoted to me in the early years of my doctoral training.

Many other people provided invaluable support. Diogo Arsénio for his presence in tough times, Emmanuel Schertzer for his friendship, Caroline Muller for her thoughtful advices, Louis-Philippe Nadeau for always being available, Jean-Franǫis Lemieux for bearing with me, Agnieszka Smith-Moroviec for listening to my presentations, Shane Keating for his sense of humor and Carl Gladish for his refreshing devotion to bouldering. I would also like to acknowledge Bruno Tremblay and McGill University for hosting me during the summer 2010.

This work could not have been accomplished without the support of national laboratories, international collaboration efforts and governmental agencies that made available the necessary data, models and funding. I credit the Computational and Information Systems Laboratory (CISL) at the National Center for Atmospheric Research (NCAR) for providing the ECMWF ERA40 and NCEP I Reanalysis data. I also thank the Geophysical Fluid Dynamics Laboratory (GFDL) for making available the Atmospheric Dynamical Core used in chapter 3. I acknowledge the modeling groups, the Program for Climate Model Diagnosis and Intercomparison (PCMDI)

and the WCRP's Working Group on Coupled Modelling (WGCM) for their roles in making available the WCRP CMIP3 multi-model dataset. Finally, I am indebted to the McCracken Fellowship program from the New York University and by the NSERC/CRSNG doctoral fellowship program from the Canadian government for their financial support throughout the years.

J'aimerais remercier mes parents, Renée et Jean-Guy, ma soeur Julie, mon filleul Émile et ma nièce Adèle pour m'avoir soutenu dans mes incessants déplacements. Finalement, je dois souligner la patience de Catherine, sans qui certains obstacles auraient peut-être eu raison de moi. Merci.

Preface

The study of the meridional overturning circulation is a fascinating subject. Its goal, understand how heat and momentum are transported poleward from the tropical regions, is fairly simple in essence. Because of the Hadley cell predominantly laminar structure, tropical fluxes are simple to conceive: surface air converges in the equatorial regions, convects then diverges at higher altitudes and finally subsides in the subtropics. In midlatitudes, such a simple flow description does not exist since the turbulent nature of the midlatitudes atmosphere makes any similar zonal-mean analysis useless. One must therefore resort to techniques that are not supported by simple physical interpretations. The majority of those techniques consider the atmosphere dry and adding moisture has often proved to be an elusive endeavor. In this thesis, a moist analysis of the meridional overturning circulation, as proposed by Pauluis et al. (2008), is simplified and explained, conferring it a stronger physical footing. The physical interpretations we develop require the concept of the isentropic mass flux joint distribution, which is an extension of the isentropic mass flux discussed by (Held and Schneider, 1999; Schneider et al., 2006).

In chapter 1, we introduce the meridional overturning circulation with a broad overview of the field. We recall some of the important milestones in the understanding of meridional transports of mass, momentum and energy. We also offer a review of different methods for quantifying the meridional overturning circulation. Finally, we present the moist thermodynamics framework needed for the analyses presented in this thesis.

In chapter 2, we decompose the joint distribution using a method that

differentiates poleward and equatorward air masses according to their moisture content. This method is then used to formulate a simple theory linking surface temperature statistics to the midlatitudes average moist vertical stability. Several concepts introduced in this chapter form a basis for the remainder of this thesis. In concurrent work with Tiffany Shaw, a number of observations from this chapter were used to develop a simplified algorithm designed to compute the moist and dry isentropic circulation. We do not present this algorithm but describe the framework that justifies the approximations presented in that concurrent work.

In chapter 3, we describe idealized moist life-cycle experiments that are used to study the signature of an isolated baroclinic eddy on the mass flux joint distribution. These controlled experiments relate eddies dynamics to characteristics of the dry and moist isentropic circulations. This chapter is the result of collaborative work with Lorenzo Polvani and is built upon his previous studies of the life cycle of dry baroclinic eddies.

In chapter 4, we apply the analysis presented by Pauluis et al. (2010a) to quantify changes in isentropic circulations for the A1B global warming scenario. We also put to use the tools developed in chapter 2 to analyze changes in the model-averaged isentropic mass flux joint distribution. In this chapter, we focus on the climate evolution from the twentieth century to the twenty-first century and produce climate predictions based on bulk measures of midlatitudes eddy activity.

Finally, in chapter 5, we discuss our results and describe their impact for our understanding of current and future climates. Suggestions by the author for future work on the subject are presented.

Abstract

Using a joint isentropic analysis, a theory of the meridional overturning circulation is developed. Our method is based on a careful treatment of the mass flux joint distribution, a quantity that records meridional mass fluxes according to their potential temperature and their equivalent potential temperature simultaneously. This approach reveals mass fluxes that would otherwise be impossible to retrieve with previously available methods. Moreover, it creates as a by-product a completely new diagnostic for the vertical profile of equivalent potential temperature in midlatitudes. These vertical profiles are unusual in that they represent the atmospheric state that is experienced by poleward and equatorward fluxes independently. While poleward fluxes are subjected to a moist atmosphere with slanted moist isentropes, equatorward fluxes experience a dry atmosphere with moist isentropes confounded with dry isentropes. Using these diagnostics, we unify the circulation on dry isentropes with the circulation on moist isentropes by identifying the mass fluxes related to midlatitudes moist ascents. In the process of unifying the two, we propose a moist theory of lower tropospheric dynamic that, when viewed in the context of strong moist ascents, gives an explanation for the midlatitudes moist stratification.

This theory is applied to the study of moist baroclinic eddies using idealized moist life-cycle experiments. We compute the cumulative mass flux joint distribution for a series of individual eddies and use it to describe transports of mass and heat. We relate the moist circulation strength to the amount of available moisture and show that by increasing the depth or relative humidity of a surface moist layer we are increasing the mass fluxes

associated with moist ascents. It is further shown that these added mass fluxes correspond to an increase in eddy kinetic energy in the breaking region of the underlying long wave.

Based on these observations, we apply similar diagnostics to model outputs of the A1B global warming scenario. We describe effects of surface warming on the isentropic circulations and conclude that winter mass fluxes associated with moist ascents could strengthen so much that they could overcome the weakening of the dry circulation during the northern winter.

Table of Contents

Dedication iv

Acknowledgements v

Preface vii

Abstract ix

List of Figures xiii

List of Tables xvi

List of Appendices xvii

1 Introduction **1**

1.1 Statement of the Problem 1

1.2 Meridional Overturning Circulation 9

1.3 Moist Thermodynamics 20

2 Simplified Analysis of the Joint Distribution on Dry Isentropes **39**

2.1 Context 39

2.2 Isentropic Circulations 42

2.3 Simplified Mass Flux Joint Distribution 49

2.4 Moist Isentropic Circulation 67

2.5 Moist Eddies and Low-Level Flows 73

2.6 Summary 83

3 Idealized Moist Life Cycles **87**

3.1 Context 87

3.2 Experimental Setting 92

3.3 Moist Life Cycles 103

3.4 Isentropic Circulations 111

3.5 Summary 141

4 Moist Eddies in a Global Warming Scenario **146**

4.1 Context 146

4.2 Analysis 149

4.3 Results 156

4.4 Summary 175

5 Conclusion **178**

5.1 Discussion 178

5.2 Future Work 183

Appendices **185**

Bibliography **197**

List of Figures

1.1 Eulerian-mean circulation 10

1.2 Transformed eulerian-mean circulation 14

1.3 JJA Isentropic circulations 19

2.1 Joint Distribution and Directional Fluxes for DJF at $\phi = 35°$N. 45

2.2 Dry isentropic circulation for DJF and JJA 46

2.3 DJF Mass fluxes on potential temperature surfaces 51

2.4 JJA Mass fluxes on potential temperature surfaces 52

2.5 DJF Equivalent potential temperature on directional fluxes . 60

2.6 JJA Equivalent potential temperature on directional fluxes . 61

2.7 Diagram explaining moist ascents 63

2.8 Comparison between $\overline{\theta_e}^*$ and $\frac{1}{2}(\langle\theta_e\rangle^+ + \langle\theta_e\rangle^-)$ 64

2.9 Circulations on moist isentropes: exact and folded 70

2.10 Total mass transport on moist isentropes: exact and folded . 71

2.11 Diagram for surface model 76

2.12 Lower tropospheric joint distribution for DJF at $\phi = 35°$N . 77

2.13 Comparison between directional θ_e variability and θ_e variance on dry isentropes 80

3.1 Typical initial conditions 101
3.2 Dry PV on $\theta_l = 310$K 104
3.3 ρ_{θ_l} on $\theta_l = 310$K 105
3.4 θ_e on $\theta = 310$K 106
3.5 Comparison of circulation on dry isentropes 114
3.6 Zonal-mean dry isentropic layer thickness 115
3.7 Moist circulation for $\mathcal{H}_{\max} = 60\%$ 117
3.8 Zonal-mean moist isentropic density 119
3.9 Dry and moist circulations for changing $\mathcal{H}_{\max}$. 122
3.10 Dry and moist Circulations for changing $\bar{z}$ 124
3.11 Legend 129
3.12 Comparison between entropy fluxes and isentropic circulation strength. 130
3.13 Recirculation and EKE on dry isentropes for changing $\mathcal{H}_{\max}$ 131
3.14 Recirculation and EKE on dry isentropes for changing $\bar{z}$ . . . 132
3.15 Stastistics 135
3.16 Comparison between the maximum EKE poleward θ_e and the maximum MR poleward θ_e 138
3.17 Comparison between the MR and EKE 140

4.1 Legend for Figure 4.2 to Figure 4.5 156
4.2 Relative changes in the dry transport 160
4.3 Relative changes in the moist branch transport 161
4.4 Relative changes in the MR 163
4.5 Relative changes in the total transport. 165
4.6 Changes in the model average dry circulation 167

4.7 Changes in the model average moist circulation 168
4.8 Changes in directional fluxes 171
4.9a DJF Changes in directional θ_e 172
4.9b JJA Changes in directional θ_e 174

List of Tables

2.1 List of functions 43
2.2 List of symbols 44

3.1 Physical parameters 93
3.2 Moist layer depth parameters 100
3.3 Simulations parameters for chapter 3 102

4.1 List of analyzed models with daily output 150
4.2 Summary of statistics from Figure 4.2, Figure 4.3, Figure 4.4 and Figure 4.5 157

List of Appendices

Appendix A

Computing the Joint Distribution 186

Appendix B

Baroclinic Initialization 192

Chapter 1

Introduction

1.1 Statement of the Problem

1.1.1 Historical Background

The subject of this thesis, the study of momentum, heat and water vapor transports from the equatorial to the polar regions, is as old as the field of climatology itself. It was in 1735 that Hadley stated for the first time the problem within a proper physical framework. He recognized the importance of momentum conservation to explain the trade winds and postulated the existence of a hemisphere-wide overturning cell with air rising in the equatorial regions and subsiding in the polar regions. This postulate was actually wrong since it turned out that the overturning cell did not extend beyond the subtropics. His error was a result of his inaccurate thinking in terms of linear momentum instead of angular momentum. Had he done so, he would have realized that the flow corresponding to such a large cell necessitated far too large zonal velocities in the midlatitude regions.

It was more than a century later, in 1856, that Ferrel argued for the first time that the meridional overturning circulation should not be hemisphere-wide but instead limited to the subtropics. Ferrel got to his result by suggesting that since half of the earth's surface area is within 30°S and 30°N, then to a first approximation half the earth's mass should also be found in this region. In his era, it was known that the tropical region's zonal circulation was predominantly constituted of easterlies, which meant that half of the earth's atmospheric mass was retrograde. Therefore, in order to have an atmosphere that has no *net* angular momentum, it required that the other half of the earth's atmospheric mass be prograde. This simple argument then required that a reversal of the winds zonal direction occurs at around 30°S and 30°N, as observed on earth. Based on surface wind and pressure measurements, he also accurately predicted that the mean midlatitudes meridional circulation was bringing low-level air towards the poles and, thanks to mass conservation, high-level air had to be pushed towards the equatorial regions. Since high-level air has to have more intrinsic energy than low-level air, for otherwise it would sink, it suggests a transport of heat *from* the poles *to* the tropical regions must be taking place.

Over the years, as more data had been collected, it became possible to verify what this knowledge meant for the atmospheric radiative balance. Simpson (1929) computed for the first time the poleward heat transport necessary to close the heat budget in higher latitudes. With a strong radiative cooling and a relatively high surface temperature the climate in these regions could only be explained if vast quantities of heat was transported by atmospheric and oceanic currents. This madeFerrel's observation partic-

ularly confusing since it predicted meridional transports of heat in opposite direction. Ferrel was apparently not aware that his finding implied such a paradoxical flow of heat.

This state of affair puzzled dynamicists for many years as they could not explain why such a meridional heat transport should even exist in the first place. They could hardly explain why the atmosphere was not simply in radiative equilibrium at every latitudes, which was known to be an acceptable solution to the equations of motions. Bjerknes and Solberg (1922) had indeed formulated a theory for the atmospheric general circulation that included midlatitudes cyclones, at theory attributed them a direct role in the poleward transport of heat. This theory was however merely stating the ability of midlatitudes cyclones to transport heat but not why they should be the primary dynamical mechanism for bringing heat poleward.

It was only several years after Simpson (1929)'s observations, with the work of Charney (1947) and Eady (1949), that the fundamental role of large-scale turbulence in setting the circulation was first recognized. Charney was able to isolate a stability criterion for baroclinic instability and formulated a mathematical model to study the stability of balanced atmospheric flows. Using a simpler model, Eady investigated the same problem and showed clearly how a basic balanced flow always contains unstable modes. A laminar solution to the general circulation in the midlatitudes was then unlikely and the study of meridional heat transports became focused on eddy-related transports. Eady (1950) discusses the implications of this discovery and marks a turning point after which dynamicists started to admit turbulent meridional heat transfers as being the dominant process

setting the midlatitudes climate. This latter paper by Eady is of relevance even today as many questions it raises were proven to have no easy, simple answers.

The first breakthrough came with Eliassen and Palm (1961) who obtained an equation for the meridional momentum flux associated with weak interactions between atmospheric waves and the mean flow. While their work was quickly recognized as being of particular interest for many flows, it took several more years for Andrews and McIntyre (1976, 1978) to observe that it could be applicable, in a larger framework, to the problem of extratropical turbulence identified by Eady. By assuming that the midlatitudes' atmosphere was made of a mean baroclinic flow interacting non-linearly but weakly with baroclinic unstable waves, they could obtain a fix to Ferrel's theory that accounted for the observed meridional transport of heat. This new technique and theoretical perspective, called the Transformed Eulerian Mean (TEM), created a new paradigm. Because eddies usually have a vanishing mean meridional mass flux, it is extremely difficult to quantify the "stirring" they induce. That is, unless one decides to track the heat fluxes instead and deduce the stirring necessary to produce the observed heat fluxes. By making use of the weak interaction assumption, the TEM provides a method to obtain a simple expression for mass fluxes associated with the stirring. In analyzing these inferred mass fluxes care must however be taken because they do not have a direct correspondence to the actual mass fluxes that generate the general circulation. The drawback is that several characteristics of the TEM mass fluxes, like their vertical distribution and their maximum value, can be inaccurately represented.

These limitations are an undesired consequence of assuming that the interactions are weak. This assumption is overly restrictive and likely to be wrong for some atmospheric flows. Its shortcomings are particularly apparent at the surface where the lower boundary allows large variations that violate most smallness assumptions. The simplest way to circumvent this restriction is to analyze the meridional circulation on isentropic surfaces, thus creating a semi-Lagrangian analysis (McIntosh and McDougall, 1996; Karoly et al., 1997). This approach is the one we study in this thesis and that will be presented in detail throughout this work. In section 1.2, we shortly review the different techniques used to describe the meridional circulation and in section 1.3, we introduce the moist thermodynamics fundamentals that are required for a proper understanding of the isentropic analysis method. In the next subsection, we give a summary of the results described in this thesis' core chapters.

1.1.2 Summary of Results

In chapter 2, we propose a simplified description of the role played by moisture on the meridional overturning circulation using the mass flux joint distribution, a joint isentropic analysis that records meridional mass fluxes in terms of their potential and equivalent potential temperatures. The method involves separating the joint distribution into its northward and southward components, and subsequently projecting them onto potential temperature surfaces. This decomposition reveals fluxes that would otherwise disappear when performing a direct dry isentropic average. The revealed fluxes have non-negligible components from the surface to the

tropopause in most of midlatitudes, suggesting eddies with a deeper reach than would be deduced from a dry isentropic average. They also hint at a connection between the subtropics and the extratropics in which disturbances appear to extract water vapor from the Hadley cell subsiding branch and transport it towards the poles. The decomposition is simultaneously used to recover the vertical profiles of equivalent potential temperature typical for each of the directional components. The obtained profiles suggest a troposphere that has a lower moist stratification, as seen by the poleward component, than would be inferred by the climatological mean. This low moist stratification implies a strong connection between the surface and the mid tropospheric equivalent potential temperature in the poleward branch of midlatitudes eddies. With the help of a simple model of the low-level flow, it is shown that the equivalent potential temperature in the surface poleward mass fluxes is related to zonal variances of surface equivalent potential temperature. This theoretical model along with the diagnostics presented throughout the chapter provides a direct physical explanation for the known correlation between midlatitudes bulk moist stratification and meridional gradients of surface equivalent potential temperature.

In chapter 3, we study the effect of moisture on the net meridional transport induced by a moist baroclinic life-cycle. We use an idealized atmospheric dynamical core and an explicit initial balanced flow to conduct controlled numerical experiments (with an emphasis on reproducibility) to investigate the influence of troposphere moisture on the evolution of one baroclinic eddy. We specify a moist layer whose depth and relative humidity are varied to provide a continuous transition from a purely dry to

an entirely moist life cycle. We contrast the moist simulation dynamics with the dry simulation dynamics and observe the effect of latent heat release on potential vorticity dynamics. The dynamic is understood as part of a dry isentropic circulation, with isentropic layer thickness variations caused by convective vortex stretching. Using a cumulative isentropic analysis, performed by using the mass flux joint distribution averaged over a life-cycle, we describe changes in the dry and moist isentropic circulations produced by the introduction of a moist layer. As we increase the available moisture, the dry circulation is observed to weaken in the mid troposphere while the moist circulation is seen to exhibit an important strengthening. The addition of moisture displaces the moist circulation equatorward, which distinguishes it even more from the dry circulation. The difference between the two circulations is analyzed using the directional fluxes and the poleward θ_e profile and it is shown that more slantwise convection occurs when there are more cancellations between the two directional fluxes. Moreover, it is observed that increased cancellations project onto stronger eddy kinetic energies in the wave breaking region. It is concluded that as moist air is transported poleward along slanted moist isentropes, it directly influences the wave breaking strength.

In chapter 4, changes in isentropic circulations associated with global warming in A1B model outputs for the 20^{th} and 21^{st} centuries are analyzed. The changes in circulation averaged on dry and moist isentropes are quantified through the use of three bulk measures of the circulations that were used in chapter 3: mass transport, entropy transport and effective stratification. Over the course of the 21^{st} century, the circulation on dry

isentropes is diagnosed to weaken due to a reduction of the meridional heat transport and to an increase in stratification. In contrast, the moist branch of the circulation, measured in terms of the difference between the circulations on moist and dry isentropes, strengthens during the winter months. This intensification is characterized not only by an increase in eddy latent heat transport but also by an increase in mass transport. This indicates a larger poleward mass flow of warm moist subtropical air into the stormtracks leading to enhanced moist ascents within baroclinic eddies. Changes in the model average mass flux joint distribution characteristics are described using the tools presented in chapter 2. In particular, changes in directional fluxes and directional θ_e profiles are analyzed. Because poleward directional θ_e profiles are a key determinant of midlatitudes moist stratification, this point of view allows a precise quantification of surface warming influence on midlatitudes moist stability. Finally, we show how these diagnostics can be used to describe how the eddy structure evolves in a changing climate.

1.2 Meridional Overturning Circulation

The zonal-mean meridional overturning circulation captures the dynamics of air rising at the equator and subsiding at higher latitudes. There are many different ways to compute it and each of these methods allows for different diagnostics. This means that the right method will often depend on the problem at hand and more specifically on which quantity is assumed to a key descriptor of the problem.

1.2.1 Eulerian-mean

The most straightforward way to describe the meridional dynamics of a dry atmosphere is to take a zonal and temporal mean at fixed pressure and latitude (see Vallis, 2006, for more details). This flow satisfies the zonal-mean continuity equation:

$$\partial_\phi(2\pi a \cos\phi[v]) + \partial_p(2\pi a \cos\phi[\omega]) = 0, \tag{1.1}$$

where $[v]$[1] is the zonal-mean meridional velocity and $[\omega]$ is the zonal-mean vertical velocity in pressure coordinates. The coordinates ϕ and p correspond to latitude and pressure, respectively, while the parameter a stands for the earth's radius. The zonal-mean flow, with a vanishing divergence

[1] The zonal-mean in pressure coordinates is thought of being mass-weighted when isobar intersect the surface:

$$[v] = \frac{1}{2\pi}\int_0^{2\pi} vH(p - p_s)d\lambda, \tag{1.2}$$

where p_s is the surface pressure and $H(\cdot)$ is the heaviside function that is 1 for a positive argument and 0 otherwise. For sufficiently large p, $[v]$ will be equal to 0 in this formulation.

in the (ϕ, p) plane, can be represented with the help of a streamfunction $\Psi_p(\phi, p)$:

$$\Psi_p(\phi, p) = 2\pi a \cos\phi \int_p^\infty [v] dp, \tag{1.3}$$

such that

$$\partial_p \Psi_p = -2\pi a \cos\phi [v], \qquad \partial_\phi \Psi_p = 2\pi a \cos\phi [\omega]. \tag{1.4}$$

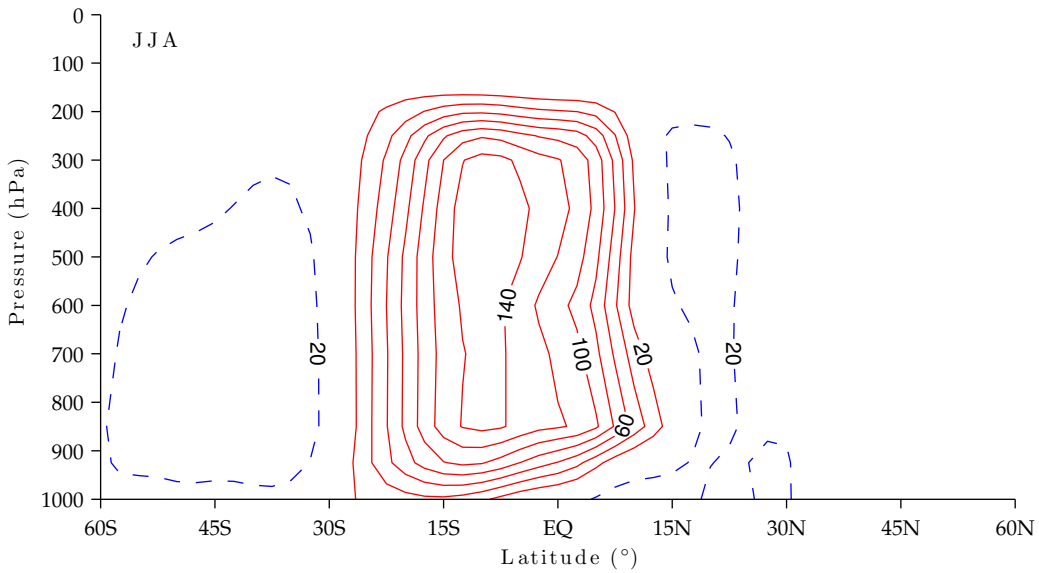

FIGURE 1.1. June-July-August Eulerian-mean circulation in pressure coordinates using the NCEP I reanalysis for the years 1991-2000. Red, solid contours are positive and blue, dashed contours are negative. Contour labels units are 10^9 kg s^{-1}. This circulation was computed without removing below-surface values which is why the Hadley cell intersects the lower boundary. For mid tropospheric isobars, the distortions created by this computational artifact becomes negligible.

The resulting streamfunction, in Figure 1.1 has a three-cell structure: a Hadley cell in the subtropics, a Ferrell cell in the midlatitudes and a polar cell (not shown in Figure 1.1) in the polar region. The Hadley cell is driven

by upward mass fluxes generated by moist convection in the ITCZ. The compensating subsidence occurs in subtropical regions by the action of radiative cooling. The Hadley cell is vigorous and peaks in the winter hemisphere at low latitudes. The Ferrel cell is a reversed cell that appears to bring low-level air poleward, air that rises at the beginning of the polar cell and returns equatorward in the high troposphere. The Ferrel cell is much weaker than the Hadley cell and is peculiar because it appears to be bringing warm high-level air equatorward with a return flow of cold low-level air poleward. From this one could naively infer that the overturning circulation in midlatitudes works to cool the high latitudes and warm the subtropics.

1.2.2 Transformed Eulerian-mean

If one computes the meridional flux, F_θ, of potential temperature, θ, a quantity equivalent to dry static energy, one obtains

$$F_\theta = \int_0^\infty [\theta v] dp = \int_0^\infty [\theta][v] + [\theta' v'] dp, \tag{1.5}$$

where primes denote departures from the zonal mean: $\theta' = \theta - [\theta]$ and $v' = v - [v]$. In subsection 1.2.1, when discussing the flows of heat, we only considered transport by the mean flow of the mean θ, which corresponds to the first term on the right hand side. Because it led to a paradoxical picture of heat flows, it is natural to conclude that the product $[\theta][v]$ is not a good description of the meridional fluxes of heat and that therefore one has to explicitly consider fluxes due to correlations, $[\theta' v']$, between poleward

flows and positive potential temperature anomalies. One way of including these fluxes is to assume that the product $[\theta][v]$ is deficient because one of its two factors is inadequately representing the turbulent atmosphere. If we consider that perturbations due to turbulent eddies are small about the atmospheric mean, it is reasonable to assume that $[\theta]$ represents a typical atmospheric state. Such an assumption suggests that among the zonal mean quantities $[\theta]$ and $[v]$, the latter is the least adequately representing the real turbulent atmosphere. It should therefore be discarded and replaced by a modified quantity, $[v^*]$, a transformed mass flux, that satisfies

$$F_\theta = \int_0^\infty [\theta][v_*]dp = \int_0^\infty [\theta][v] + [\theta' v']dp. \tag{1.6}$$

On an isobar, the difference $[v_*] - [v]$ is thought to represent the mass flux occuring due to displacements of air masses with different heat contents. Unfortunately, there is not a unique such quantity and extra constraints must be added in order to specify a solution. To this end we further assume that environmental waves are sufficiently weak that their typical potential temperature variability per mass is proportional to $\partial_p[\theta]$:

$$\delta\theta = \gamma\partial_p[\theta], \tag{1.7}$$

where γ is a proportionality constant that has units of pressure. This will be an appropriate correspondence if the waves are buoyancy-driven. Because environmental waves were said to have air displacements producing mass fluxes $[v_*] - [v]$, we can reasonably expect that eddy fluxes of heat be

proportional to its product with the variability $\delta\theta$:

$$\int_0^\infty [\theta' v'] dp = \int_0^\infty \delta\theta([v_*] - [v]) dp = \int_0^\infty \gamma \partial_p[\theta]([v_*] - [v]) dp. \tag{1.8}$$

Integrating by parts and assuming that displacements vanish at the integral's bounds,

$$\int_0^\infty [\theta' v'] dp = -\int_0^\infty [\theta] \partial_p \big(\gamma([v_*] - [v])\big) dp, \tag{1.9}$$

and after substituting in equation (1.6) one obtains

$$\int_0^\infty [\theta] \Big\{ ([v_*] - [v]) - \partial_p \big(\gamma([v_*] - [v])\big) \Big\} dp = 0. \tag{1.10}$$

If one wants the resulting solution to be valid no matter what background state is, then one has to require that the expression in brackets vanishes uniformly. This results in the following expression for the eddy flux:

$$\int_0^\infty [\theta' v'] dp = \int_0^\infty \partial_p[\theta] \left(\int_0^p [v_*] - [v] dp' \right) dp. \tag{1.11}$$

This equation can be rewritten as

$$\int_0^\infty \left\{ \frac{[\theta' v']}{\partial_p[\theta]} - \left(\int_0^p [v_*] - [v] dp' \right) \right\} \partial_p[\theta] dp = 0. \tag{1.12}$$

After integrating by parts to transfer the pressure derivative onto the expression in brackets and by requesting once more that the solution be

independent of the background state, one obtains:

$$[v_*] = [v] - \partial_p \left(\frac{[\theta' v']}{\partial_p [\theta]} \right). \tag{1.13}$$

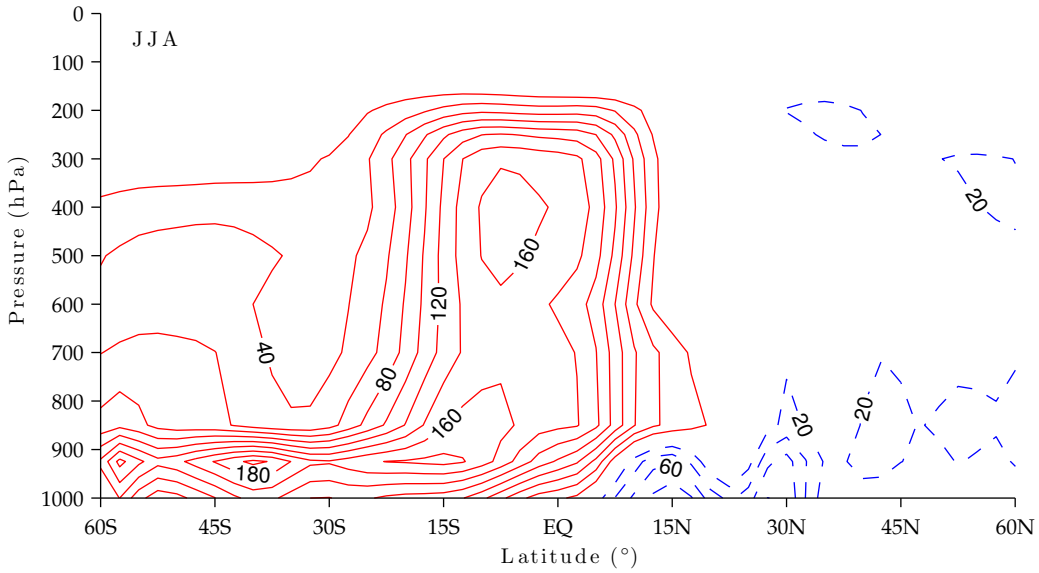

FIGURE 1.2. June-July-August Transformed Eulerian-mean circulation in pressure coordinates using the NCEP I reanalysis for the years 1991-2000. Red, solid contours are positive and blue, dashed contours are negative. Contour labels units are 10^9kg s^{-1}. This circulation was computed with the same method as for Figure 1.1.

We plot in Figure 1.2 the streamfunction representing the circulation corresponding to $[v_*]$. In this corrected circulation, the reversed Ferrel cell is now replaced by a forward cell from which one can infer the correct heat fluxes. The representation of the meridional circulation is however imperfect, its primary limitation being its inability to create closed streamlines at the surface. This problem has been addressed by Held and Schneider (1999) where it was shown that the TEM failed (their figure 3) in the lower troposphere in part because the stratification $\partial_p [\theta]$ was small and thus no longer

a good measure of wave disturbance. By comparing it to the meridional circulation in isentropic coordinates (discussed next, in subsection 1.2.3), they were able to show that the problem resided in large surface variations of temperature, arguing that these variations were caused by the common occurrences of cold air outbreaks. The large variations found within these outbreaks can be produced only because the rigid surface boundary tends to modify the isentropic dynamic by injecting potential vorticity in the interior flow. Because the surface dynamic creates a mixed layer close to the surface, its results in low surface stratification $\partial_p[\theta]$ in a flow region where the dynamics generates waves with intrinsically large variability.

While in lower troposphere the stratification is a poor proxy for variability, the meridional gradients $\partial_y[\theta]$ are on the other hand relatively good. After interchanging the two, Held and Schneider (1999) show that the TEM can be used to explain most features of the isentropic circulation, therefore verifying an equivalence expected in the limit of small amplitude perturbation (shown rigorously by Andrews and McIntyre, 1976). Plumb and Ferrari (2005) generalized this idea even further by assuming that local variability is proportional to the norm of $[\theta]$ gradients, $|[\nabla][\theta]|$, where $[\nabla] = (\partial_y, \partial_p)$. In this case, $[v^*]$ will take the following form (see Plumb and Ferrari, 2005; Vallis, 2006):

$$[v^*] = [v] - \partial_p \left(\frac{[v'\theta']\partial_p[\theta] - [\omega'\theta']\partial_y[\theta]}{|[\nabla][\theta]|^2} \right). \tag{1.14}$$

A fundamental problem with expression (1.14) is that it does not satisfy (1.6) and therefore does not account explicitly for meridional energy

fluxes. Beyond this limitation, the expression (1.14) is able to fix most of the aforementioned problems, wherever $||[\nabla][\theta]||$ is indeed proportional to the local θ variability. Because at every latitude (except maybe in the ITCZ) the turbulent nature of atmospheric flows creates substantial tracer variability, this version of the TEM fails if $||[\nabla][\theta]||$ vanishes. This never happens but if one replaces θ by the equivalent potential temperature θ_e, $||[\nabla][\theta_e]||$ usually vanishes in the subtropics. As it will be seen later, θ_e is related the moist static energy of an air parcel and as such represents the total heat content of a moist air parcel accurately. Due to this equivalence, in a moist atmosphere, it would be more desirable to track the stirring created by fluxes of θ_e instead of tracking the stirring related to fluxes of θ. Since this is impossible using any of the TEM formulations, one has to use a moist isentropic analysis, which we discuss next.

1.2.3 Isentropic

The underlying approach used throughout this thesis consists in calculating the meridional circulation on potential temperature surfaces (Johnson, 1989; Karoly et al., 1997; Held and Schneider, 1999). It is known to resolve the Hadley circulation reliably and represent midlatitudes eddies in a way that is consistent with the net poleward transport of sensible heat. Its capacity at resolving the eddy climatology comes from its ability at discriminating between warm poleward flows with high potential temperatures and cold equatorward flows with low potential temperatures. The separation between warm poleward and cold equatorward is conserved through the evolution of eddies because potential temperature is mostly

invariant over a typical eddy time-scale of about six or seven days and only in the absence of moist convection. The result (shown in the upper panel of Figure 1.3) is that potential temperature on a parcel is mostly conserved by eddy motions and therefore can be considered a partial Lagrangian marker within those eddies. The inferred isentropic circulation is stronger than the one computed using an Eulerian average and has one great advantage: potential temperature fluxes deduced from it implicitly include eddy transport terms.

This method is however insufficient as midlatitudes eddies possess an important moisture component coming from two primary sources. Eddies can transport moisture poleward from the subtropics to the midlatitudes (Yang and Pierrehumbert, 1994; Pierrehumbert, 1998) or lift it from the extratropical planetary boundary layer through their moist conveyor belt. The moist eddies transport unsaturated air poleward and upward along slanted dry isentropes, a motion that cools the moist air and brings it towards saturation. Once saturated, this moist air either starts following a slanted moist isentrope or begins convecting vertically.

The effect of moisture on large-scales has been studied by Schneider et al. (2006) who computed fluxes of moisture on isentropic surfaces and showed that a balance exists between an influx of moisture from the Hadley circulation and an eddy outflux to the extratropics. They argued that the direct impacts of moisture on subtropical eddies would only lead to a simple correction to their analysis and neglect it altogether. While latent heat effects are not dominant in their region of interest, there are several features of the meridional circulation that can only be explained if latent

heat release is considered a key component of the large scale dynamic.

One way to explicitly include the effect of latent heat is to follow Czaja and Marshall (2006), Pauluis et al. (2008) and Pauluis et al. (2010a) and compute the meridional isentropic circulation using the equivalent potential temperature instead of using the potential temperature. Unlike the circulation on dry isentropes, this circulation on moist isentropes includes the total heat flux — sensible plus latent — and allows to diagnose mass fluxes associated with observed total heat fluxes. While the potential temperature is not conserved for adiabatic saturated motions, the equivalent potential temperature is. It is therefore expected that the circulation on moist isentropes captures Lagrangian trajectories more closely than the circulation on dry isentropes in regions where condensation occurs. As a consequence, the circulation on moist isentropes (shown in the lower panel of Figure 1.3) is found to be more vigorous in the extratropics, where latent heat release by condensation is a key diabatic heating source. In this thesis, we are particularly interested in understanding the effect of moisture fluxes on the dry isentropic circulation and relate them to the circulation on moist isentropes.

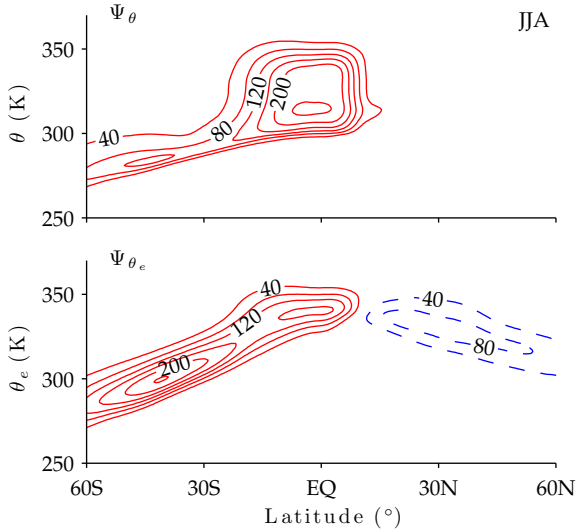

FIGURE 1.3. June-July-August Isentropic Circulations. Dry circulation in the upper panel and moist circulation in the lower panel. These circulations were computed using the ERA40 reanalysis dataset for the years 1991-2000. Red and solid contours are positive while blue and dashed contours are negative. Contours levels start at 40×10^9 kg s^{-1} in 40×10^9 kg s^{-1} increments.

1.3 Moist Thermodynamics

Thermodynamics is the study of heat exchanges that are necessary to bring an unbalanced physical system to equilibrium. By applying its fundamental laws, it is possible to find the final state of complex systems even if they start from a completely heterogeneous state and undergo dramatic transitions. The *zeroth law* defines the meaning of equilibrium by stating its transitivity. If two thermodynamical systems are in equilibrium with a third, then all three systems are in equilibrium. The *first law* states the conservation of energy and can be formulated using the following equation:

$$\delta Q = \delta U + \delta W, \tag{1.15}$$

that means that an input of heat δQ either adds to the internal δU or produces work δW. If the heating is applied to the system through a sequence of quasi-steady, reversible steps, then the heating process produces changes in entropy S that are related to the input of heat:

$$TdS|_{\text{rev}} = \delta Q. \tag{1.16}$$

In this case, the equation for the conservation of energy adopts the form of total differential,

$$TdS = dU + dW. \tag{1.17}$$

In this thesis, we are concerned with gases and we prefer to use the Legendre-transform version of this equation where the internal energy

is replaced by the enthalpy:

$$Tds = dh - \alpha dp, \tag{1.18}$$

written in terms of the specific entropy s, the specific enthalpy h, the specific volume α and the pressure p.

The *second law* states that the entropy of the universe always increases. For an isolated system, this means that equation (1.16) does not apply for irreversible processes. Instead, it takes the form

$$T(dS|_{\text{rev}} + dS|_{\text{irrev}}) = \delta Q, \quad dS|_{\text{irrev}} \geq 0. \tag{1.19}$$

This restriction that the irreversible entropy must increase, explains why some energy-conserving processes are impossible. Take water vapor, for example. When temperature is below the saturation temperature, water vapor can condensate to liquid water but liquid water cannot be evaporated into water vapor. On the other hand, when temperature is above the saturation temperature, liquid water can evaporate but water vapor cannot condensate. This restriction on the direction of phase transitions is important for this work because it precludes the release of latent heat unless air is saturated. Finally, the *third law* defines the absolute zero temperature and the impossibility of attaining it. We will not make use of this law within this work.

Even thought thermodynamics is supposed to apply to systems in equilibrium, it often enables physicists to quantify energy transfers in transient, unbalanced systems. Moist thermodynamics for atmospheric dynamics

makes use of the laws of thermodynamics to understand the properties of a composite of water and dry air. The water should be allowed to change phases and thus reach states that contain a mixture of vapor, water droplets and ice pellets. The exact blend will evidently depend on the equilibrium temperature but also on the presence and nature of aerosols. Determining the precise distribution of the three phases is usually an arduous task that falls within the realm of *cloud microphysics*. In this work, we will not be interested in the consequences of aerosols on the equilibrium state of a moist system. Instead, we will focus on a specific idealization of moist themodynamics where phase changes depend solely on the equilibrium state. Within this approximation, the latent heat release associated with condensation is retained. In other words, we are making sure that heat spent to evaporate water vapor is deposited wherever the vapor it condensates. Other secondary effects are included in the idealized moist thermodynamics; they will be presented in subsection 1.3.4.

As mentioned earlier, the formulation of thermodynamics requires a system that reaches equilibrium. Many non-equilibrium effects are due to the compressibility of air, which means that they propagate and equilibrate at the local sound speed. The usual description of the atmosphere eliminates sound waves because of their short time-scale: atmospheric air is thus assumed to always be in local equilibrium. From an air parcel perspective, this means that after some heat and mass exchange the parcel will reach a thermodynamical equilibrium state on time scales small compared with every other time scales. Super cooled water in ascending clouds and re-evaporation of rain hydrometeors are some notable non-equilibrium effects

that can violate this assumption. These will be largely ignored throughout this work even if they can sometimes be non-negligible. All these considerations justify that we use local thermodynamical equilibrium in the treatment of moist atmospheric thermodynamics.

Therefore when we look at model outputs, thermodynamics will be assumed to hold at the grid-scale level even if those grid-scales are hundred of kilometers in horizontal extent. Together with the neglect of microphysics, our formulation of moist thermodynamics allows only large-scale condensation and large-scale precipitation. No sub-grid scale parametrizations are thus required or even available.

We could summarize the above discussion by simply stating that we are primarily interested in budgets. This means that the moist thermodynamics we are using aims primarily at closing heat and mass budgets but not at accurately representing the real spectrum of attainable thermodynamical states. In many ways, we are following a similar approach to that of Emanuel (1994).

1.3.1 Liquid Water

We begin by investigating the thermodynamical properties of liquid water. Liquid water can take many different shapes and forms: it can be as massive as an ocean or as tiny as a microscopic water droplet. In the latter, surface tension effects can add to the energy of water droplets, increasing the complexity of its thermodynamical treatment. Its neglect is necessary to arrive at a simple formulation and in this case the specific energy of water

droplets correspond simply to its thermal internal energy h_l:

$$h_l - h_{l0} = c_l T, \tag{1.20}$$

where T is the temperature, c_l is the specific heat of liquid water and h_{l0} is an arbitrary reference enthalpy. Because under typical atmospheric conditions liquid water is incompressible, its internal energy is also its enthalpy and equation (1.20) can thus refer to either.

The first law of thermodynamics for reversible processes states how the entropy of liquid water changes

$$T ds_l = dh_l, \tag{1.21}$$

which can be readily integrated to give

$$s_l - s_{l0} = c_l \ln \frac{T}{T_0}, \tag{1.22}$$

where T_0 is an arbitrary reference temperature and s_{l0} is an arbitrary reference entropy.

1.3.2 Mixture of Water Vapor and Liquid Water

We consider a pure mixture of water vapor and liquid water droplets, without the presence of any other chemical species. The water vapor is simply an ideal gas with its particular gas constant, R_v. The enthalpy of

water vapor is given by the expression of enthalpy for an ideal gas

$$h_v - h_{v0} = c_{pv} T, \tag{1.23}$$

where c_{pv} is the specific heat at constant pressure of water vapor and h_{v0} is an arbitrary reference enthalpy.

Like the liquid water, the entropy s_v of water vapor can be deduced from the first law of thermodynamics

$$T ds_v = dh_v - \frac{de}{\rho_v}, \tag{1.24}$$

where e is the water vapor pressure. Its density ρ_v is related to the pressure and temperature through the ideal gas law.

$$\rho_v(e, T) = \frac{e}{R_v T}. \tag{1.25}$$

With this, the first law (1.24) can be integrated to yield

$$s_v - s_{v0} = c_{pv} \ln \frac{T}{T_0} - R_v \ln \frac{e}{e_0}, \tag{1.26}$$

where e_0 is a reference vapor pressure and s_{v0} is the water vapor reference entropy.

An ideal mixture of two components is described by the mass-weighted average of each of the components' specific quantities. In the case of water vapor and liquid water, this means that the mixture enthalpy h_a and entropy s_a will be mass-weighted averages of (1.20) and (1.23), and (1.22) and (1.26),

respectively:

$$\rho h_a = \rho_l h_l + \rho_v h_v, \tag{1.27a}$$

$$\rho s_a = \rho_l s_l + \rho_v s_v. \tag{1.27b}$$

The density of water droplets ρ_l represents the mass of water droplets per volume and ρ represents the total mass per volume, equal in this case to the sum $\rho_v + \rho_l$. The specific ratios

$$q_v = \frac{\rho_v}{\rho_l + \rho_v}, \quad \text{and} \quad q_l = \frac{\rho_l}{\rho_l + \rho_v}, \tag{1.28}$$

are not independent: they add up to unity, $q_v + q_l = 1$.

The mass-weighted quantities (1.27) satisfy a new second law that includes a chemical exchange term $g_l - g_v$,

$$T ds_a = dh_a - \frac{de}{\rho} + (g_l - g_v) dq_v, \tag{1.29}$$

related to the *Gibbs Free Energies* of liquid water g_l and water vapor g_v that are given by

$$g_l = Ts_l - h_l, \tag{1.30a}$$

$$g_v = Ts_v - h_v. \tag{1.30b}$$

1.3.3 Clausius-Clapeyron Equation

In subsection 1.3.2, we have assumed that any state given by coordinates T, e and q_v is achievable. This means that we have not imposed any limit on

the amount of water vapor and therefore we have implicitly allowed supersaturation. In a system at equilibrium, supersaturation rarely occurs and the vapor pressure e rarely exceeds its saturation value. Once we know this saturation value, we will be able to reduce the number of thermodynamics coordinates from three to two and thus greatly simplifying the treatment of the multi-phase system. Before, however, we need to derive from first principles the saturation curve.

Rewriting the first law (1.29) with the internal energy $u_a = h_a - \alpha e$, where α is the specific volume, leads to

$$Tds_a = du_a + ed\alpha + (g_l - g_v)dq_v. \tag{1.31}$$

Consider a closed system of fixed volume, so that the total mass and volume do not change, which implies that $d\alpha = 0$. Moreover, since heat exchanges are not allowed, its internal energy cannot change, $du_a = 0$. In such a system,

$$Tds_a = (g_l - g_v)dq_v. \tag{1.32}$$

Invoking the second law of thermodynamics, we require

$$ds_a = ds_a|_{\text{irrev}} \geq 0, \tag{1.33}$$

for an adiabatic process. Because at saturation both conversions from water vapor to liquid water and from liquid water to water vapor are allowed, we must assume that dq_v can take on both signs. This means that and adiabatic phase change can only occur if $g_l - g_v = 0$. This is the *Clausius-Clapeyron*

equation, usually written as

$$\frac{1}{e_s}\frac{de_s}{dT} = \frac{L_v(T)}{R_v T^2}, \tag{1.34}$$

where $L_v(T) = L_{v0} - (c_l - c_{pv})(T - T_0)$ is the *Latent Heat of Vaporization* for the ideal mixture. The latent heat of vaporization at T_0, L_{v0}, is measurable in the laboratory and is related to other constants through the relation $L_{v0} = h_{l0} - h_{v0} - (c_l - c_{pv})T_0$. The Clausius-Clapeyron equation can be easily integrated to yields

$$R_v \ln \frac{e_s}{e_s(T_0)} = L_v(T)\left(\frac{1}{T_0} - \frac{1}{T}\right) - (c_l - c_{pv})\left(\ln \frac{T}{T_0} + 1 - \frac{T}{T_0}\right). \tag{1.35}$$

If one insists that an ideal mixture of liquid water and water vapor exchanges mass only at saturation, then the difference in Gibbs free energies $g_l - g_v$ is zero everywhere. Substituting equation (1.35) in their expression, one obtain

$$g_l - g_v\Big|_{e=e_s(T)} = T\left(s_{l0} - s_{v0} - \frac{L_{v0}}{T_0} - R_v \ln \frac{e_s(T_0)}{e_0}\right), \tag{1.36}$$

which requires that the expression within the right hand side parentheses vanishes. This determines the difference $s_{l0} - s_{v0}$ and the expression for the latent heat determines the difference $h_{l0} - h_{v0}$:

$$s_{l0} - s_{v0} = \frac{L_{v0}}{T_0} + R_v \ln \frac{e_s(T_0)}{e_0}, \tag{1.37a}$$

$$h_{l0} - h_{v0} = L_{v0} + (c_l - c_{pv})T_0, \tag{1.37b}$$

which provides two equations for the four unknowns s_{l0}, s_{v0}, h_{l0} and h_{v0}. In the next section, we will however show that it is possible to obtain more constraints when water is mixed with dry air.

1.3.4 Mixture of Moisture and Dry Air

Atmospheric air is composed of a gas mixture that comprises oxygen, nitrogen, carbon dioxyde and water vapor. The chemical composition of dry atmospheric air — that is atmospheric air without water vapor — is relatively uniform around the globe. Because of this uniformity, it is usual to assume dry air to be a gas with a fixed gas constant R_d equal to the gas constant of the mixture.

Moisture must however be added independently as its concentration varies widely within the atmosphere. As it was seen earlier it also changes phase quite commonly, a process that releases a lot of latent heat and therefore changes the internal energy of saturated air parcels. In a development similar to the liquid water and water vapor mixture, we investigate this mixture of dry air, water vapor and liquid water. The enthalpy and entropy of dry air are given by

$$s_d = c_{pd} \ln \frac{T}{T_0} - R_d \ln \frac{p_d}{p_{d0}}, \tag{1.38a}$$

$$h_d = c_{pd} T. \tag{1.38b}$$

A general expression for the entropy of moist air can be found by using expressions for the individual entropies and mass-weighing them. This

results in

$$s_w = q_d s_d + q_v s_v + q_l s_l, \tag{1.39a}$$

$$= \bar{c} \ln \frac{T}{T_0} - \bar{R} \left(\ln \frac{p}{p_0} + \beta \left(\frac{e}{p}, \frac{e_0}{p_0} \right) \right) + s_{v0} q_v + s_{l0} q_l, \tag{1.39b}$$

where $\bar{c} = q_d c_{pd} + q_v c_{pv} + q_l c_l$ is the mass-weighted specific heat, $\bar{R} = q_d R_d + q_v R_v$ is the mass-weighted specific gas constant and $\beta(a, b) = a \ln \frac{a}{b} + (1 - a) \ln \frac{1-a}{1-b}$ is a (relative) entropy of mixing. It corresponds to the entropy of mixing of dry air and water vapor at constant pressure. The specific mass ratios q_d, q_v and q_l are related by an equivalent of equation (1.28):

$$q_d = \frac{\rho_d}{\rho_d + \rho_v + \rho_l}, \quad q_v = \frac{\rho_v}{\rho_d + \rho_v + \rho_l}, \quad q_l = \frac{\rho_l}{\rho_d + \rho_v + \rho_l}. \tag{1.40}$$

The density of each species are denoted by ρ_d for the density of dry air, by ρ_v for the density of water vapor and by ρ_l for the density of liquid water droplets. We refer to the specific total water content by $q_T = q_v + q_l$.

A moist air entropy will always be related to a moist air enthalpy, found by taking the mass-weighted sum of each of the species enthalpy:

$$h_w = \bar{c} T + h_{v0} q_v + h_{l0} q_l. \tag{1.41}$$

Both the moist air entropy and the moist air enthalpy satisfy the first

law of thermodynamics

$$Tds_w = dh_w - \alpha dp + (\underline{g_v} - g_d)dq_T + (g_l - g_v)\underline{dq_l}, \tag{1.42a}$$

$$= dh_w - \alpha dp + (\underline{g_l} - g_d)dq_T + (g_l - g_v)\underline{(-dq_v)}, \tag{1.42b}$$

where $g_d = Ts_d - k_d$ is the Gibb's free energy of dry air and g_v, g_l are as before. These two expressions are equivalent and differ only in the underlined terms.

1.3.4.1 Diabatic exchanges of water

By not allowing supersaturation or re-evaporation of rain drops, we are ensuring that conversion from one phase to the other occurs only at saturation. At saturation, the constraints (1.37) originating from the Clausius-Clapeyron equation $g_l - g_v = 0$ ensure that the last term in both equations (1.42) vanishes uniformly within the idealized moist atmosphere.

The two formulations will differ only when there is a change in total water content, $dq_T \neq 0$, i.e. when liquid water precipitates or when moisture is inputed in the form of water vapor. In this case, one wants to define the constants s_{v0}, s_{l0}, k_{v0} and k_{l0} as to minimize the impact of total water content changes on the moist air entropy (1.42). For both formulations, there will be a different set of constants that minimize the pre-factor to dq_T around the moist reference state p_0, e_0 and T_0.

In the first formulation, (1.42a), the pre-factor reads

$$g_v - g_d = (c_{pv} - c_{pd})T\left(\ln\frac{T}{T_0} - 1\right) - R_v T \ln\frac{e}{e_0} + \ldots \\ R_d T \ln\frac{p_d}{p_{d0}} + T s_{v0} - k_{v0}, \quad (1.43)$$

which vanishes at the moist reference state only if $k_{v0} = T_0 s_{v0}$. In the second formulation, (1.42b), the pre-factor is

$$g_l - g_d = (c_l - c_{pd})T\left(\ln\frac{T}{T_0} - 1\right) + R_d T \ln\frac{p_d}{p_{d0}} + T s_{l0} - k_{l0}, \quad (1.44)$$

and it vanishes at the moist reference state only if $k_{l0} = T_0 s_{l0}$.

Interestingly, in light of equations (1.37) it appears that both formulations can be simultaneously be minimized if $(c_l - c_{pv})T_0 = R_v \ln\frac{e_s(T_0)}{e_0}$ Usually, however, we take $e_s(T_0) = e_0$, which would demand $c_l = c_{pv}$. In general, this is not true, so that we can only minimize one of the two formulations at the same time and each minimization leads to a different moist air entropy.

The unspecified constants determine how much latent heat is included in the moist air enthalpy. In subsubsection 1.3.4.2, we show one particular choice of constants were no latent heat is included and the resulting moist air enthalpy is essentially equal to the dry air enthalpy. In subsubsection 1.3.4.3, we present another set of constants that results in an enthalpy were all of the latent heat is explicitly included. Because the latent heat can or cannot be released, choosing which set of constants is most appropriate will depend on the problem at hand. If, for example, one wishes to moist

study convection it is typical to assume that moist air will release all of its latent heat and that therefore it is preferable to include it in the energy budget from the beginning. In such a case, it would be more appropriate to use the formulation in subsubsection 1.3.4.3.

1.3.4.2 Liquid water entropy

Using the first formulation (1.42a) and setting $h_{v0} = T_0 s_{v0}$, the recovered entropy-enthalpy pair will be

$$\begin{aligned} s_l = \bar{c} \ln \frac{T}{T_0} - \bar{R} \left(\ln \frac{p}{p_0} + \beta \left(\frac{e}{p}, \frac{e_0}{p_0} \right) \right) + \dots \\ - \left(\frac{L_{v0}}{T_0} + R_v \ln \frac{e_s(T_0)}{e_0} \right) q_l + s_{v0} q_T \end{aligned} \tag{1.45}$$

$$h_l = \bar{c}_v T - L_v(T) q_l + T_0 s_{v0} q_T. \tag{1.46}$$

where $\bar{c}_v = (c_{pd} + (c_{pv} - c_{pd}) q_T)$. If ones chooses $s_{v0} = 0$, on recovers the same expression as in Emanuel (1994) for the *Liquid Water Entropy*. Choosing $s_{v0} = 0$ in addition guarantees that $g_v - g_d$ has a vanishing temperature partial derivative, at constant p_d, at $T = T_0$.

Substituting (1.35) in (1.45), yields

$$s_l = \bar{c}_v \ln \frac{T}{T_0} - q_l R_v \ln \frac{e_s(T)}{e_0} - \bar{R} \left(\ln \frac{p}{p_0} + \beta \left(\frac{e}{p}, \frac{e_0}{p_0} \right) \right) - \frac{L_v(T)}{T} q_l, \tag{1.47}$$

which is an expression that depends on the full (T_0, p_0, e_0) reference state.

One can define the *liquid water potential temperature* by finding the temperature an air parcel would have if it were moved adiabatically to a level where there is no liquid water. If we assume that this level is at $p = p_0$, one

can solve for the liquid water potential temperature, θ_l:

$$\theta_l = T_0 e^{\frac{s_l}{\bar{c}_v} + \frac{\bar{R}}{\bar{c}_v}\beta\left(q_T \frac{\epsilon+1}{1+\epsilon q_T}, \frac{e_0}{p_0}\right)}. \tag{1.48}$$

This form shows the intimate link between θ_l and s_l. Because the entropy of mixing between water vapor and dry air is usually small, one can see that they are essentially the same quantity. Using equation (1.47) and assuming that the air parcel does not contain liquid water, it is possible to simplify this expression:

$$(\theta_l)_{\text{unsat}} = T\left(\frac{p}{p_0}\right)^{\frac{\bar{R}}{\bar{c}_v}}, \tag{1.49}$$

which is exactly equal to the virtual potential temperature θ_v:

$$(\theta_l)_{\text{unsat}} \equiv \theta_v. \tag{1.50}$$

When saturated, however, this correspondence is false and both potential temperatures can differ significantly. If rain is considered, it is rare that moist air remains saturated over long periods, so that this correspondence is actually exact almost everywhere.

1.3.4.3 Moist entropy

Using the first formulation (1.42b) and setting $h_{l0} = T_0 s_{l0}$, the recovered entropy-enthalpy pair will be

$$s_m = \bar{c} \ln \frac{T}{T_0} - \bar{R} \left(\ln \frac{p}{p_0} + \beta \left(\frac{e}{p}, \frac{e_0}{p_0} \right) \right) + \ldots \left(\frac{L_{v0}}{T_0} + R_v \ln \frac{e_s(T_0)}{e_0} \right) q_v + s_{l0} q_T, \tag{1.51}$$

$$h_m = \bar{c}_l T + L_v(T) q_v + T_0 s_{l0} q_T. \tag{1.52}$$

where $\bar{c}_l = (c_{pd} + (c_l - c_{pd}) q_T)$ is the specific heat if all the water is in liquid form. If ones chooses $s_{l0} = 0$, one recovers the same expression as in Emanuel (1994) for the *Moist Entropy*. Once more, this peculiar choice of s_{l0} guarantees that $g_v - g_d$ has a vanishing temperature partial derivative at $T = T_0$.

Substituting (1.35) in (1.51), yields

$$s_m = \bar{c}_l \ln \frac{T}{T_0} - R_d (1 - q_T) \ln \frac{p_d}{p_0 - e_0} + \left(\frac{L_v(T)}{T} - R_v \ln \mathcal{H} \right) q_v, \tag{1.53}$$

which is a quantity that only depends on the reference state $(T_0, p_0 - e_0)$ and is therefore somewhat less arbitrary.

If a parcel is lifted adiabatically until $q_v \sim 0$, $p_d \sim p$ the expression (1.53) will then take the form

$$s_m \sim \bar{c}_l \ln \frac{T}{T_0} - R_d (1 - q_T) \ln \frac{p}{p_0 - e_0} \tag{1.54}$$

which means that, solving for T,

$$T \sim T_0 \left(\frac{p}{p_0 - e_0} \right)^{\frac{R_d(1-q_T)}{\bar{c}_l}} e^{\frac{s_m}{\bar{c}_l}}. \tag{1.55}$$

Bringing the parcel back to $p = p_0 - e_0$ by making sure that the water does not re-evaporate, yields the *equivalent potential temperature*

$$\theta_e = T_0 e^{\frac{s_m}{\bar{c}_l}}. \tag{1.56}$$

1.3.4.4 Rain

For our modelling purposes in chapter 3, rain is an isothermal and isobaric process where liquid water simply leaves an air parcel. When there is condensation, the vapor specific ratio is

$$q_v = \frac{R_d}{R_v}(1 - q_T)\frac{e_s(T)}{p - e_s(T)}, \tag{1.57}$$

which means that the curve $q_T = q_v$ is satisfied for q_v^* given by

$$q_v^*(p, T) = \frac{R_d}{R_v}\frac{e_s(T)}{p - e_s(T)} \Big/ \left(1 + \frac{R_d}{R_v}\frac{e_s(T)}{p - e_s(T)}\right) \tag{1.58}$$

One can write the specific ratios in terms of this quantity

$$q_v(p, T, q_T) = (1 - q_T)\frac{q_v^*}{1 - q_v^*}, \tag{1.59a}$$

$$q_l(p, T, q_T) = \frac{q_T - q_v^*}{1 - q_v^*}. \tag{1.59b}$$

Equation (1.59b) states that $q_l \propto q_T - q_v^*(p,T)$, which means that if rain is an isothermal and isobaric process then as q_l is reduced by precipitation then $q_T \to q_v^*(p,T)$. This suggests the following simple relaxation parametrization for precipitation:

$$\frac{dq_T}{dt} = -\frac{1}{\tau_p}\max\{q_T - q_v^*, 0\}. \tag{1.60}$$

1.3.5 Summary

In the theory of moist thermodynamics, a thermodynamical state is determined by three state variables, T, p and e instead of two in dry thermodynamics. For this reason, specifying an entropy and an enthalpy is ambiguous: there is not a single expression determined up to an additive constant but a spectrum of expressions. We have described two members of this spectrum that differ in the way they treat latent heat in diabatic considerations. In the liquid water entropy-enthalpy formulation, we do not include latent heat explicitly. When water vapor condensates and precipitates, liquid water entropy increases to account for the latent heat release. In the moist entropy-enthalpy formulation, we do include latent heat explicitly and when water vapor condensates, moist entropy is only slightly increased. Instead, it is when water vapor is added to an air parcel that its moist entropy increases.

This dual behavior is important because condensation/precipitation and evaporation are usually observed in very different geographical regions. On earth, condensation and precipitation are common in the ITCZ and in midlatitudes eddies, away from the planetary boundary layer. Evaporation,

on the other hand, is almost entirely confined to the planetary boundary layer. This means that once an air parcel has left the boundary layer, only radiative forcing and condensation/precipitation can change its entropy. Since condensation/precipitation does not substantially change the parcel moist entropy, we will assume in this thesis that moist entropy in the mid troposphere is essentially conserved on time-scales shorter than the radiative time-scale. Next, in chapter 2, we use this assumption to describe the path taken by air parcels in the poleward branch of midlatitudes eddies.

Chapter 2

Simplified Analysis of the Joint Distribution on Dry Isentropes

2.1 Context

In subsection 1.2.3 we hinted at the effects latent heat release can have in controlling the dynamics of midlatitudes climates. While these effects can be included explicitly in the study of the meridional overturning circulation by computing the circulation on moist isentropes, this method is limited by the impossibility of interpreting θ_e as a vertical coordinates due to its non-monotonic nature as a function of height. In this chapter, we answer this limitation by making use of the Pauluis et al. (2010a) mass flux joint distribution in such a way that we avoid using θ_e as a coordinate. This approach enables us to interpret the circulation on moist isentropes without using θ_e as a vertical coordinates, thus preventing the loss of vertical sigificance.

The release of latent heat generates diabatic ascents of moist air and its precise impact on the midlatitude overturning circulation has been a subject of debate. Pauluis et al. (2010a) have identified characteristics of the moist isentropic circulation that exhibit the key role moist ascents play in setting the moist circulation circulation intensity. Their analysis could not however decide whether these moist ascents were dominated by fast deep moist convective events or by slow slantwise convective motions (in the sense of Emanuel, 1983). By analyzing the climatology of moist potential vorticity and moist stratification, Korty and Schneider (2007) were able to decide in which regions each type of convection was more predominant. They found that the extratropics were generally more conducive to slantwise convection while the subtropical regions exhibited conditions that were more typical of deep convection. In this chapter, the method we are presenting provides a new set of diagnostics particularly suited for the study of the geographical distribution for each type of convection. Our approach reconciles the moist perspective of Pauluis et al. (2010a) with the dry perspective of Schneider et al. (2006) by describing the mass flux joint distribution on dry isentropes. It allows for a direct comparison of the two circulations and for an assessment of the moist circulation's vertical structure.

In section 2.2 we present the data used and introduce the joint isentropic analysis. The method required to compute the mass flux joint distribution is described and a brief introduction to its structure is offered by relating it to the circulation on dry isentropes. A transect along a latitude circle of the full joint distribution is shown, which will be routinely referred

to in the subsequent sections. In section 2.3, we describe a simplified decomposition of the joint distribution onto potential temperature surfaces into two directional flows: one Northward and one Southward. Along with this decomposition we define the moist stratification associated with each directional flows, which we use to identify midlatitudes convective regions and their related cross-isentropic transports of moisture. In section 2.4, we use the simple decomposition of section 2.3 to create an approximate circulation on moist isentropes and compare it to its exact counterpart. With the new insights gained from the decomposition, we can use the comparison to relate features of the circulation on moist isentropes to the characteristics of the directional flows' moist stratification. In section 2.5, we revisit and improve a simple theoretical model presented by Held and Schneider (1999) with the introduction of moisture. We use it to explain the relationship between surface temperature variability and the vertical structure of θ_e within our decomposition of the joint distribution.

2.2 Isentropic Circulations

2.2.1 Reanalysis Data

The data used in this chapter was obtained from the European Center for Medium-range Weather Forecasting ERA-40 reanalysis dataset and covers the period from 1981 to 2000 (Uppala et al., 2005). All the variables from the dataset lie on a $1.25^\circ \times 1.21^\circ$ regular Gaussian grid at T106 spectral truncation for 60 hybrid model levels. The meridional velocity, the air temperature and logarithm of the surface pressure are converted from a T159 spectral representation and the specific humidity from a reduced N80 Gaussian grid[1].

2.2.2 Mass Flux Joint Distribution

The analyses performed in this thesis are based on the the mass flux joint distribution described in Pauluis et al. (2010a) and computed using the method specified in the appendix. The mass flux joint distribution is defined as

$$M(\phi, \theta', \theta'_e) = 2\pi a \cos\phi \left[\int_0^{p_s} v\delta(\theta' - \theta)\delta(\theta'_e - \theta_e)\frac{dp}{g} \right], \qquad (2.1)$$

where $[\cdot]$ represents a zonal and temporal mean, $\delta(\cdot)$ corresponds to the Dirac delta function, p_s is the surface pressure, v is the meridional velocity, θ is the potential temperature and θ_e is the equivalent potential temperature. The projection variables θ' and θ'_e correspond to the potential temperature

[1] Available from the National Center for Atmospheric Research Data Support Section, dataset ds127.2.

and equivalent potential temperature in the joint isentropic phase-space. The remaining quantities are defined in Table 2.2. For a given air parcel, the two potential temperatures differ only if the parcel is moist, corresponding to a parcel with a positive specific water content, q_T. In this case the two potential temperatures are related by the following relationship:

$$\theta'_e = \theta' \exp\left(\frac{L_{v0}}{c_p T_0} q_T\right).$$

TABLE 2.1. List of functions

Symbol	Functions of	Description
$[\cdot]$	ϕ, p	Zonal and temporal average at fixed pressure;
$\langle\cdot\rangle$	ϕ, θ	Zonal and temporal average along lines of constant θ;
$\overline{(\cdot)}^*$	ϕ, θ	Mass-weighted zonal and temporal average along lines of constant θ, $\overline{(\cdot)}^* = \langle\rho_\theta \cdot\rangle \,/\, \langle\rho_\theta\rangle$;
$\langle\cdot\rangle_t$	ϕ, θ, t	Zonal average along lines of constant θ;
$\langle\cdot\rangle_{\theta_e t}$	ϕ, θ_e, t	Zonal average along lines of constant θ_e;
$\langle\cdot\rangle^{\pm}$	ϕ, θ	Directional isentropic mass flux-weighted average along lines of constant θ;
$\langle\rho v\rangle^{\pm}$	ϕ, θ	Directional mass fluxes;
M	ϕ, θ, θ_e	Mass flux joint distribution;
$\overline{(\cdot)}^N, \overline{(\cdot)}^S$		Northern (25°N to 60°N) and Southern (25°S to 60°S) midlatitudes average;

Before computing the mass flux joint distribution, we linearly interpolate the meridional velocity, the specific humidity and the temperature onto 260 equally-spaced $\sigma = \frac{p}{p_s}$ levels. The potential temperatures are then calculated using the interpolated pressure, air temperature and specific

TABLE 2.2. List of symbols

Symbol	Description
$H(\cdot)$	Heaviside function: 0 for negative arguments and 1 otherwise;
λ, ϕ, p, t	Longitude, latitude, pressure and time;
g, a	Gravitational acceleration and earth's radius;
θ, θ_e	Potential temperature and equivalent potential temperature;
ρ_θ	Isentropic layer thickness;
L_{v0}	Latent heat of vaporization at 0°C
c_p	Specific heat of air
T_0	Reference temperature (0°C)

humidity (Emanuel, 1994). We assume that moist air is an ideal mixture of gases and make use of the corresponding Clausius-Clapeyron equation. The mass flux joint distribution (2.1) is then computed numerically by using the method described in the appendix.

Figure 2.1(i) shows the mass flux joint distribution $M(\phi, \theta', \theta'_e)$ at 35°N during northern hemisphere winter. The joint distribution shows multiple peaks and large values along the $\theta' = \theta'_e$ diagonal. The large values on the diagonal represent dry mass fluxes while off diagonal peaks indicate moist mass fluxes. The joint distribution records mass fluxes according to their θ level and according to equivalent potential temperature. Some insight into the nature of the joint distribution can be gained by investigating its relation to the circulation on dry isentropes (Johnson, 1989; Held and Schneider, 1999; Schneider et al., 2006). Analyzing this simpler quantity will help illustrate the mass flux joint distribution by relating it to a well-known circulation.

2.2.3 Dry Isentropic Circulation

The dry isentropic streamfunction $\Psi_\theta(\phi, \theta')$, which measures the net mass flux *below* the isentropic surface with potential temperature θ', can either be calculated from the data or from the mass flux joint distribution, i.e.

$$\Psi_\theta(\phi, \theta') = 2\pi a \cos\phi \left[\int_0^{p_s} vH(\theta' - \theta) \frac{dp}{g} \right] = \int_0^{\theta'} \int_0^{\infty} M(\phi, \theta, \theta_e) d\theta_e d\theta, \tag{2.2}$$

where $H(\cdot)$ is the Heaviside function, equal to 1 when its argument is positive and equal to 0 otherwise.

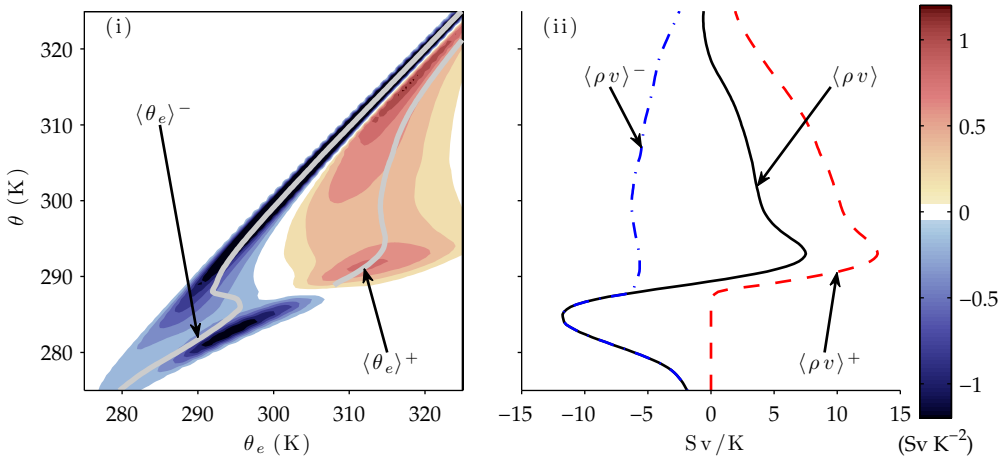

FIGURE 2.1. DJF at $\phi = 35°$N. (i) Mass flux joint distribution. Color contours are in 0.2 Sv/K^2 increments. To be discussed in subsection 2.3.3, for each directional distribution, we show $\langle\theta_e\rangle^-$ and $\langle\theta_e\rangle^+$ as white lines. (ii) the projections $\langle\rho v\rangle^-$, blue dash-dotted, $\langle\rho v\rangle^+$, red dashed, and the sum of the two, $\langle\rho v\rangle$, as a black solid line.

Figure 2.2 shows the dry isentropic streamfunction during December, January, February (hereafter DJF) and June, July, August (hereafter JJA). In the winter hemisphere, the circulation is a single equator-to-pole cell,

with high entropy air flowing poleward and lower entropy air flowing equatorward. A well-defined Hadley cell exists in the tropics and connects to a direct cell in midlatitudes. The strength of the Hadley cell does not differ substantially from the Hadley cell in the Eulerian-mean circulation as both circulations have maxima on the order of 200 Sv[2]. The extratropical extension of the circulation, which peaks around 40° latitude (both seasons and both hemispheres), is weaker than the maximum in the tropical circulation. During the northern summer, the circulation is so weak that its highest contour corresponds to 20 Sv, our lowest contour interval. For all practical purposes, the circulation on dry isentropes vanishes for this season.

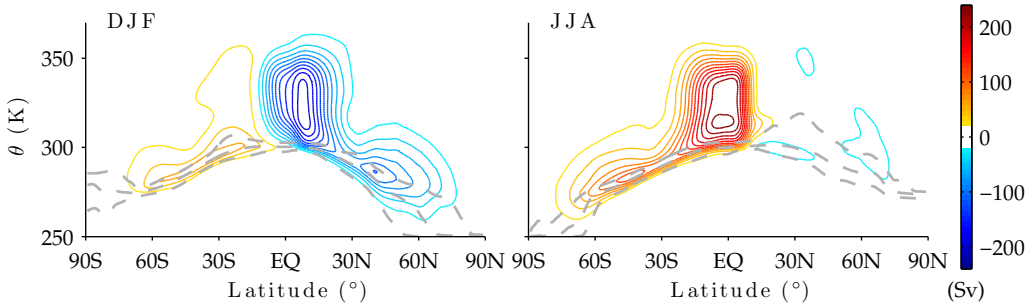

FIGURE 2.2. The streamfunction on dry isentropes (2.2). Solid contours are positive and dashed contours are negative. The contours range from 20 Sv to 240 Sv in 20 Sv increments. The three gray dashed line correspond to the 10^{th}, 50^{th} and 90^{th} percentile of the potential temperature surface distribution.

In each figures, we plot as thick gray dashed lines the tenth percentile, the median and the ninetieth percentile of the surface potential tempera-

[2] We use a Sverdrup unit to quantify the circulation where 1 Sv=10^9kg s^{-1}. For the dry isentropic circulation, this definition is equivalent to the traditional definition 1 Sv=10^6 m^3 s^{-1}.

tures distribution. With this information, one can observe that the equatorward branch of the midlatitudes circulation occurs over a narrow range of potential temperatures that are typical of surface values. The poleward branch of the circulation, on the other hand, takes place over a wider range of potential temperatures, corresponding to mid tropospheric potential temperature values.

The net meridional mass flux on isentropic surfaces, $\langle \rho v \rangle$, can be found by either taking the vertical derivative of the streamfunction (2.2), as in Held and Schneider (1999), or summing over all θ_e in the mass flux joint distribution:

$$\langle \rho v \rangle = \partial_{\theta'} \Psi_\theta(\phi, \theta') = \int_0^\infty M(\phi, \theta', \theta_e) d\theta_e. \tag{2.3}$$

The net mass flux on isentropic surfaces associated with the joint distribution at 35°N during DJF is shown in Figure 2.1(ii) as a solid line. It is southward (i.e. negative) below 290 K, with a minimum of 12 Sv/K at $\theta' = 285$K, and it becomes northward (i.e. positive) above 290 K, with a maximum of 7.5 Sv/K at $\theta' = 293$K. Note that the corresponding northward and southward regions of the mass flux joint distribution have very different equivalent potential temperature values.

The circulation on dry isentropes does not however tell a complete story. As it has been demonstrated by Schneider et al. (2006), it is possible to compute a non-trivial eddy flux of water vapor on dry isentropes. This implies that an important poleward transport of moisture exists which cannot be explained by the circulation on dry isentropes alone. The fact that such a

transport exists should not come as a surprise since poleward-moving air, which either originates from the subtropical regions or from the planetary boundary layer, must carry on average more moisture than its equatorward-moving counterpart. This means that, on a dry isentrope, poleward-moving air has a higher equivalent temperature than equatorward-moving air on the same isentrope and motions that would otherwise cancel in a dry isentropic average do not in the joint isentropic average. This is because within the joint isentropic analysis they are recorded differently, thanks to their different moisture content. This can indeed be seen in Figure 2.1 and this observation will be used next to simplify the joint distribution in order to describe it strictly on dry isentropes. This will serve to better understand the mass flux joint distribution and to simplify its analysis.

2.3 Simplified Mass Flux Joint Distribution

2.3.1 Directional Mass Fluxes

The fact that two air masses with different moisture content moving in opposite directions cancel each other's mass flux within a dry isentropic average but not within the joint isentropic average is key to this study. To see this we refer to the midlatitudes joint distribution of Figure 2.1(i). In this figure, on every horizontal lines above the line $\theta = 288\text{K}$, there are both positive (solid) and negative (dashed) contours. Since the procedure to go from the joint distribution to the net mass fluxes on dry isentropes in equation (2.3) requires the calculation of an integral along horizontal lines, important cancellations between the northward (positive) and southward (negative) flows will occur on dry isentropes above 288K.

To study the joint distribution on dry isentropes while avoiding these cancellations, we define the northward, $M^+(\phi, \theta, \theta_e)$, and the southward, $M^-(\phi, \theta, \theta_e)$, joint distributions on isentropic filaments by

$$M^+(\phi, \theta, \theta_e) = \max\{M(\phi, \theta, \theta_e), 0\}, \tag{2.4a}$$

$$M^-(\phi, \theta, \theta_e) = \min\{M(\phi, \theta, \theta_e), 0\}. \tag{2.4b}$$

In Figure 2.1(i) the southward M^- and northward M^+ joint distributions correspond to the solid and dashed contours, respectively. As such, the directional decomposition does not discard any information and the joint distribution can be recovered by adding the two components: $M(\phi, \theta, \theta_e) = M^+(\phi, \theta, \theta_e) + M^-(\phi, \theta, \theta_e)$. The primary advantage of the directional de-

composition is that the individual southward and northward contributions are sign-definite, which makes it possible to consider each one as a standard two-dimensional distribution at every latitude.

We can now imitate the procedure of equation (2.3) by using the directional joint distributions (2.4) instead of the full joint distribution. This defines the northward $\langle \rho v \rangle^+$ and southward $\langle \rho v \rangle^-$ directional fluxes:

$$\langle \rho v \rangle^+ = \int_0^\infty M^+(\phi, \theta, \theta_e) d\theta_e,$$
$$\langle \rho v \rangle^- = \int_0^\infty M^-(\phi, \theta, \theta_e) d\theta_e,$$

and this time this operation causes no cancellations. The directional fluxes at 35°N DJF are shown in Figure 2.1(ii) as a dashed line for the northward fluxes and as a dot-dashed line for the southward fluxes. While the projections that produce the directional fluxes discard informations about θ_e, they still hold more informations than the net mass flux on dry isentropes $\langle \rho v \rangle$, a quantity that can be recovered by adding the two directional fluxes, i.e. $\langle \rho v \rangle = \langle \rho v \rangle^+ + \langle \rho v \rangle^-$.

The upper panels of Figure 2.3 and Figure 2.4 show the directional fluxes during DJF and JJA, respectively. In all panels, the thick gray dashed line corresponds to the median surface potential temperature. The upper left panels show the northward directional fluxes $\langle \rho v \rangle^+$ and upper right panels show the southward directional fluxes $\langle \rho v \rangle^-$. The total mass flux on potential temperature surfaces $\langle \rho v \rangle$ is shown in the lower right panels. As noted earlier, adding the two directional fluxes to produce the lower right panels result in significant cancellations. A measure of these cancellations,

identified by $\langle \rho v \rangle'$, is plotted in the lower left panels of Figure 2.3 and Figure 2.4. It is calculated by

$$\langle \rho v \rangle' = \min \left\{ \langle \rho v \rangle^+ , - \langle \rho v \rangle^- \right\}, \tag{2.6}$$

and its physical significance is addressed later in subsection 2.3.2.

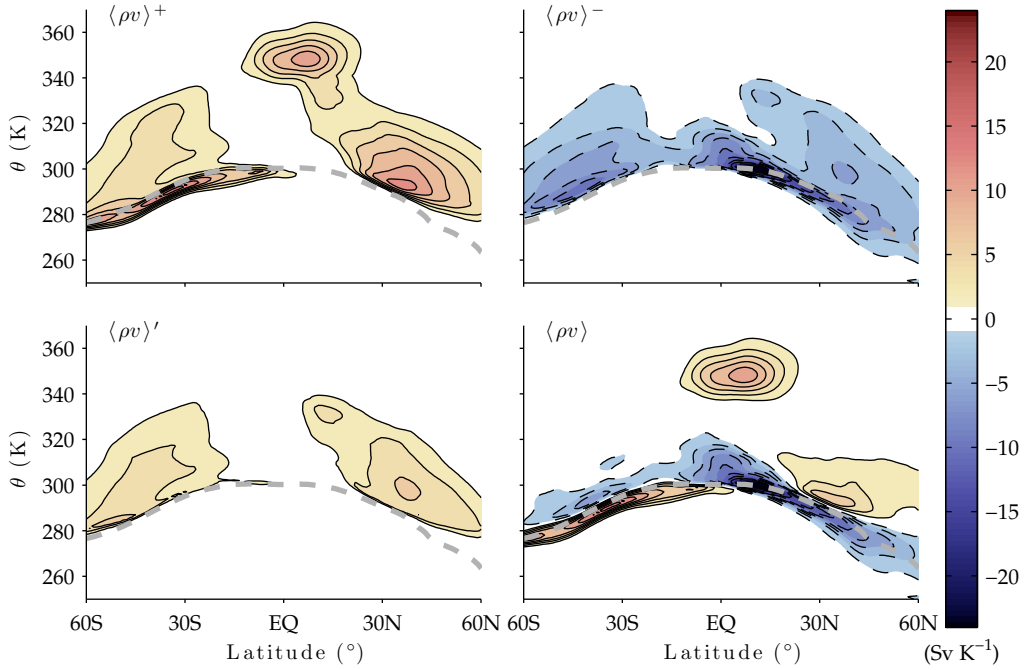

FIGURE 2.3. DJF Mass fluxes on potential temperature surfaces. Upper left, Northward fluxes and upper right, Southward fluxes; lower left, $\langle \rho v \rangle'$ of equation (2.6), a quantity that we call the Moist Recirculation in subsection 2.3.2; lower right net mass fluxes. Contours are in 2 Sv K^{-1} increments. The gray dotted line show the median surface θ.

The lower right panel of Figure 2.3 and Figure 2.4 corresponds to the net mass fluxes on potential temperature surfaces, $\langle \rho v \rangle$, and are equal through equation (2.3) to the vertical derivative of the dry isentropic circulation shown in Figure 2.2. One can identify the Hadley cell by the strong pole-

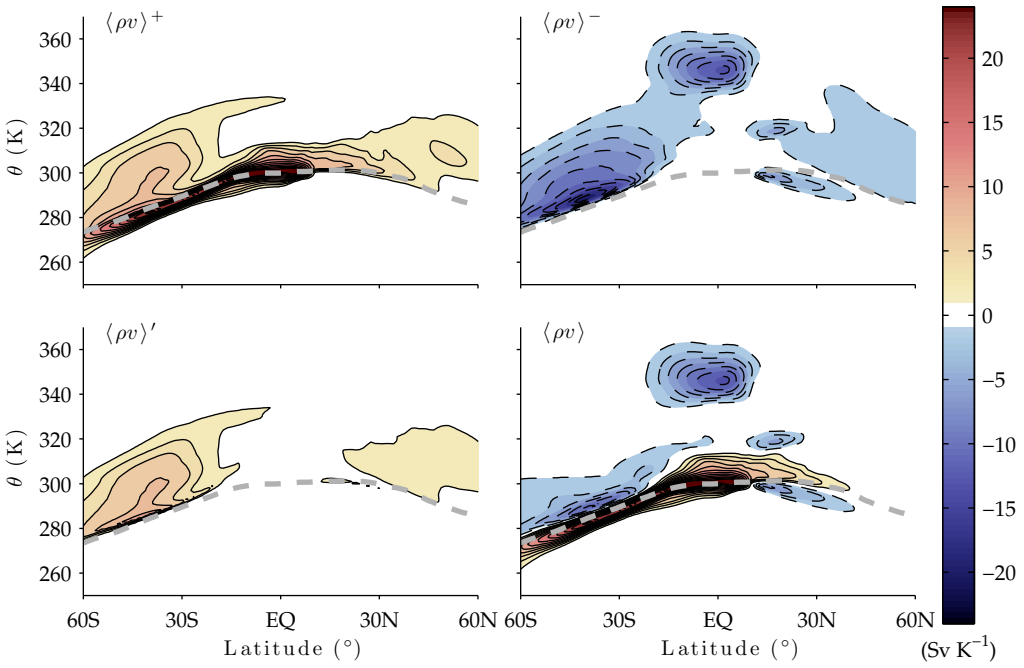

FIGURE 2.4. JJA Mass fluxes on potential temperature surfaces. Same as Figure 2.3.

ward mass fluxes at $\theta \approx 350$K and the strong equatorward surface fluxes at $\theta \approx 300$K between the equator and 30° in the winter hemisphere. The tropical surface flow has a warm component coming from the winter hemisphere and a cooler — and weaker — component coming from the summer hemisphere.

The mass fluxes associated with the midlatitudes overturning circulation can be easily identified in the winter hemispheres. Their equatorward flow is intense and occurs within a narrow range of potential temperatures mostly below the median surface temperature (see Held and Schneider, 1999, for a detailed analysis). It extends naturally to become the surface flow of the Hadley cell in the subtropics. Their poleward flow is weaker and spread over a broad range of potential temperatures from surface

values to approximatively 300K-310K. This mid tropospheric poleward flow becomes important approximately at the latitude where the Hadley cell's poleward flow becomes negligible. The two poleward flows are nevertheless disconnected: the midlatitudes poleward flow does not appear to be a natural extension of the poleward Hadley cell's flow.

This apparent separation between the two winter poleward flows disappears in the directional fluxes. Indeed, the poleward directional fluxes in the Hadley cell are now connected to the midlatitudes poleward directional fluxes (see upper left panel of Figure 2.3 for NH DJF and the upper right panel of Figure 2.4 for the SH JJA). Such a connection has been deduced by other studies (Pierrehumbert, 1998; Schneider et al., 2006) and is related to eddies extracting moisture from the subtropics to the midlatitudes. Because the net mass fluxes $\langle \rho v \rangle$ are vanishing within the connection, there are corresponding equatoward directional fluxes (NH upper left, SH upper right in Figure 2.3 and NH upper right, SH upper left in Figure 2.4) to cancel the poleward directional fluxes connecting the subtropics to the midlatitudes. For DJF, the subtropical NH equatorward directional fluxes span potential temperature values from 320K to 340K while for JJA the subtropical SH equatorward directional fluxes is not as wide and spans only values from 320K to 330K.

The midlatitudes equatorward directional fluxes of both seasons and both hemispheres have a much broader θ extent than the corresponding equatorward fluxes in the net mass fluxes $\langle \rho v \rangle$ and are distributed across the whole mid troposphere. While these mid tropospheric mass fluxes are not as intense as the surface equatorward fluxes, they spread from

surface θ values to about 310K-320K and span most of the hemispheres from about 20° to the pole. Because the net mass fluxes are weak in this mid tropospheric region, there are corresponding poleward directional fluxes to cancel the equatorward directional fluxes. Consequently, the θ extent of the poleward directional fluxes is similar to that of the mid tropospheric equatorward directional fluxes. This extent is also broader than the θ extent of poleward fluxes in the midlatitudes net mass fluxes.

Before moving forward, we want to bring special attention to the NH summer. We have already observed that the dry circulation (right panel of Figure 2.2) was weak during that season. Correspondingly, the net mass fluxes (lower right panel of Figure 2.4) for that season are weak relative to the NH winter net mass fluxes. The mass fluxes revealed by the directional fluxes (NH of upper panels in Figure 2.4) are also weak relative to the directional fluxes in the NH winter but not as much as the net mass fluxes are between the two seasons. Indeed, over the region from 30°N to 60°N the poleward directional fluxes $\langle \rho v \rangle^+$ are only about 3 times stronger for DJF than for JJA (upper right panel of Figure 2.3 vs Figure 2.4) whereas poleward fluxes in the net mass fluxes essentially vanish for JJA. This means that eddies in the NH sumer have a strong moisture components with the majority of the poleward heat transports being provided through moist ascensions. During that season, on a given dry isentrope, the moist poleward component mostly cancels the drier equatorward component, thus leading to a net poleward transport of latent heat accompanied by a vanishing transport of sensible heat. A similar cancellation occurs in both hemispheres and both seasons albeit in a less pronounced manner.

2.3.2 Moist Recirculation

These mid tropospheric cancellations arise because there remains moisture fluxes that are not accounted for by the circulation on dry isentropes. These cancellations, resulting from the addition of the two directional fluxes, lead to net mass fluxes on dry isentropes that are significantly weaker than either directional fluxes. In the mid troposphere, the net mass fluxes are poleward which means that the magnitude of the mass flux cancellation will be equal to the magnitude of the equatorward directional fluxes. More generally, the cancellation $\langle \rho v \rangle'$ between the two directional fluxes will be equal to the smallest, in absolute value, of the two fluxes as formulated in equation (2.6). These cancellations should be understood as the net poleward transport of mass in moist regions that is balanced exactly by an equatorward transport of mass in dry regions. The resulting recirculation — that we will more specifically refer to as the Moist Recirculation (hereafter MR) — is plotted in the lower left panel of Figure 2.3 and Figure 2.4. The bulk of the MR is located above the surface median potential temperature in the midlatitudes, between 30° and 60°. Its extent in θ is similar to the corresponding extent of midlatitudes directional fluxes and its strength is comparable to that of the equatorward directional fluxes.

The winter hemispheres MR extend deep into the subtropics, as low as 15°, attaining their peak in the mid-to-upper troposphere at $\theta \approx 330$K and vanishing for potential temperatures close to surface values. This peak corresponds to the lower portion of the Hadley circulation's poleward mass fluxes, showing that the MR is responsible for the connection between the subtropical atmosphere and the midlatitudes. In the winter midlatitudes,

the MR exhibits intense mass fluxes at 37° latitudes and $\theta \approx 300$K, of a magnitude of 3 Sv K^{-1} (DJF) and 4 Sv K^{-1} (JJA). During the Southern winter, there are even larger mass fluxes in the lower troposphere and further poleward. These are however of a different nature, for the most part related to surface fluxes, which will be described extensively in section 2.5.

The concept of the MR serves to quantify the mass fluxes the can only be resolved by a moist isentropic average. This means that it is particularly suited as tool to improve our interpretation of the circulation during the northern summer. The MR in the lower left panel of Figure 2.3 and Figure 2.4 show that the northern hemisphere's summer MR mass fluxes have about a half of their winter value. This means that the weak summer circulation is misleading because it results from the cancellation of the MR in the dry isentropic average.

2.3.3 Thermodynamics and moist ascent

The MR arises when there is a difference between the mean moisture content (or θ_e value) of the poleward mass fluxes and equatorward mass fluxes on a dry isentrope. The directional mass flux joint distributions (2.4), because they are sign-definite quantities, can be used to obtain this moisture contribution in terms of mean equivalent potential temperatures

$\langle\theta_e\rangle^+$ and $\langle\theta_e\rangle^-$ transported by each of the directional fluxes:

$$\langle\theta_e\rangle^+ = \int_0^\infty \theta_e M^+(\phi,\theta,\theta_e)\,d\theta_e \Big/ \langle\rho v\rangle^+ , \tag{2.7a}$$

$$\langle\theta_e\rangle^- = \int_0^\infty \theta_e M^-(\phi,\theta,\theta_e)\,d\theta_e \Big/ \langle\rho v\rangle^- . \tag{2.7b}$$

Figure 2.1(i) shows as thick white lines these mean equivalent potential temperatures superimposed on the mass flux joint distribution at 35°N during DJF. The mean equivalent potential temperature of the southward — in this case equatorward — flux (shown by the thick white line on the dashed contours) begins at a θ value that corresponds to surface air and with a $\langle\theta_e\rangle^-$ value consistent with high relative humidity. This air is part of equatorward flows associated with eddies in midlatitudes that will join the Hadley cell surface branch if it moves sufficiently equatorward. Moving along the $\langle\theta_e\rangle^-$ curve, one reaches at $\theta = 286$K a sharp transition from a moist $\langle\theta_e\rangle^-$ to one that is along the line $\langle\theta_e\rangle^- = \theta$, the line that corresponds to dry air. The level at which this occurs is approximately the same at which the net mass fluxes vanishes (see Figure 2.1(ii)). Above this sharp transition, $\langle\theta_e\rangle^-$ remains along the main diagonal and, hence, remains dry.

The average equivalent potential temperature of the northward — in this case poleward — flux begins at $\theta = 290$K with a value of $\langle\theta_e\rangle^+ \approx 310$K. It then increases to $\langle\theta_e\rangle^+ = 315$K at $\theta = 295$K, the level at which the northward fluxes peak (see the dashed line in Figure 2.1(ii)), and remains roughly constant until $\theta = 305$K, above which level it again increases with increasing θ. For high θ levels, however, the distribution of θ_e in the poleward flow becomes skewed indicating that the mean $\langle\theta_e\rangle^+$ no

longer provides an accurate description of the flow. Below this level, it is nevertheless significant that the first moment of the northward distribution varies little in the vertical. This indicates that the poleward mass fluxes are connected to the lower troposphere which can only happen if there are moist ascents on the large scale in the poleward flow.

By construction, the averages (2.7) created using the mass flux joint distribution preserve the total θ_e flux on isentropic surfaces, i.e.

$$\langle \theta_e \rho v \rangle = \langle \theta_e \rangle^+ \langle \rho v \rangle^+ + \langle \theta_e \rangle^- \langle \rho v \rangle^- . \tag{2.8}$$

This means that the decomposition into directional fluxes and directional equivalent potential temperature accurately represents the net moist entropy fluxes. The NH summer stands out since its the net mass fluxes on dry isentropes vanish for all practical purposes. During that season the flux of θ_e on the left hand side of equation (2.8) will thus be the mass-weighted zonal-mean eddy flux of θ_e on dry isentropes and the right hand side will be equal to $(\langle \theta_e \rangle^+ - \langle \theta_e \rangle^-) \langle \rho v \rangle'$. When the net mass fluxes on dry isentopres vanish, this last expression becomes synonymous to an eddy flux of θ_e, and eddy flux that is driven by an "eddy mass flux" $\langle \rho v \rangle'$ that transports θ_e according to the difference $\langle \theta_e \rangle^+ - \langle \theta_e \rangle^-$.

In the southern hemisphere and during DJF of the northern hemisphere the net mass fluxes do not vanish and as a consequence the MR cannot be exactly identified with an eddy mass flux. It is nevertheless convenient to assume that the opposing mass fluxes of the MR have a typical equivalent potential temperature equal to their respective directional θ_e: the northward

mass fluxes occur at $\langle\theta_e\rangle^+$ and the southward fluxes, at $\langle\theta_e\rangle^-$. With this assumption, the meridional flux of θ_e associated with the northward branch of the MR will be equal to $\langle\theta_e\rangle^+ \langle\rho v\rangle'$ and the one associated with the southward will be equal to $-\langle\theta_e\rangle^- \langle\rho v\rangle'$.

Figure 2.5 and Figure 2.6 show the directional mean equivalent potential temperatures (2.7). In the same figures, we have reproduced the MR from the lower left panel of Figure 2.3 and Figure 2.4 for DJF and JJA, respectively. The directional θ_e are plotted according to their direction within each hemisphere, poleward or equatorward, instead of according to their absolute direction, northward or southward. This serves to emphasize the similitudes between the poleward θ_e and between the equatorward θ_e. In the remainder of this subsection, we proceed to explain the meaning of these figures.

The difference between the two directional equivalent potential temperatures, $\langle\theta_e\rangle^+ - \langle\theta_e\rangle^-$, being generally positive in the NH and generally negative in the SH, confirms our claim that the MR are related to a poleward flux of θ_e on dry isentropes. Since a difference of θ_e on a fixed dry isentrope is proportional to the difference in latent heat,

$$\langle\theta_e\rangle^+ - \langle\theta_e\rangle^- \sim \frac{L_{v0}}{c_{pd}}(\langle q_T\rangle^+ - \langle q_T\rangle^-),$$

it implies that the MR transports latent heat poleward. In this expression, we have denoted by $\langle q_T\rangle^+$ and $\langle q_T\rangle^-$ the specific humidity associated with the directional components, that can be computed by using equations (2.7) and replacing θ_e by q_T.

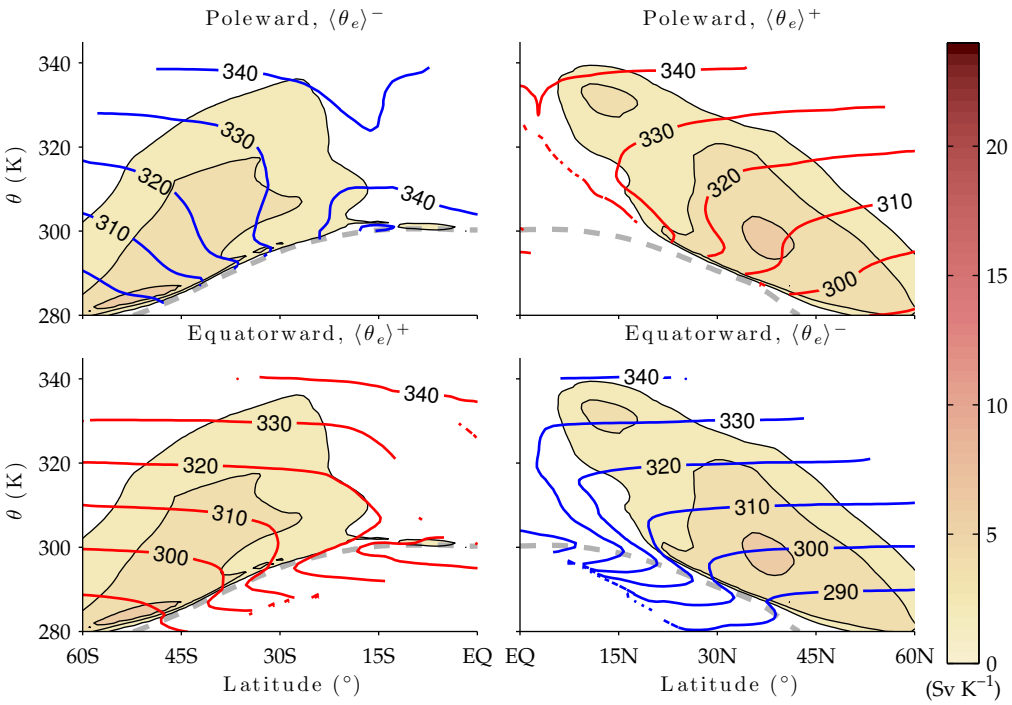

FIGURE 2.5. DJF Equivalent potential temperature on directional fluxes. In shaded contours, the MR, with the same contours as Figure 2.3 and Figure 2.4. In the upper panels, the thick solid curves show the equivalent potential temperature on the *poleward* directional fluxes $\langle\theta_e\rangle^+$ and $\langle\theta_e\rangle^-$, respectively. In the lower panels, the thick solid curves show the equivalent potential temperature on the *equatorward* directional fluxes $\langle\theta_e\rangle^+$ and $\langle\theta_e\rangle^-$, respectively. The gray dashed line corresponds to the median surface potential temperature.

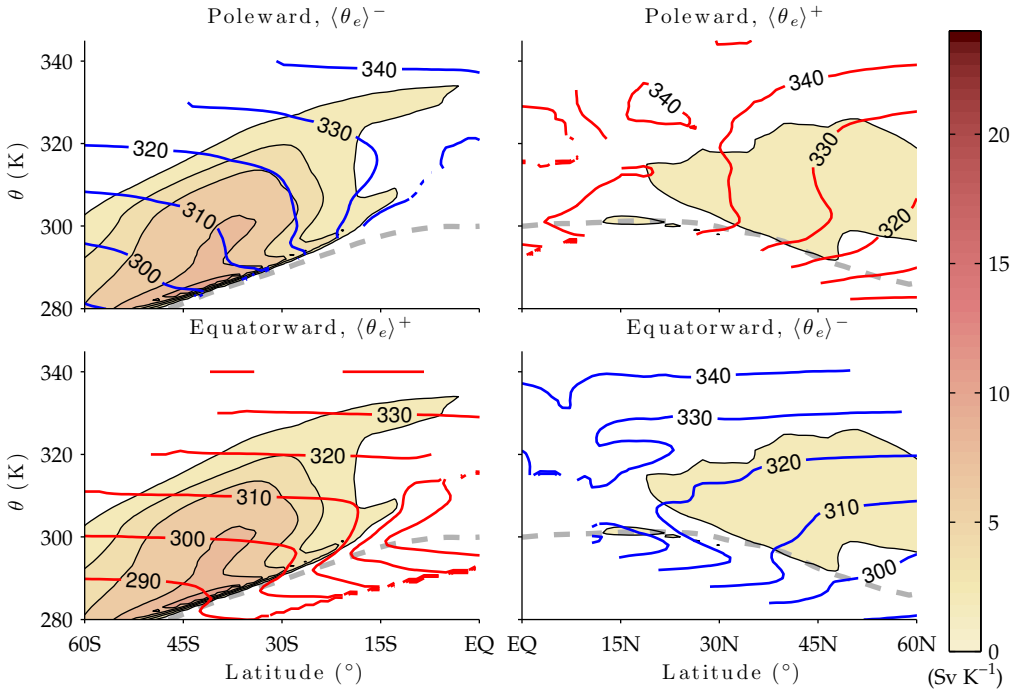

FIGURE 2.6. JJA Equivalent potential temperature on directional fluxes. Same as Figure 2.5.

The purpose of the directional θ_e profiles however goes beyond an assessment of the θ_e fluxes by the MR and can be used to discuss the thermodynamic cycle of midlatitudes baroclinic eddies and the moist vertical stability profiles experienced by the different branches of these eddies. To investigate the latter, we first look at the equatorward directional θ_e in the lower panels of Figure 2.5 and Figure 2.6. The midlatitudes of both seasons and both hemispheres share many similarities, like for instance the large values of θ_e in their lower part, below the median surface θ. This corresponds to mass fluxes occurring within the planetary boundary layer. They are also all mostly dry above the median surface potential temperature which can be deduced by an equatorward directional θ_e that is aligned with lines of constant θ.

The vertical structure of the poleward θ_e (upper panels of Figure 2.5 and Figure 2.6) is also similar across seasons and hemispheres but exhibit marked differences between the subtropics and the midlatitudes. In the subtropics and up to 35° (50°N for NH JJA), the vertical profile exhibits a local minimum at mid tropospheric θ values of around 310K. The consequence of such a vertical profile can be better understood by considering, for example, a typical surface parcel at 29°N in the NH of DJF (upper right panel of Figure 2.5). It lies on the $\langle\theta_e\rangle^+ = 320$K curve at $\theta = 295$K. At the beginning of its poleward motion, it has a mostly horizontal, i.e. dry isentropic, motion until $\phi \approx 32$N. If this parcel is to keep moving poleward while preserving its $\langle\theta_e\rangle^+$, it has to do so at the much higher θ value of about 310K because no poleward mass fluxes have $\langle\theta_e\rangle^+ = 320$K below this level. Such a discontinuous path suggests a fast adjustment that can be attributed to deep convection.

In midlatitudes, poleward of 35° (50°N for NH JJA), the poleward θ_e is increasing with increasing θ. If we consider a typical parcel at median surface θ that is moving poleward in this region, the issue of a discontinuous path does not arise, contrary to the situation in the subtropics. Indeed, if we take for example a parcel at 40°N, $\theta = 290$K on the line $\langle\theta_e\rangle^+ = 310$°K in the NH of DJF (upper right panel of Figure 2.5), it will be able to follow continuously its $\langle\theta_e\rangle^+ = 310$K curve all the way to the pole. Such a smooth path excludes deep convective adjustments, instead suggesting that the large scale moist ascents are due to slantwise convective motions.

To illustrate the thermodynamics cycle in midlatitudes, we isolate the $\langle\theta_e\rangle^+ = 310$K and $\langle\theta_e\rangle^- = 310$K curves from the right panels of Figure 2.5

and zoom in to produce Figure 2.7. A moist air parcel begins by flowing poleward along a dry isentrope and starts cooling while retaining its θ_e value. At around 40°N it undergoes a limited convective adjustment in the form of a vertical path from $\theta \approx 293$K to $\theta \approx 300$K, after which it can continue along a slanted moist isentrope to the upper and poleward edge of the MR and ultimately will reach the $\theta = 310$K isentrope. If this parcel comes back towards the equator within an eddy time-scale, its motion will remain adiabatic and it must therefore return along the line $\langle\theta_e\rangle^- = 310$K, which is a horizontal line that confounds itself with the $\theta = 310$K isentrope. In the absence of liquid water to evaporate, it will remain at $\langle\theta_e\rangle^- = 310$K.

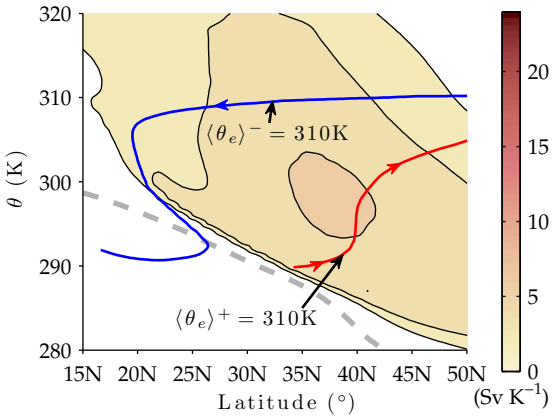

FIGURE 2.7. Diagram explaining moist ascents. A composite diagram of left panels of Figure 2.5. The lowermost curve indicates $\langle\theta_e\rangle^+ = 310$K and the uppermost, $\langle\theta_e\rangle^- = 310$K. Arrows were added to emphasize the direction of the flow. The shaded contours are as in Figure 2.5(ii) and indicate the moist residual mass flux. The gray dashed line represents the median of the surface distribution.

The portion of the $\langle\theta_e\rangle^- = 310$K curve that lies south of 25°N exhibit a "S" shape that requires some precision because heat fluxes become important in the region. The air parcels going southward along the upper branch of the $\langle\theta_e\rangle^- = 310$K curve are dry parcels displaced by the MR. Because the MR is weak in the region, we can assume that on average these air parcels are moving slower than before and their motion becomes more affected by radiative cooling. As they are cooled, these air parcels eventually leave

the $\langle\theta_e\rangle^- = 310$K curve and enter the planetary boundary layer somewhere within the subtropics. There, they get mixed with near-surface air and subsequently moistened, which explains the relatively high $\langle\theta_e\rangle^-$ values found around the surface median potential temperature. These air parcels then pursue their equatorward motions as they increase even more their moisture content. Because their θ value can be assumed to be relatively unchanged by this process, these air parcels will remain convectively stable until they reach the ITCZ.

2.3.4 Relation to Mass-Weighted Average

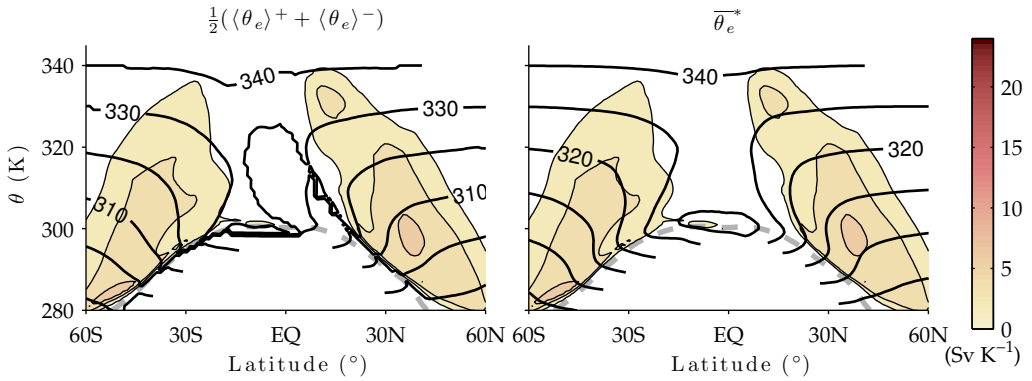

FIGURE 2.8. Comparison between the climatology inferred by the directional profiles, right panel, and the mass-weighted climatology, left panel.

In the presentation of subsection 2.3.3, we observed that the vertical θ_e profile obtained using the poleward directional flow is fundamentally different from the one obtained using the equatorward directional flow. Within the poleward profile, it could be observed that the likely path of air parcels in the poleward branch of the MR was connecting the surface with the upper part of the MR, an indication that the moist stability experienced

by these air parcels is lower than the dry stability. In the equatorward profile, on the other hand, the observed paths corresponded to dry isentropes and consequently the moist stability by air parcels in the MR equatorward branch has to be comparable to the dry stability. In this section, we aim to relate this decomposition of the moist stability to the climatological moist stability, a more traditional measure of stability that has been used to investigate a similar problem in several other studies (Juckes, 2000; Frierson, 2008).

In a geophysical turbulent flow, one can adopt a TEM-like perspective and assume that turbulent perturbations are weak departures from an otherwise zonally-symmetric mean state. This assumption would demand the two directional profiles to be relatively similar as both would be small perturbations from the mean. Because the directional profiles were shown to be dramatically different, this perspective does not seem to agree with our observations.

An alternative perspective would be to assume the turbulence to be made exclusively of large departures with a mean state that is not representative of a typical atmospheric state. In such a case, the mean state would essentially be a mathematical construct, equal to the mean of the actual states attained through turbulent large perturbations. The dramatically different directional profiles are such a kind of actually achieved atmospheric states that are generated by strong geophysical turbulence. If we assume that we are indeed in such a regime, we should expect the climatological θ_e profile along dry isentropes to be approximately an average between the

poleward and equatorward θ_e profiles:

$$\overline{\theta_e}^* \approx \frac{1}{2}(\langle\theta_e\rangle^+ + \langle\theta_e\rangle^-). \tag{2.9}$$

The right hand side and the left hand side of this equation are shown in Figure 2.8. They exhibit a stunning resemblance in midlatitudes, less so in the subtropics. This seems to confirms our claim that the mean state of such a turbulent flow can be described simply by the mean climatology in each of the poleward and the equatorward branch of the MR.

This has profound implications because it says that not only does the poleward θ_e profile describes moist ascents in the poleward branch of midlatitudes eddies but it also determines half of the mean moist stratification. Since the other half, corresponding to the θ_e profile of equatorward branch, has a moist stratification equal to the dry stratification, it suggests that the climatological moist stratification is entirely determined by the poleward branch. To understand what sets the moist stratification in the midlatitudes, one has need only to understand what sets the typical θ_e value of the poleward directional fluxes.

2.4 Moist Isentropic Circulation

The preceding section describes the meridional mass fluxes and their associated profile of equivalent potential temperature with θ as a vertical coordinate. Because the potential temperature is stratified everywhere except within the boundary layer on the large scales, this analysis of the directional fluxes and the directional profiles of θ kept a notion of vertical position. This allowed to associate moist equatorward flows to the lower troposphere and to observe that the bulk of the MR lied in the mid-to-high troposphere.

In Pauluis et al. (2010a) it was noted that one of the key quantities that can be extracted from the joint distribution is the circulation on moist isentropes. It is important because it allows to diagnose meridional transports of θ_e, which include the transports of latent heat. Moreover, θ_e approximates Lagrangian trajectories better than θ where condensation and precipitation are important. Its main limitation comes from the inability to understand θ_e as a vertical coordinate due to its lack of stratification in the lower troposphere. This limitation could be mitigated if we could give a physical interpretation of the circulation on moist isentropes based on the insights obtained from the previous sections. This would be an easy task if it was possible to recover the circulation on moist isentropes by using directional fluxes and directional θ_e profiles only.

The circulation on moist isentropes is analyzed using the moist isentropic streamfunction $\Psi_{\theta_e}(\phi, \theta_e')$, which measures the net meridional flux of air masses with equivalent potential temperature θ_e less than the phase-space equivalent potential temperature θ_e'. It adopts a formulation that is many

points similar to the dry streamfunction (2.2) and can also be calculated from the mass flux joint distribution:

$$\Psi_{\theta_e}(\phi, \theta_e') = 2\pi a \cos\phi \left[\int_0^{p_s} v H(\theta_e' - \theta_e) \frac{dp}{g} \right], \tag{2.10a}$$

$$= \int_0^{\theta_e'} \int_0^{\infty} M(\phi, \theta, \theta_e) d\theta d\theta_e, \tag{2.10b}$$

$$= \int_0^{\infty} \langle \rho v \rangle^+ \left(\int_0^{\theta_e'} \frac{M^+}{\langle \rho v \rangle^+} d\theta_e \right) - \langle \rho v \rangle^- \left(\int_0^{\theta_e'} \frac{M^-}{\langle \rho v \rangle^-} d\theta_e \right) d\theta. \tag{2.10c}$$

As in the rest of this paper, we drop the primes for the phase-space θ_e to streamline the discussion.

The directional fluxes and directional θ_e can be processed to approximate the circulation on moist isentropes in a simple way. The procedure transforms the curves of constant directional θ_e in Figure 2.5 and Figure 2.6 into the vertical axis while carefully recording the associated directional fluxes. In the subtropical poleward fluxes the directional θ_e is not increasing monotonically with θ which led to the interpretation that poleward motions along moist isentropes have to be discontinuous. The procedure to recover the circulation on moist isentropes will effectively "fold" the corresponding fluxes, bundling together low-level air with upper tropospheric air. This folding will also occur in the equatorward fluxes, with the surface fluxes being folded unto mid tropospheric fluxes. This last folding will lead to cancellations with the poleward fluxes, fluxes that can have θ_e values comparable to surface values. As it can be seen in the lower panels of Figure 2.5 and Figure 2.6, this effect is important only for latitudes equatorward of 40°.

The procedure to compute the corresponding folded streamfunction mimics the computation of the moist streamfunction (2.10) but uses the directional fluxes and their directional θ_e:

$$\Psi^{\text{fold}}_{\theta_e}(\phi, \theta_e) = \int_0^\infty \langle \rho v \rangle^+ H(\theta_e - \langle \theta_e \rangle^+) - \langle \rho v \rangle^- H(\theta_e - \langle \theta_e \rangle^-) d\theta. \quad (2.11)$$

If the decomposition of the joint distribution into directional fluxes was exact, then $\Psi^{\text{fold}}_{\theta_e}$ would be equal to the moist streamfunction (2.10). In fact, the folded streamfunction (2.11) approximates the exact streamfunction by reducing the directional θ_e distributions $M^+ / \langle \rho v \rangle^+$ and $M^- / \langle \rho v \rangle^-$ to δ-functions centered at their respective mean value. The quality of the decomposition at recovering the circulation on moist isentropes can be assessed by comparing these two quantities in Figure 2.9 where we have plotted the exact moist circulation (2.10) in the left panels and the folded moist circulation (2.11) in the right panels for both seasons.

Qualitatively, the folded circulation is very similar to the exact circulation. The folded circulation is narrower in the θ_e direction, primarily in the subtropics. This is a consequence of the cancellations arising from the folding procedure as previously described. The folded circulation tends to have sharper gradients, a consequence of assuming that directional fluxes occur at their directional θ_e, which neglects higher moments of the directional distribution of θ_e. Moreover, these sharper gradients occur wherever the directional θ_e is not a monotonic function of θ, which occurs significatively only in the poleward flow around 30°.

To assess the discrepancy between the two circulations more quantita-

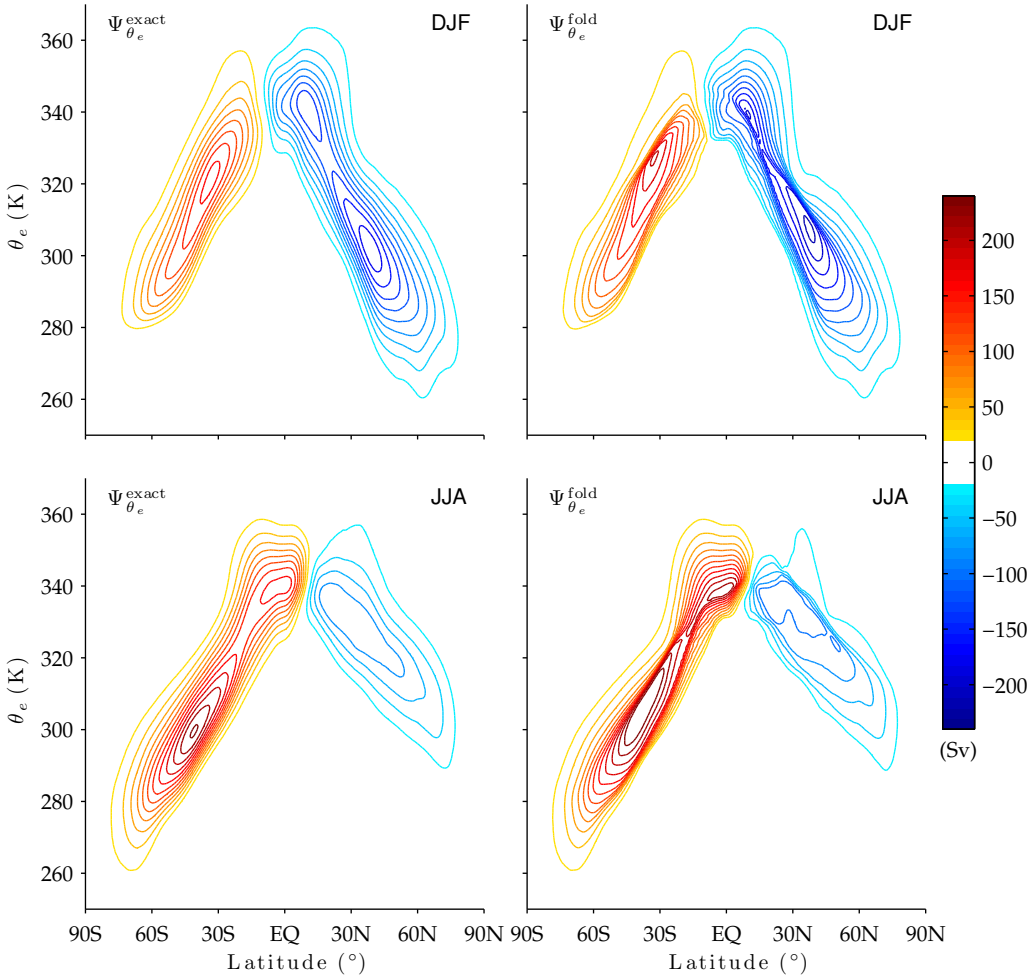

FIGURE 2.9. Circulations on moist isentropes: exact and folded. In the left panels, the exact circulation on moist isentropes and in the right panels, the circulation on moist isentropes as recovered using the directional decomposition. Contours are the same as in Figure 2.2, from 20 Sv to 240 Sv in 20 Sv increments.

tively, we calculate the total mass transport (Pauluis et al., 2010a):

$$\Delta\Psi^{\text{exact}}_{\theta_e}(\phi) = \max_{\theta'_e}\left\{\Psi^{\text{exact}}_{\theta_e}(\phi,\theta'_e)\right\} - \min_{\theta'_e}\left\{\Psi^{\text{exact}}_{\theta_e}(\phi,\theta'_e)\right\}, \tag{2.12}$$

and similarly for the folded circulation $\Psi^{\text{fold}}_{\theta_e}$. The total mass transport is plotted in Figure 2.10, with the solid line corresponding to the approximate transport and the dashed line to the exact transport.

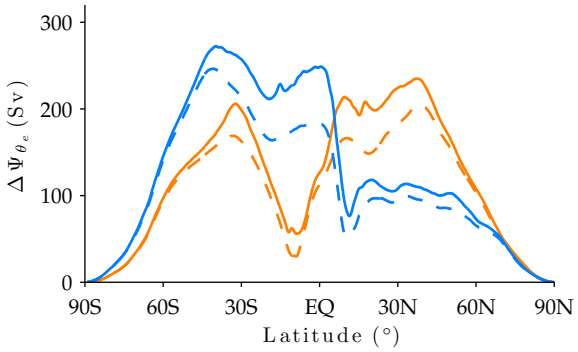

FIGURE 2.10. Total mass transport on moist isentropes: exact and folded. Solid curves show the folded total circulation on moist isentropes and dashed curves show the exact total circulation on moist isentropes while orange curves are for DJF and blue curves are for JJA.

For each season, the exact and the folded total mass transports are qualitatively similar. The winter season circulation exhibits two maxima, one in the subtropics corresponding to the Hadley cell and one in the midlatitudes, related to moist eddies. The summer season circulation exhibit only one maxima, somewhere around 30°. In the NH, this maxima is very weak and the total mass transports are not changing much with latitude. The folded circulations tend to over-estimate these maxima with errors in the folded circulation on the order of 10-15% in midlatitudes. This over-estimate is a direct consequence of our reduction of the directional θ_e distributions to δ-functions, which neglects the variance at a leading order error and results in a quadratic correction.

The good agreement between the two methods signifies that our inter-

pretations of the directional fluxes and directional θ_e profiles can be used to understand the circulation on moist isentropes. In particular, it can be seen that the maximum of the moist circulation corresponds to the region where the poleward θ_e becomes an increasing function of θ. In this region, parcels moving poleward are not required to follow a discontinuous path along a moist isentrope. This was said to mean that deep convection is not a important adjustment mechanism for the region. It has the implication that the winter circulation on moist isentropes peaks in the region where moist ascents are relatively slow and related to slantwise convection.

From what we have learned in the previous sections, it can be deduced that the difference between the strengths of the circulation on moist isentropes and the circulation on dry isentropes is due to the MR. These MR contribute largely to the circulation on moist isentropes in the midlatitudes and are responsible for making it relatively uniform across hemispheres and seasons. Even in the summer hemispheres, where the circulation on dry isentropes is weak, the MR are observed to contribute significantly to the meridional transport of energy.

2.5 Moist Eddies and Low-Level Flows

We have shown that it is possible to obtain a simplified description of the mass flux joint distribution by using directional fluxes and directional θ_e. This simplified distribution has been used to both recover exactly the circulation on dry isentropes and approximately the circulation on moist isentropes, with a good degree of accuracy. It also provided a physical interpretation of the moist processes occurring within those circulations. In this section, we describe a simple model of the low-level flow that links the observed structure of the poleward θ_e to surface humidity and potential temperature.

The importance of moisture in the surface flow was highlighted by the thermodynamic structure of poleward directional fluxes linking surface air parcels to the upper troposphere through moist ascents. It is thus expected that surface thermodynamical characteristics of baroclinic eddies are key to understanding their moist vertical structure.

2.5.1 Dry model

In order to explain the role of surface moisture, we will extend a dry kinematic model for the distribution of mass fluxes within the surface layer of Held and Schneider (1999). We begin with a review of their purely dry model, a model that is based on the assumption that a stratified surface layer with a uniform meridional velocity exists right above the Ekman layer. The momentum balance in the surface layer is used to relate the layer's velocity to the surface potential temperature deviations from its

mean value:

$$v_s(\lambda, \phi, t) = \alpha(\phi)(\theta_s(\lambda, \phi, t) - \overline{\theta_s}(\phi)), \tag{2.13}$$

where v_s is the surface velocity, θ_s is the surface potential temperature and $\overline{\theta_s}(\phi)$ is the zonal and temporal mean of θ_s. This linear formulation is the simplest such formulation guaranteeing that warm air flows poleward and cold air flows equatorward. The factor $\alpha(\phi)$ is a proportionality constant that is positive in the northern hemisphere and negative in the southern hemisphere.

The "surface layer" is defined from the ground up to the highest isentrope $\theta_I(\phi)$ that interacts substantially with the ground. Held and Schneider neglect variations in the surface layer's static stability, attributing it a fixed value $\frac{1}{g}\frac{\Delta p_s}{\Delta \theta_s}$. In our development, we take the quantity $\Delta\theta_s$ to be equal to the surface potential temperature standard deviation, assuming that the lower tropospheric stratification is proportional to the variance of surface temperature. At any point in time, the mass flux on an isentropic layer with potential temperature θ that lies within the surface layer, $\theta_s(\lambda, \phi, t) < \theta < \theta_I(\phi)$ is then

$$\frac{1}{g}\frac{\Delta p_s}{\Delta \theta_s} v_s = \frac{1}{g}\frac{\Delta p_s}{\Delta \theta_s}\alpha(\phi)(\theta_s(\lambda, \phi, t) - \overline{\theta_s}(\phi)).$$

The mass flux vanishes whenever the isentropic layer of interest lies below the ground. In order to determine the zonal-mean mass flux associated with the surface, $\langle \rho v \rangle_s$, they assume they are given the surface potential temperature probability distribution $\Pi(\theta_s, \phi)$. The product $\Pi(\theta_s, \phi)\Delta\theta$ represents the fraction of the time that the surface potential temperature is between

θ_s and $\theta_s + \Delta\theta$. This quantity tells us that a given isentrope $\theta < \theta_I(\phi)$ will occur a fraction $\int_0^\theta \Pi(\theta_s, \phi) d\theta_s$ of the time. Since the velocity of a surface layer isentrope was assumed to be uniform within an atmospheric column and fully determined by the potential temperature at the intersection of the column with the ground through equation (2.13), the zonal and temporal mean mass flux for $\theta < \theta_I(\phi)$ will be given by

$$\langle \rho v \rangle_s = \frac{1}{g} \frac{\Delta p_s}{\Delta \theta_s} \alpha(\phi) \int_0^\theta (\theta_s - \overline{\theta_s}(\phi)) \Pi(\theta_s, \phi) d\theta_s. \tag{2.14a}$$

If the probability distribution was Gaussian, which it is close to in midlatitudes, then (2.14) would also be Gaussian with the same standard deviation as $\Pi(\theta_s, \phi)$ and would take the form:

$$\langle \rho v \rangle_s = \frac{1}{g} \Delta p_s \Delta \theta_s \alpha(\phi) \Pi(\theta_s, \phi). \tag{2.14b}$$

The fast decay of the Gaussian distribution means that values of θ more than a few standard deviations above $\overline{\theta_s}(\phi)$ contribute little to the average mass flux. For the remainder of this section, we assume that the distribution $\Pi(\theta, \phi)$ is normal[3] with mean $\overline{\theta_s}$ and standard deviation $\Delta\theta_s$.

In addition to the surface layer, Held and Schneider specify a *mixed layer* with a mass thickness $\frac{\Delta p_m}{g}$ that has a vertically uniform potential temperature equal to the surface value. The associated mass flux will thus

[3]The tails of the distribution usually differ significantly from normality. Since this theory is not supposed to account for extremes, it is convenient to assume that in our discussion $\Pi(\theta, \phi)$ corresponds to a truncated version of the real distribution from which we have removed the first and last 10 percentiles. Using this truncated distribution we can compute $\overline{\theta_s}$ and $\Delta\theta_s$ as well as setting θ_I to the 100^{th} percentile (which will be the same as the 90^{th} percentile in the full distribution). This is how the $\overline{\theta_s}$ and θ_I values in Figure 2.12 were calculated.

be

$$\langle \rho v \rangle_{\mathrm{m}} = \frac{\Delta p_m}{g} v_s \Pi(\theta, \phi) = \frac{\Delta p_m}{g} \alpha(\phi)(\theta - \overline{\theta_s}) \Pi(\theta, \phi). \tag{2.15}$$

In the expression, the factor $\Pi(\theta, \phi)$ should be understood as representing the fraction of the time the mixed layer will spend at surface potential temperature $\theta_s = \theta$. The net transport associated with ground interactions is obtained by adding the two contributions

$$\begin{aligned} \langle \rho v \rangle &= \langle \rho v \rangle_{\mathrm{m}} + \langle \rho v \rangle_{\mathrm{s}} \\ &\approx \left((\theta - \overline{\theta_s}(\phi)) - \frac{\Delta p_s}{\Delta p_m} \Delta \theta_s(\phi) \right) \frac{\Delta p_m \alpha(\phi)}{g} \Pi(\theta, \phi), \end{aligned} \tag{2.16}$$

This expression corrresponds to an equatorward flow for $\theta < \overline{\theta_s}$ but not necessarily for $\theta \geq \overline{\theta_s}$ since the first term becomes poleward and the second term remains equatorward. The model is summarized as a schematic shown in Figure 2.11.

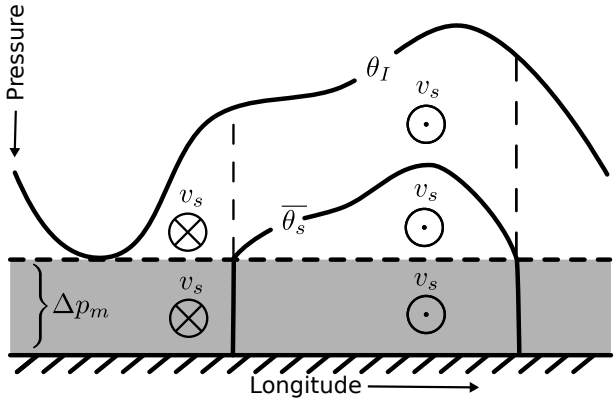

FIGURE 2.11. Diagram for the surface and mixed layer model of section 2.5. The direction of the geostropic velocity v_s is equatorward, $\odot$, in columns where surface θ_s is below $\overline{\theta_s}$. On the other hand, the velocity is poleward, $\otimes$, in columns where surface θ_s is above $\overline{\theta_s}$. The shaded region, corresponding to the mixed layer, is moist.

In Figure 2.12, which shows the joint mass flux distribution at 35°N during DJF, we indicate the key quantities $\overline{\theta_s}$ and θ_I. The joint distribution is

comprised of two main regions. The first region lies along the 80% relative humidity curve and intersects two peaks of opposite sign. These air masses originate from the mixed layer and are thus moist. The second lies along the $\theta = \theta_e$ curve and is mostly dry. It represents equatorward flowing air and corresponds to the surface layer in the simple model. However, it does not peak at $\theta = \overline{\theta_s}$ as in the model but instead remains important at higher levels. This is because the full joint distribution includes mass fluxes occurring in the free troposphere that are adding to the surface layer fluxes.

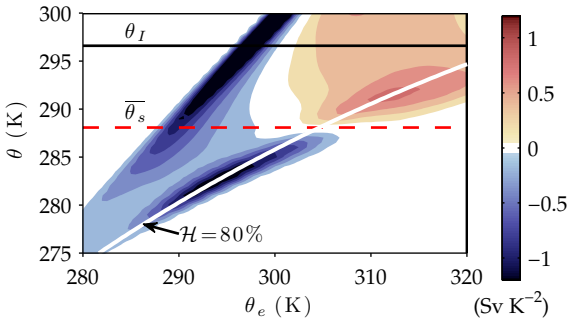

FIGURE 2.12. Lower tropospheric joint distribution for DJF at $\phi = 35°$N. The solid line indicates the arbitrary cutoff θ_I and the red dashed line shows the local average surface potential temperature θ_s. The diagonal curve shows the local surface 80% relative humidity contour, computed by using the average surface pressure and $\overline{\theta_s}$.

2.5.2 Moist model

Of the two regions identified in Figure 2.12, the one that corresponds to the mixed layer is the one which must be extended to include the effects of moisture. Figure 2.12 suggests that it would be appropriate to assume that the mixed layer term has a high relative humidity and that the surface layer term is dry. With 80% relative humidity as in the figure, the two layers occupy very distinct regions in the joint distribution.

If one projects the mass fluxes from the mixed and surface layers, there

will be no cancellations for $\theta < \overline{\theta_s}$ but significant cancellations for $\theta > \overline{\theta_s}$. By using the same ideas as in section 2.3 we can use the joint distribution to decompose the fluxes into directional fluxes to avoid the cancellations. Within the framework of this simplified model, this is done easily by attributing the whole surface layer along with the mixed layer with potential temperature below $\overline{\theta_s}$ to the equatorward directional fluxes while attributing the remainder of the mixed layer to the poleward directional fluxes:

$$\langle \rho v \rangle^{-} = -\left(\max\{\overline{\theta_s}(\phi) - \theta, 0\} + \frac{\Delta p_s}{\Delta p_m} \Delta\theta_s(\phi) \right) \frac{\Delta p_m \alpha(\phi)}{g} \Pi(\theta, \phi), \quad (2.17a)$$

$$\langle \rho v \rangle^{+} = \max\{\theta - \overline{\theta_s}(\phi), 0\} \frac{\Delta p_m \alpha(\phi)}{g} \Pi(\theta, \phi), \quad (2.17b)$$

where we have assumed that we are in the northern hemisphere, so that northward is poleward and southward is equatorward. For $\theta < \overline{\theta_s}$, the poleward flux is zero and the equatorward flux is moist. Physically, this flow is assumed to have been reinjected from within the surface layer into the mixed layer and subsequently moistened. On the other hand, the poleward flow with potential temperatures higher than $\overline{\theta_s}$ is moist with a high relative humidity.

2.5.3 Relation to the interior flow variance

The poleward flux $\langle \rho v \rangle^{+}$ occurs at potential temperature values that depend on the distribution of surface potential temperatures $\Pi(\theta, \phi)$. If one computes the mean potential temperature transported by $\langle \rho v \rangle^{+}$, θ^{+}, in equations (2.17), one finds that it depends fundamentaly on the variance of

the distribution $\Pi(\theta, \phi)$:

$$\theta^+ = \int_0^\infty \theta \langle \rho v \rangle^+ d\theta \Big/ \int_0^\infty \langle \rho v \rangle^+ d\theta = \overline{\theta_s} + \sqrt{\frac{\pi}{2}} \Delta\theta \approx \overline{\theta_s} + 1.25 \Delta\theta_s, \quad (2.18)$$

where we have made explicit use of the Gaussian assumption for $\Pi(\theta, \phi)$. Since it was observed in subsection 2.3.3 that the poleward flows were following slanted moist isentropes, it is expected that moist lower tropospheric air is carried to potential temperatures values similar to their equivalent potential temperature. The vertical extent in θ of the MR will thus be related to lower tropospheric values of θ_e in the poleward flow.

The typical value of θ_e in the poleward flow, θ_e^+, will be related to the typical θ^+ values in the poleward flow by

$$\theta_e^+ \approx \theta^+ e^{\frac{L_{v0}}{c_{pd}} \mathcal{H} \frac{e_s(\theta^+)}{p_0}}, \quad (2.19)$$

where $\mathcal{H}$ is a typical surface relative humidity, shown to be typically on the order of 80%. Because of such a relationship, the vertical structure of the MR will be determined by θ^+, which depends on the zonal variability of θ_s.

A similar result had already been obtained by Juckes (2000) and Frierson (2006). Their theories relate the moist static stability to meridional gradients of surface temperatures and equivalent potential temperatures, respectively. While we do not compute directly the moist static stability, we explain why the vertical extent of the eddy-induced circulation should be determined by moist ascents. Our approach has the advantage of clearly identifying the zonal variability as the generator of vertical stratification but it has the limitation that it describes only the portion of the atmosphere affected by

the circulation.

In Pauluis et al. (2010b) used an approximation to the distribution of eddy fluxes $\overline{v'\theta'_e}$ on isobars to show that the difference between the poleward and equatorward θ_e is proportional to 2.5 times the standard deviation of θ_e. This 2.5 factor arises for a similar reason as the 1.25 factor of equation (2.18) but unlike in this equation, it should apply in the whole midlatitudes turbulent region and not only to the surface flow.

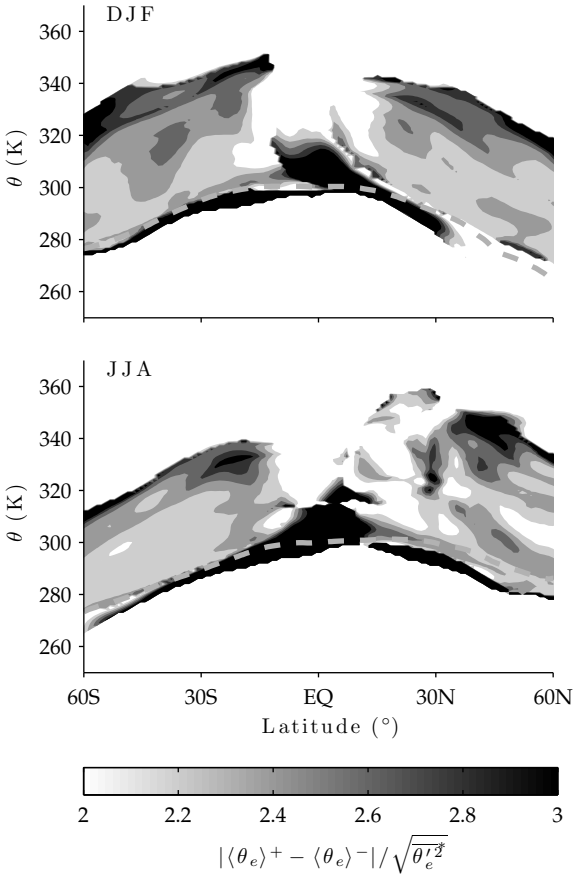

FIGURE 2.13. The ratio of directional θ_e variability $|\langle\theta_e\rangle^+ - \langle\theta_e\rangle^-|$ to the θ_e standard deviation on dry isentropes. The non-dimensional contours are in 0.2 increments.

While in that work, a gaussian distribution of θ_e on isobars was postulated in order to arrive to this result, with the method developed in this chapter we can compute the difference $|\langle\theta_e\rangle^+ - \langle\theta_e\rangle^-|$ without the need for a similar distribution of θ_e on dry isentropes. We can therefore check that this difference is indeed proportional to the standard deviation of θ_e on dry isentropes. To this end, we plot in Figure 2.13 the difference $|\langle\theta_e\rangle^+ - \langle\theta_e\rangle^-|$ divided by the mass-weighted standard deviation of θ_e on dry isentropes, $\overline{\theta'^2_e}^{*1/2}$, where is a deviation of the isentropic mean, $\theta'_e = \theta_e - \overline{\theta_e}^*$. All midlatitudes expect NH JJA are found within 2.0 and 3.0 with the bulk of the

winter hemispheres being found between 2.2 and 2.4. This shows that, as a general rule, the difference between the two directional θ_e profiles is about 2.3 times the standard deviation of θ_e. This confirms that midlatitudes moist dynamic is dominated by large variance flows and that assuming meridional eddy fluxes of heat to be produced by small disturbances, as we did in the derivation of the TEM in subsection 1.2.2, does not appear to be valid.

2.5.4 Low-Level Circulation on Moist Isentropes

Model (2.17) describes fluxes on dry isentropic surfaces for the lower troposphere. It is not a complete model of the circulation because it does not include the mid-to-upper tropospheric flows necessary to close the circulation streamlines. On the other hand, if one assumes that the mid tropospheric circulation is to first order a response to the surface dynamic then we can use our model to compare the strength of the low-level flow between the moist and dry isentropic circulations.

The analyses used in this chapter suggest that, in the mixed layer, the equivalent potential temperatures found in the poleward flow are typically higher than $\theta_I(\phi)$ in midlatitudes. This means that the equatorward branch of the circulation on moist isentropes if computed using this model will exclusively include equatorward fluxes, without cancellations. This indicates that its total mass transport is in large part determined by the sum of the contributions from the surface and mixed layers. These two contributions cannot however be of a very different order. If the mixed layer contribution was much more important than the surface layer contri-

bution, the maximum of the dry isentropic circulation would be attained exactly at the mean surface potential temperature. On the hand, if the surface layer was dominant, the dry isentropic circulation would peak at potential temperatures values typical of the mid troposphere. This leaves no choice but to conclude that the two contributions are of the same order. This conclusion implies that the circulation on moist isentropes intensity must be approximately twice the contribution from the mixed layer, which is the main contribution to the strength of the circulation on dry isentropes. This provides a heuristic argument why the moist isentropic circulation is expected to be roughly twice the dry isentropic circulation in midlatitudes.

2.6 Summary

Using reanalysis data, we have presented a new perspective on the Pauluis et al. mass flux joint distribution that provides a simplified description, on potential temperature surfaces, of meridional equivalent potential temperature fluxes and their associated mass fluxes. Our analysis splits the joint distribution into its northward and southward components and identifies their respective equivalent potential temperature profiles. These profiles describe the moist stratification as experienced by the directional components of the joint distribution and as such allow a precise assessment of the moist ascents within extratropical eddies.

As warm and moist air moves poleward, it follows a dry isentrope until is reaches saturation, after which it follows a slanted saturated isentrope. In the subtropics, the moist stratification associated with the poleward components shows that moist surface air is not able to move along its slanted moist isentrope without sharply transitioning to higher θ values at one point or another of its trajectory, which is a characteristic of fast deep convection. In the extratropics, on the other hand, the poleward branch moist stratification indicates that moist air can move along moist slanted isentropes without having to undergo a similar transition, a phenomenon that we associated with slow slantwise convection. At the opposite, equatorward θ_e profile corresponds to dry isentropes for potential temperatures typical of mid tropospheric air. For potential temperatures typical of surface values, the equatorward θ_e profile is moist with θ_e values corresponding to high surface relative humidity. This is interpreted as an indication that mid tropospheric dry air is moistened after it is reinjected in the planetary boundary layer.

The stark difference between the moisture content of the directional components is associated with strong mid tropospheric mass fluxes in both components, allowing them to cancel each other out on potential temperature surfaces. These opposing mass fluxes that form the Moist Recirculation are observed from the deep subtropics through all of midlatitudes and over a broad range of potential temperatures from surface values to upper tropospheric values. The Moist Recirculation is associated with moist baroclinic eddies and is seen to be responsible for most of the meridional latent heat fluxes as well as being key in connecting the subtropics to the midlatitudes in the winter hemispheres. We noticed that the Moist Recirculation strength was not independent of the moist stratification. Indeed, the Moist Recirculation peaks in the transition region where the atmosphere goes from being predominantly conducive to deep convection to being primarily susceptible to slantwise convection. This suggests that slow convection is more effective at strengthening moist baroclinic eddies, a claim that cannot be entirely supported by this reanalysis study but will be addressed in chapter 3. In that chapter, we use idealized moist life cycles experiments to show a relationship between slantwise convection and enhanced dynamics.

The decomposition into directional fluxes provides a vertical θ_e profile in the poleward flow that seems to determine the moist stratification in midlatitudes. Indeed, while one can investigate the stability of the atmosphere using the θ_e climatology on pressure surfaces, it would not correspond to the effective stability as experienced by any flows. Instead, what we have shown is that poleward flows undergo all of the moist instabilities and that the equatorward flows are essentially stable to moist ascents. The

decomposition presented in this paper thus make it is possible to identify very clearly the regions where moist ascents are important and what type of convection is more prevalent in those regions.

The decomposition into directional components was used to present an approximate circulation on moist isentropes. This approximate circulation is in good qualitative agreement with the exact circulation on moist isentropes but have some weakenesses. In particular, it is biased because the directional θ_e neglects higher θ_e moments in the directional distributions. The approximate circulation has sharper gradients than the circulation on moist isentropes, sharper gradients that are associated with vanishing moist stratification in directional θ_e profiles. Most of the approximate circulation features can be traced back in the directional fluxes and the directional θ_e profiles, which provides a way to understand the moist circulation using quantities that have θ as a vertical coordinate. This way, we were able restore a sense of the vertical in the analysis of the moist circulation.

All these observations show that the moist stratification in the midlatitudes is related to surface values of θ_e in the poleward component. In order to understand what sets this value, we extended the theory by Held and Schneider (1999) describing the low-level flows by introducing moisture to make it match our observations. The theory attributes all of the low-level poleward flow to the boundary layer. By assuming a simple correlation between surface meridional velocities and surface potential temperature anomalies, it was shown that the poleward boundary layer mass fluxes were occurring at potential temperature values depending on the zonal variance of surface θ. Since the boundary layer is usually moist with high

relative humidity, we showed that the mean surface equivalent potential temperature in the poleward flow was related to both the mean and the variance of surface temperature.

This conclusion offers a way to understand the connection between surface moisture values and static stability. Since the poleward flow has a low moist stratification due to deep convection in the subtropics and slantwise-like convection in the extratropics, it means that its poleward θ_e is directly related to the surface θ_e in the poleward flow. Because the equatorward mass fluxes were observed to take place in response to the poleward fluxes, their dry static stability must be related to difference between the poleward component θ_e and surface θ_s. This explains the moist stratification within the poleward component and the dry stratification within equatorward component of eddies using only average surface temperatures and their zonal variance. This extends the theories of Juckes and Frierson by describing the processes causing the midlatitudes' stratifications.

Chapter 3

Idealized Moist Life Cycles

3.1 Context

In chapter 2, the Moist Recirculation was said to represent ascending mass fluxes within midlatitudes eddies, with the underlying assumption that the primary source of turbulence was baroclinic instability. As described in the introduction, it has long been recognized (Eady, 1949; Charney, 1947) that the midlatitudes atmosphere is usually baroclinically unstable. For this reason, baroclinic instabilities develop regularly and grow into weather systems. Baroclinic eddies affect the background atmosphere, bringing it back towards a state of increased baroclinic stability by transporting heat, water vapor and momentum in the meridional direction. Radiative forcing then subsequently acts to restore meridional temperature gradients and return the atmosphere to a baroclinically unstable state. In the study of baroclinicity, works commonly fall in two categories (Pierrehumbert and Swanson, 1995): studies that investigate the cumulative

effect of numerous eddies on the mean atmospheric state and studies that consider a baroclinic event in isolations .

The first strain of work focuses on the effects of baroclinic eddies upon the midlatitudes climatology in long term simulations. In these studies, the evolution of a single eddy is not relevant. Instead, it is the collective impact of those eddies on the atmospheric mean state, through their meridional heat and momentum fluxes, that is of fundamental importance. A specific branch of these studies have been recently concerned about the effect of greenhouse gases on this climatology. Modeling studies of Bengtsson et al. (2006, 2009); O'Gorman and Schneider (2008); Wu et al. (2010), just to mention a few, show important changes in the intensity and geographical distribution of the storms associated with baroclinic eddies.

Recent studies of the dynamical effect by moisture on the extratropical climatology suggest that latent heat release can have great impacts on the characteristics of the meridional circulation. Schneider et al. (2010), using an idealized GCM, showed that the tropical atmosphere was strongly affected by moisture, with the Hadley cell being weakened and its width increased with surface warming. Moreover, their simulations indicate a reduction in the mean Eddy Kinetic Energy (hereafter EKE) in the extratropical atmosphere unlike what had been deduced from life cycle simulations (Gutowski et al., 1992). In the same vein, Frierson (2006, 2008) uses a similar GCM to relate changes in sea surface temperature distribution to changes in midlatitudes stability.

The second strain of work study the growth mechanism of a baroclinic eddy starting from an initially balanced yet baroclinically unstable state. A

large part of these studies are linear in nature, primarily investigating the morphology and growth rate of normal modes (see Simmons and Hoskins, 1977; Lin and Pierrehumbert, 1988, 1993, for example). This approach proves to be useful if one wants to describe the early dynamic of baroclinic eddies.

These linear studies are however unable to account for the turbulent development in the later stages of the eddy evolution. To complement these and allow the investigation of the turbulent stage, it is common (e.g. Thorncroft et al., 1993) to use numerical models of the non-linear evolution equations to study the complete life cycle of a single baroclinic eddy. The role of moisture in these studies has been a relatively recent development. The moist linear growth and normal modes has been studied for saturated initial conditions (Fantini, 1999; Whitaker and Davis, 1994) or for zero moist potential vorticity (Fantini, 2004). Both are special cases that are usually far from typical atmospheric conditions. More realistic moist life cycles along with their non-linear evolution was studied by Gutowski et al. (1992); Moore and Montgomery (2005). Moist frontogenesis and the concept of the diabatic rossby vortex was introduced at about the same time (Parker and Thorpe, 1995; Thorpe and Emanuel, 1985; Montgomery and Farrell, 1991; Moore and Montgomery, 2005) and shown to be an important mechanism in the evolution of moist baroclinc eddies. These theories focus on the role of convective potential vorticity anomalies on dynamics of baroclinic instabilities. This effect is fundamental to understand the development of long waves in the presence of moisture.

To connect the two approaches, it is necessary to use a technique that is

able to resolve transient eddy features without the need to explicitly track individual eddies. To this end, in chapter 2, we have investigated the relevance of using isentropic averages, based of the postulate that an average along isentropic surfaces closely captures the Lagrangian trajectories of baroclinic eddies.

The assumption that potential temperature is a good Lagrangian marker is hampered by two mechanisms. First, if the baroclinic eddies time-scale is too long with respect to the radiative cooling time-scale, then the potential temperature could change appreciably over the duration of eddies life cycles. This would greatly reduce the potential temperature usefulness in resolving eddy transports. Since the radiative cooling is of the order of 1K per day this effect is generally negligible for the explosive evolution of an eddy life cycle that last 5 to 7 days. In Czaja and Marshall (2006); Pauluis et al. (2008, 2010a), the effect of moisture has been addressed by the replacement of potential temperature by the equivalent potential temperature. This approach relies on the idea that latent heat release effects are fundamental to the dynamics of midlatitudes eddies.

The theory developed in this thesis assumes that meridional heat fluxes are driven by zonally asymmetric features, including moist baroclinic eddies but also stationary waves, tropical cyclones, etc. Because it was postulated in chapter 2 that moist baroclinic eddies were the primary source of zonal asymmetry, in this chapter we are interested in understanding how their nonlinear evolution contributes to meridional transports. This nonlinear evolution is usually complex, with air masses being displaced poleward and upward in non-trivial patterns (Stone et al., 1999; Polvani

and Esler, 2007).

In order to achieve this goal, we run life cycle experiments using an idealized atmospheric GCM for which we specify initial conditions with a surface moist layer of varying depth (up to 5 km) and varying relative humidity (from dry to 80%). We are able to describe the transition from a completely dry life cycle to a moist cycle and observe how the input of moisture influences the life cycle dynamics. Based on these observations to explain changes in the net meridional transport of mass and heat with the help of the mass flux joint distribution and the techniques developed in chapter 2. These techniques can be used to quantify the net meridional reorganization of air masses produced by adiabatic moist life cycles. This allows to identify which feature of the meridional heat transports attributed to moist baroclinic eddies can be traced back to reanalysis data.

In section 3.2 we present the model and the procedure used for the initialization of the balanced baroclinic flow. We follow closely the setup of Polvani and Esler (2007) and describe our method to include simple moisture effects. Next, in section 3.3, we compare a moist control run to a dry control run using PV dynamics on a fixed isentropic surface. In section 3.4, we study the isentropic circulations in moist and dry coordinates, using the language developed in chapter 2. We further investigate the structure of the moist recirculation along with the vertical profiles of θ_e and compared them with the EKE on isentropic surfaces.

3.2 Experimental Setting

3.2.1 Equations

We use the hyper-viscous primitive equations on the sphere in pure σ coordinates with idealized moisture. The horizontal velocity $\mathbf{u} = (u, v)$, the moist enthalpy h_m described in equation (1.52), the specific water content q_T and surface pressure p_s satisfy

$$\frac{d\mathbf{u}}{dt} + 2\Omega \sin\phi \mathbf{k} \times \mathbf{u} + \nabla_{\mathrm{h}}\Phi + \frac{R_d T_v}{p_s}\nabla_{\mathrm{h}} p_s = \nu \nabla_{\mathrm{h}}^6 \mathbf{u}, \tag{3.1a}$$

$$\frac{dh_m}{dt} - \frac{R_d T_v}{p_s \sigma}\omega = \nu \nabla_{\mathrm{h}}^6 h_m, \tag{3.1b}$$

$$\frac{dq_T}{dt} = \nu \nabla_{\mathrm{h}}^6 q_T, \tag{3.1c}$$

$$\partial_t p_s + \int_{\sigma_T}^1 \nabla_{\mathrm{h}} \cdot (p_s \mathbf{u}) d\sigma' = 0, \tag{3.1d}$$

along with the diagnostics for the hydrostatic geopotential Φ and vertical velocity in pressure coordinates, ω,

$$\Phi = R_d \int_{\sigma}^1 T_v \frac{d\sigma'}{\sigma'}, \tag{3.1e}$$

$$\omega = \sigma \mathbf{u} \cdot \nabla p_s - \int_{\sigma_T}^{\sigma} \nabla_{\mathrm{h}} \cdot (p_s \mathbf{u}) d\sigma'. \tag{3.1f}$$

The material derivative can then be formulated as

$$\frac{d(\cdot)}{dt} = \partial_t(\cdot) + \mathbf{u} \cdot \nabla_{\mathrm{h}}(\cdot) + \dot{\sigma}\partial_\sigma(\cdot),$$

where $\dot{\sigma}$, the vertical velocity in σ coordinates, can be found using (3.1d) and (3.1f) as well as use the fact that p_s is a constant function of σ:

$$p_s\dot{\sigma} = \omega - \sigma\frac{dp_s}{dt} = \int_\sigma^1 \nabla_\mathrm{h} \cdot (p_s\mathbf{u})d\sigma'. \tag{3.2}$$

The horizontal gradient operator ∇_h is taken at constant σ. We use a hyper-viscosity ν that is discussed in the model's description in subsection 3.2.2. All other symbols found in equations (3.1) are listed in Table 3.1.

TABLE 3.1. Physical parameters

Parameter	Value	Units
g	9.806	cm/s^2
a	6.371×10^6	m
Ω	7.292×10^{-5}	1/s
R_d	287	J/kg/K
κ	2/7	
c_{pd}	R_d/κ	J/kg/K
p_0	101325	Pa
R_v	461.5	J/kg/K
c_{pv}	$4R_v$	J/kg/K
L_{v0}	2.5e6	J
c_l	4190	J/kg/K
$e_{s\mathrm{ref}}$	610.7	Pa
T_ref	273.16	K

Without moisture, these equations are as described by Durran (1999). When moisture is present ($q_T > 0$) the virtual temperature, T_v, is a function of the specific water vapor, q_v, and the temperature, T,

$$T_v = (1 + \epsilon q_v)T. \tag{3.3}$$

The factor $\epsilon = R_v/R_d - 1$ is constant for an ideal mixture of water vapor and dry air. This formulation of the virtual temperature does not include the effect of condensed liquid water on the moist air's density, thus preventing the appearance of instabilities resulting from the large-scale mixing of saturated and unsaturated air. For a saturated parcel, this brings inconsistencies in its energy budget but because we will only study flows that precipitate, this will not lead to important biases. The temperature and the specific water vapor (T, q_v) needed to compute the virtual temperature are functions of the moist enthalpy h_m and the specific water content q_T, functions that have to be specified to close equations (3.1).

To this end, we use an idealized representation of moisture by assuming that liquid water never freezes. It allows the use of the Clausius-Clapeyron equation for ideal gases (1.35) to find the saturation vapor pressure, $e_s(T)$.

$$e_s(T) = e_{s\text{ref}} \exp\left(\frac{1}{R_v}\left(\frac{L_v(T_0)}{T_0} - \frac{L_v(T)}{T}\right) - \frac{c_l - c_{pv}}{R_v}\ln\left(\frac{T}{T_0}\right)\right),$$

If we further simplify our description by assuming that water vapor is never oversaturated, the saturation vapor pressure is sufficient to construct functional forms for q_v and h_m. Using $p = \sigma p_s$, these can be formulated as,

$$q_v = \min\left\{q_T, (1 - q_T)\frac{q_v^*(p,T)}{1 - q_v^*(p,T)}\right\}, \tag{3.4a}$$

$$h_m = c_{pd}\left(1 + \delta_l q_T\right)T + L_v(T)q_v, \tag{3.4b}$$

where $\delta_l = c_l/c_{pd} - 1$ is also a constant for and ideal mixture of gases and $L_v(T)$ is the latent heat of vaporization for an ideal mixture of ideal gases.

The specific water vapor $q_v^*(p,T)$ is the maximum specific water vapor that can be attained through an isothermal and isobaric process:

$$q_v^*(p,T) = \frac{R_d e_s(T)}{R_v p - \epsilon R_d e_s(T)}.$$

The equations of motions (3.1) prognose q_T and h_m, which can be used to invert system (3.4) for T and q_v for a fixed pressure p.

The thermodynamic equation (3.1b) along with the conservation of the total water content (3.1c) implies, from the first law of thermodynamics, that the equivalent potential temperature θ_e is conserved for adiabatic motions. For non-adiabatic motions caused by precipitation occurring at saturation, θ_e will be virtually unchanged. It will be slightly affected by the process because as condensed water is removed from the system it removes its specific heat simultaneously, which acts to reduce the parcel total specific heat content. In the model presented next, this condition will be satisfied, implying that for our model θ_e can be assumed to be unchanged by precipitation.

3.2.2 Model

We use an experimental setting that was designed to offer a natural moist extension to the dynamic studied by Polvani and Esler (2007), which was itself an extension of Polvani et al. (2004). To this end, we appended a full moisture representation to the GFDL Memphis Spectral Core by replacing the temperature by the moist enthalpy in the temperature equation and by specifying the total water content q_T as a tracer. The latter specification

serves to include equation (3.1c) in the dynamical core. The substitution of the temperature for the moist enthalpy is required in order for the dynamical core to have its thermodynamics evolved according to equation (3.1b). The use of a third-order hyper-viscosity creates a diffusive scale while preserving as much as possible the adiabatic nature of the flow at large-scales. The hyper-viscosity coefficient ν was taken to be resolution dependent and set to be damping the largest spherical wave-number on a 4 hours time-scale. All the simulations performed in this chapter were performed with zonal wave number 6 symmetry.

As it can be seen from equations (3.1), the temperature T is only required to compute the virtual temperature T_v and can thus be treated as a diagnostic variable. Indeed, at the end of each time-step, one can invert equations (3.4) at each grid point using a Newton-Raphson method. The convergence is quick and does not carry much overhead as it is performed point-wise. Surface heat fluxes — sensible and latent — are set to zero and no radiation scheme is used. We thus obtain idealized experiments where most characteristics can be understood by a joint isentropic analysis without having to account for diabatic effects, except for precipitation and hyperdiffusion.

Precipitation can be added to equation (3.1c) by removing liquid water at the end of each time-step, whenever water vapor condensates. By implementing it in this way, we make sure that specific liquid water never attains negative values. This semi-implicit precipitation removes q_T at the end of each time-step at a rate specified by a parametrized precipitation time scale τ_p. The precipitation time-scale was taken to be $\tau_p = 300$s to correspond to

twice the time-step used to run simulations at the T170 resolution.

Because changes in q_T imply changes in the moist enthalpy h_m, one must specify the thermodynamic path taken by a precipitating air parcel. Here, we assume that the rain removes water through an isothermal and isobaric process. At the end of a time-step Δt, q_T and h_m are modified as

$$q_T' = q_T - \min\left\{\frac{\Delta t}{\tau_p}, 1\right\} \max\left\{q_T - q_v^*(p,T), 0\right\}, \tag{3.5a}$$

$$h_m' = h_m(p, T, q_T'). \tag{3.5b}$$

This model resembles the model of Frierson et al. (2006), with the exception that it can be run with large scale condensation that does not precipitate by letting $\tau_p \to \infty$. It is also simpler in the sense that re-evaporation is not allowed and, thus, when water is removed from the system, it disappears altogether from the simulation.

We use a consistent refinement (Lindzen and Fox-Rabinovitz, 1989; Polvani and Esler, 2007) of the vertical and horizontal dimensions. This means that we specify the aspect ratio for typical (dry) vertical wave speeds to typical (dry) horizontal wave speed that we would like to resolve in order to maximize the problem's Courant number. This is accomplished by keeping the same aspect ratio as in Polvani and Esler (2007), namely T170 with 120 vertical levels. Since this study has a tropospheric focus, we use linearly-spaced σ levels instead of the log-spaced levels use in their study.

In order to retain a simple model, we use implicit hydrostatic convection driven by large-scale condensation. It was observed by Gutowski et al. (1992); Moore and Montgomery (2005) that large-scale thermodynamical

adjustments were sufficient to capture the dynamics of their simulated moist life cycles. In particular, Gutowski et al. (1992) showed that by turning off the moist convective parametrization, their results were virtually unchanged. This gives us confidence that by using hydrostatic convection we are not overly biasing our results.

An hydrostatic flow being able to communicate disturbances instantaneously in the vertical brings in parabolicity in an otherwise hyperbolic, finite propagation speed, system. This mixed mathematical behavior can be understood in clear physical terms. The hydrostatic primitive equations have the same conservations laws as the non-hydrostatic equations except that its energy does not include contributions from vertical velocities. Instead, vertical velocities are diagnosed from the divergence of horizontal velocities, divergences that are not constrained by the equations and, hence, can develop a δ-function type blow-up. This leads to extremal vertical velocities that are inversely proportional to the horizontal grid-spacing Δx. The vertical grid spacing being refined proportionally to Δx in this study, the time taken for an air parcel to propagate vertically across a grid cell with the extremal vertical velocities will be proportional to Δx^2, as discussed in Pauluis and Garner (2006). This phenomenon is similar to that of a parabolic equation, highlighting the diffusive nature of grid-scale convection. In convergence analysis for test runs of our model, we observed this phenomenon, with vertical velocities increasing faster than Δx^{-1} when the CFL condition, $\Delta t \propto \Delta x$ for hyperbolic systems is used instead of $\Delta t \propto \Delta x^2$, the condition that is associated with the instantaneous propagation of disturbances by the hydrostatic equation.

Therefore, as long as the vertical kinetic energy remains comparatively much smaller than the total hydrostatic primitive equations kinetic energy *and* time is refined using the CFL condition for parabolic systems, the modeled solution should be a consistent approximation to the non-hydrostatic equations. This justifies the validity and the incurred computational costs of allowing grid scale convection but does not address the fundamental reason why, for our purposes, it constitutes a more sensible choice than any other convective adjustment schemes.

Common parametrizations of deep convection (see Stevens, 2005, for an overview) rely on adjustments that relax atmospheric columns to a convectively stable profile while conserving energy, which can be viewed as non-local re-indexing scheme. Such an adjustment is intrinsically diabatic, which goes contrary to our goal of obtaining life cycles that contain as little thermodynamical biases as possible. If we were to settle with a parametrization that drives diabatic vertical propagation of entropy, we would undoubtedly skew the interpretations our of analysis method. Thus, albeit the use of grid-point convection in a primitive model is at best an ad-hoc representation of convection, it allows us to more accurately assess the parcels trajectories.

3.2.3 Initialization

The initialization follows closely Polvani and Esler (2007) for which we offer a review here. The flow is specified by a zonal velocity profile, u_1,

TABLE 3.2. Moist layer depth parameters (km)

z_l	z_h	$\bar{z} = (z_h + z_l)/2$
0.0	1.0	0.50
1.0	2.0	1.50
2.0	3.0	2.50
3.0	4.5	3.75
4.0	6.0	5.00

confined to the free troposphere. We use the formulation

$$u_1(\phi, z) = U_0 G(\phi) \left[(z/z_T) e^{-\left[(z/z_T)^2 - 1\right]/2} \right], \tag{3.6}$$

where the log-pressure coordinate $z = h_{\text{ref}} \log(p_0/p)$ is equivalent to a pressure coordinate. The zonal velocity is going to be maximum at $z = z_T$ and because its meridional variations are specified as in Simmons and Hoskins (1977),

$$G(\phi) = \begin{cases} \left[\sin\left(\pi \sin^2 \phi\right)\right]^3, & \phi > 0, \\ 0, & \phi \leq 0, \end{cases} \tag{3.7}$$

it peaks $\phi = 45°\text{N}$ while being sufficiently smooth at the equator. The absence of surface wind shear in the velocity profile will result in life cycles of the LC1 type with a dominant anti-cyclonic perturbation. Using this zonal velocity profile, one can compute the meridional temperature profile necessary to balance this flow. The procedure is described in the appendix and results in a slight modification of the technique described in Polvani and Esler (2007).

The modification comes from the introduction of moisture, specified as

a simple relative humidity layer represented by a smoothed step function:

$$\mathcal{H}_{\text{ref}}(z) = \frac{\mathcal{H}_{\text{max}}}{2}\left(1 + \tanh\left(\beta\frac{(z_{\text{h}} + z_{\text{l}})/2 - z}{z_{\text{h}} - z_{\text{l}}}\right)\right), \tag{3.8}$$

which is a function that is essentially equal to $\mathcal{H}_{\text{max}}$ below z_l and 0% above z_h. The parameter β serves to control the width of the transition and was chosen to be equal to 8 in this study. This parameter was set to this value to offer a sharp transition that was well resolved by lower resolution simulations. We will consider variations in $\mathcal{H}_{\text{max}}$ from 0% to 80% and variations in z_{l} and z_{h} as shown from Table 3.2. Changes in the moist layer depth will be always discussed in terms of $\bar{z} = (z_{\text{h}} + z_{\text{l}})/2$, which is the level where the relative humidity is $\mathcal{H}_{\text{max}}/2$. The initial conditions for $\mathcal{H}_{\text{max}} = 60\%$ and $\bar{z} = 1.5$ km can be found in Figure 3.1. In these initial conditions, the high equatorial θ_e surface values are a result of the introduction of the moist layer. All the other parameters used in this study are to be found in Table 3.3.

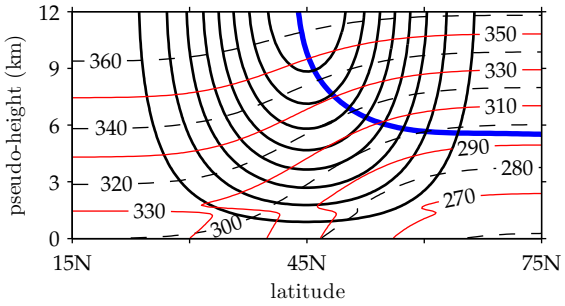

FIGURE 3.1. Initial conditions for $\mathcal{H}_{\text{max}} = 60\%$ and $\bar{z}$=1.5 km moist layer depth. The zonal velocity profile u_1 is shown as black concentric contours and the potential temperature θ_l is shown as black curves. The red contours indicate curves of constant θ_e. The thick blue curve shows the 2 PVU contour.

TABLE 3.3. Simulations parameters for chapter 3

Parameter	Value	Units	Parameter	Value	Units
U_0	45	m/s	$\hat{T}$	1	K
z_T	13	km	$\hat{\phi}$	$\pi/4$	radians
U_s	45	m/s	m	6	
ϕ_s	35	degrees	β	8	
Δ_s	20	degrees	h_{ref}	7.5	km
z_s	10	degrees	ν	4	hours
T_0	300	K	τ_{sim}	20	days
τ_p	300	s	Γ	6.5	K/km
α	10		σ_T	0.02	

3.3 Moist Life Cycles

We begin with a detailed comparative study of a chosen moist control run with its corresponding dry run. Both runs have the same reference temperature profile and the same zonal wind profile but the moist control run has a moist layer depth $\bar{z}$ of 1.5 km and a relative humidity of 60%. We first compare the development of the long wave by the mean of its potential vorticity dynamics. We plot in Figure 3.2 the potential vorticity for a time-series of the two runs on the dry isentrope $\theta_l = 310$K. The potential vorticity is defined as

$$\mathrm{PV} = -\frac{\zeta + f}{\rho_{\theta_l}}, \tag{3.9}$$

where ζ is the horizontal vorticty, $f = 2\Omega \sin\phi$ is the Coriolis parameter, θ_l is the potential temperature[1] and $\rho_{\theta_l} = g^{-1}\partial_{\theta_l} p$ is the isentropic layer thickness. In the dry run (right panels), it is expected that PV be conserved on isentropic surface by the dynamics. In the moist run, on the other hand, diabatic heating resulting from condensation and precipitation will result in vortex stretching that modifies the PV dynamics. The chosen dry isentrope, $\theta_l = 310$K, lies at all times above the ground and crosses the PV $= 2$ PVU curve at around 40°N. By comparing the evolution of the two runs, this time-series reveals the broad moist characteristics that modifies the circulation implied by the adjustment. Because the two runs have different growth rates, the side-by-side comparison is only relevant

[1] We use the liquid water potential temperature of equation (1.48) because our finite precipitation time-scale permits liquid water to remain in our model. While weuse the symbol θ_l to be precise, we make use of the correspondence between θ and θ_l expressed in equation (1.50) to call both of them "potential temperatures" even if within our data they can be different.

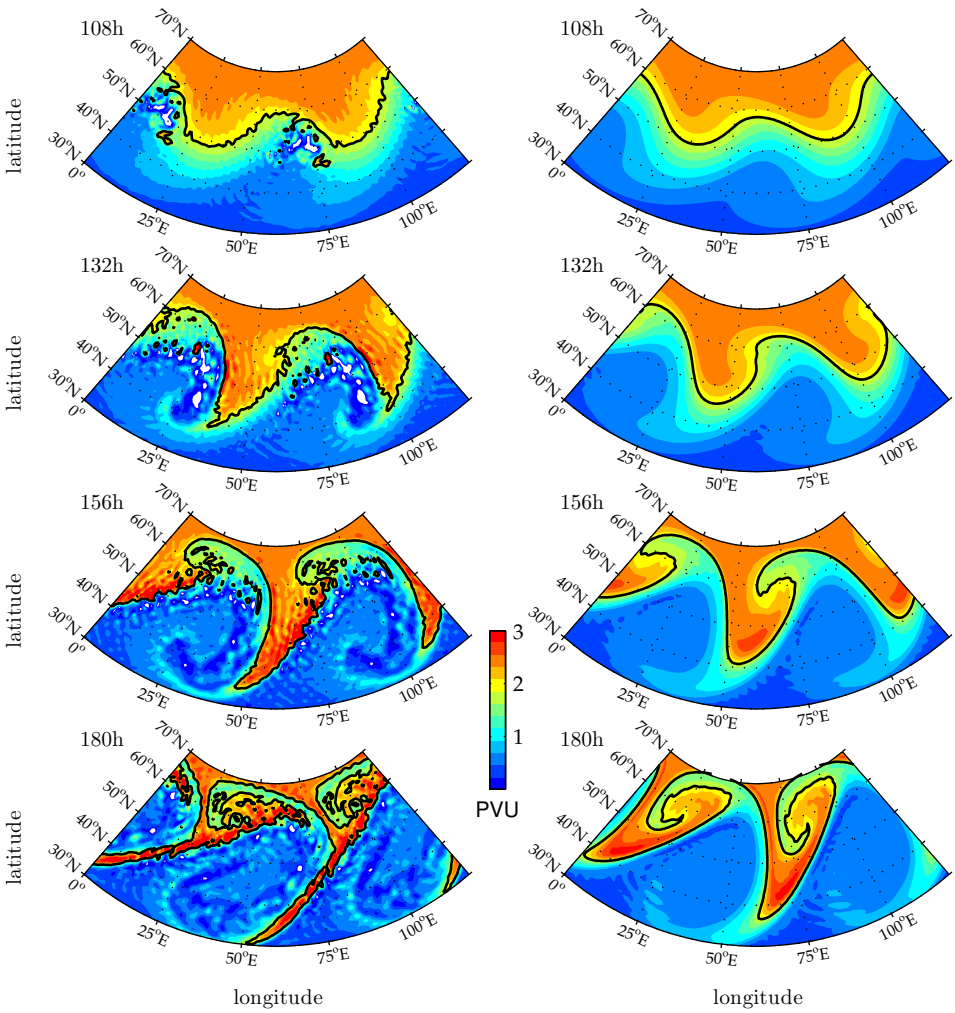

FIGURE 3.2. Dry PV on $\theta_l = 310$K for $\mathcal{H}_{\max} = 60\%$, $\bar{z}$=1.5 km on the left and dry on the right. The thick black line shows the 2 PVU contour.

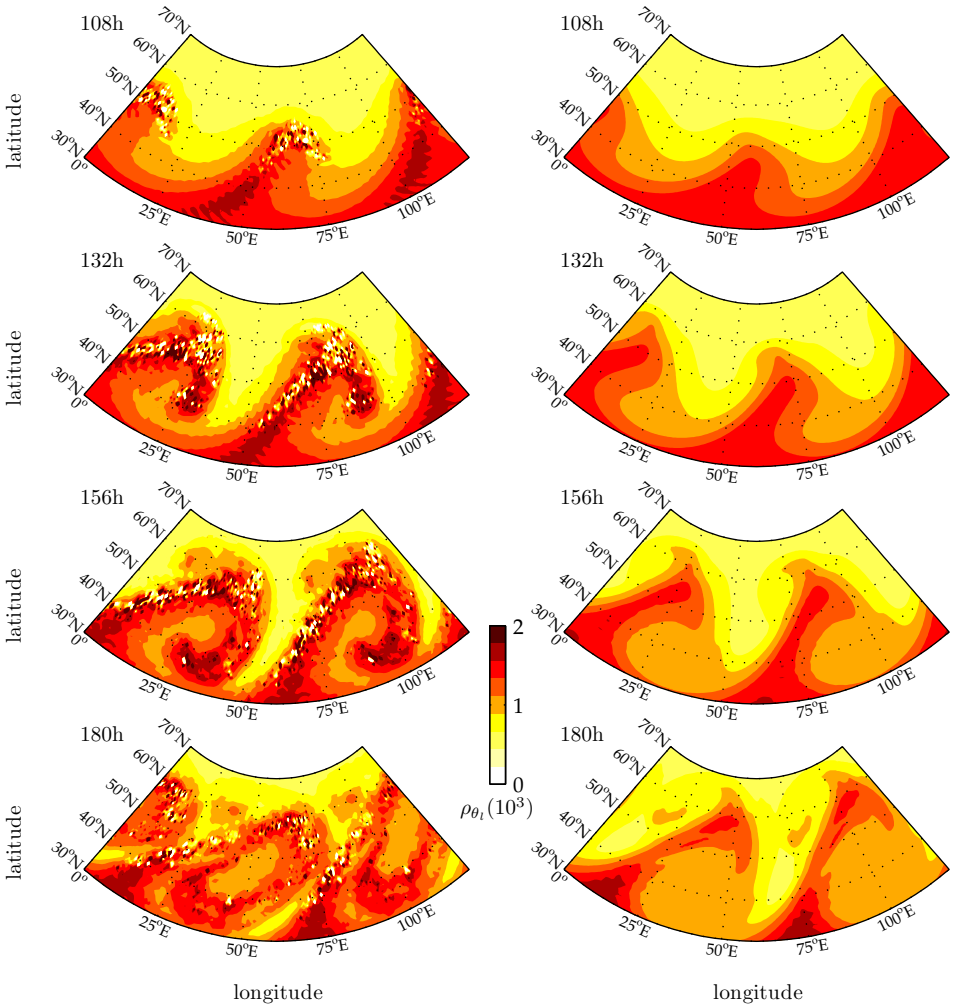

FIGURE 3.3. $\rho_{\theta_l} = g^{-1}\partial_{\theta_l} p$ in Pa K^{-1} on $\theta_l = 310$K for the simulation with $\mathcal{H}_{\max} = 60\%$, $\bar{z}$=1.5 km on the left and the dry simulation on the right.

if one compares the two runs for several time snapshots. This way it is possible to observe differences in evolution without having to worry about which phase of the life cycle each run is at.

To facilitate the understanding of the various observed features, we plot for the same two runs the $\theta_l = 310$K isentropic layer thickness $\rho_{\theta_l} = g^{-1}\partial_{\theta_l} p$ in Figure 3.3. The layer thickness is a key component of PV and for the Rossby numbers found in our simulations, it is the main determinant of PV anomalies. To further correlate the vortex stretching with moist effects, we plot in Figure 3.4 the equivalent potential temperature interpolated on the $\theta_l = 310$K isentropic layer. Because $\theta_e = \theta_l$ when no moisture is present, only the moist control run is shown. Including precipitation causes moisture to be removed from saturated grid cells at the precipitative time scale and as a result $\theta_e > \theta_l$ occurs only in unsaturated regions or in convective regions.

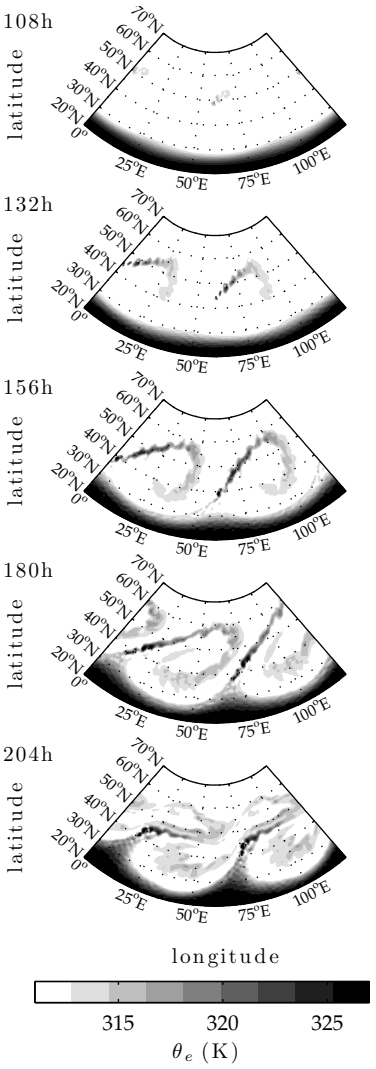

FIGURE 3.4. θ_e on $\theta = 310$K for the $\mathcal{H}_{\max} = 60\%$, $\bar{z}$=1.5 km run. The filled contours are in 3K intervals with the white contour being less than or equal to 311K.

The first snapshot, at 108h, exhibits a deformed PV = 2 PVU contour with a very similar shape in both runs. The overall shape is thus typical of an early deformation for a LC1 growth meaning that on the large scale the moist run appears to have evolved primarily as a long wave. On smaller scales, differences are

noticeable, with the moist run exhibiting a large patch of anomalous low PV air at 75°E and 50°N that is only several degrees in size. This patch is related to a corresponding isentropic layer thickness disturbance in Figure 3.3 which, apart from some bubbles of vanishing or negative thickness, created large thicknesses as compared to the dry run. This suggests that moist air from the boundary layer with $\theta_e \approx 310$K is convecting and settling onto the dry isentropic layer. The fact that the interpolated θ_e in this region (see Figure 3.4) is only slightly higher than 310K reinforces the claim that the moist convection was initiated by moist air with an a equivalent potential temperature comparable to 310K that was initially located near the surface. This means that the low PV anomaly patch has been created by the vortex stretching caused by the injection of moist air in the 310K isentrope.

These low PV anomalies can be tracked in the subsequent snapshot at 132h as it evolves clockwise around the anticyclonic region, a motion that essentially brings low PV equatorward. This time it is clear from Figure 3.4 that these low PV anomalies are associated with a thick isentropic layer at 80°E and 40°N. In Figure 3.4 these are seen to be in a mostly dry region, which confirms the interpretation that they corresponds to air that have been deposited by convection. In the same figure, a band of $\theta_e \approx 320$K moist air that extends to the southwest of 75°E and 50°N. It can be seen to correspond in Figure 3.3 to a region with many bubbles of low thickness. At this stage, the moist life cycle is already quite different from the dry life cycle with a sharp tongue in the 2PVU contour at 40°E and 40°N. The dry run does not exhibit such a sharp feature. The front strengthening is related to the low PV patch's clockwise motion that enhances the anticyclonic

region.

At 156h, the large scale latent heat release has modified the moist run so much that the whole domain has been affected. The anticyclonic region is now composed of an interior with uniform PV surrounded by a fringe of low PV. This low PV was identified with high layer thickness in Figure 3.3 in the previous snapshots. This association still holds at around 90°E and 35°N but is not that strict in the low PV band that extends along the 105°E meridian, especially at latitudes north of 50°N. Unlike in earlier times, important PV dipole anomalies have been created on the front that goes from 50°E and 35°N to 80°E and 60°N, with positive anomalies on the west and negative on the right. With the help of Figure 3.3, one can observe that positive PV anomalies are related to small layer thicknesses and negative PV anomalies, with large thicknesses. This region is populated with bubbles of large θ_e in Figure 3.4, which indicates that local convective adjustment are at play.

In the final snapshot, at 180h, the moist wave continues to generate and enhance the aforementioned features. One novelty in this frame is the maturation of the high latitude stratospheric cyclone centered at 40°E, 60°N in the moist run and at 25°E, 60°N in the dry run. The moist run's cyclone have a wider meridional extent than the dry run's. The moist run thicknesses in Figure 3.3 are described by a noisy field with a sizable patch of large thicknesses at 40°N and 35°E. The same is not true for the dry run where it instead appears that a patch of isentropic layer thickness at 50°E and 60°N is about to be detached from the anticyclonic region. In the meantime, the equivalent potential temperature in Figure 3.4 has curled

around the anticyclonic region and some $\theta_e \approx 315$K air seems to have made it back to low latitudes. We have included an extra frame at 204h for the θ_e distribution on the dry isentrope which shows moist air that travels mostly zonally. This indicates that beyond 180h, the meridional transport of moisture is greatly reduced and the moist run is thus expected to complete its life cycle without substantial large scale latent heat release.

Our description of PV anomalies matches the evolution of a wave that is strongly affected by PV dipoles created by diabatic heating resulting from condensation and precipitation. In the previous summary, we indicated that a pile up of dry air on the $\theta_l = 310$K was a result of moist air with $\theta_e \approx 310$K undergoing moist convection and settling on our isentropic layer of interest. Since this effect happens mostly in the northeastern part of the anticyclonic region, it effectively displaces the region's eastern extent even more to the east. In a concurrent effect, in the 156h and 180h frames, the front was associated with high θ_e and strong dipoles of PV anomalies associated with dipoles of isentropic layer thicknesses. Because of its high θ_e, the frontal moist air is made of convecting air that deplete the isentropic layer at the west of the front while adding to the layer thickness at the east of the front. This specific PV dipole structure on the front has the effect of displacing the front eastward. Because frontal convective effects occur mostly between 40°N and 60°N, it displaces the northern part of the long wave more than the southern part.

This mechanism explains the increased eastward displacements in the long wave northern part and therefore provide an explanation for the long wave breaking earlier in its development. Because the frontal PV dipole

anomalies are not related to a net change in the isentropic layer mass, they do not affect the net meridional transport of heat on the isentropic layer. On the other hand, the negative PV anomalies created by moist convection at high latitudes are due to net addition to the isentropic layer mass. Since these are subsequently brought equatorward, it acts to reduce the net meridional transport on an isentropic layer. This results in a weakened poleward isentropic mass transport and a weakened poleward dry entropy flux as moisture is increased in the boundary layer. As we will see next, the weakening of the isentropic circulation is largely compensated by an increase in poleward latent heat fluxes which are associated with a strengthening of moist circulation.

3.4 Isentropic Circulations

These changes in meridional transport of mass and entropy are expected to depend on the moist layer depth and moisture content. By its action on the evolution of long waves, latent heat release changes the structure of the meridional transports. The theory of chapter 2 can be used to address these changes on the transport induced by the life cycle.

To understand the circulation on dry isentropes induced by the life cycles, it is convenient to consider the equation for the conservation of the isentropic layer thickness ρ_{θ_l}, an equation that is closely related to the continuity equation,

$$\partial_t \rho_{\theta_l} + \nabla \cdot (\rho_{\theta_l} \mathbf{u}) + \partial_{\theta_l} (\rho_{\theta_l} \dot{\theta_l}) = 0, \tag{3.10}$$

where $\dot{\theta_l}$ is the diabatic heating and $\rho_{\theta_l}\dot{\theta_l}$ can be understood as the mass flux across the isentrope. If one takes a zonal mean and integrates in time equation (3.10) on a surface of constant θ_l, one obtains an equation for the zonal mean isentropic layer thickness at time t, $\langle \rho_{\theta_l} \rangle_t$:

$$\langle \rho_{\theta_l} \rangle_t - \langle \rho_{\theta_l} \rangle_0 + \frac{1}{a \cos\phi} \partial_\phi \left(\cos\phi \int_0^t \langle \rho_{\theta_l} v \rangle_t dt \right) + \ldots \\ \partial_{\theta_l} \left(\int_0^t \langle \rho_{\theta_l} \dot{\theta_l} \rangle_t dt \right) = 0. \tag{3.11}$$

Equation (3.11) relates the reorganization of air masses $\langle \rho_{\theta_l} \rangle_t - \langle \rho_{\theta_l} \rangle_0$, the cumulative meridional mass flux $\int_0^t \langle \rho_{\theta_l} v \rangle_t dt$ and the cumulative diabatic mass flux $\int_0^t \langle \rho_{\theta_l} \dot{\theta_l} \rangle_t dt$. In a moist or radiatively forced life cycle, this equation can be used to deduce the diabatic heating rate $\langle \rho_{\theta_l} \dot{\theta_l} \rangle_t$ usingthe

other two quantities which are usually easier to compute. In a purely dry life cycle, there is no diabatic mass flux and the reorganization of air masses in the (ϕ, θ_l) plane can be directly inferred by the cumulative meridional mass flux. The cumulative meridional mass flux can it turn be related to a cumulative dry isentropic streamfunction $\tilde{\Psi}_{\theta_l}$ through

$$\partial_{\theta_l} \tilde{\Psi}_{\theta_l} = \int_0^t \langle \rho_{\theta_l} v \rangle_t dt. \tag{3.12}$$

The cumulative dry isentropic streamfunction (3.12) can also be cast in a more familiar formulation of the streamfunction:

$$\tilde{\Psi}_{\theta_l}(\phi, \theta_l', t) = a \cos\phi \int_0^t \int_0^{2\pi} \int_0^{p_s} v H(\theta_l' - \theta_l) \frac{dp}{g} d\lambda dt. \tag{3.13}$$

The meridional velocity, v, is given as a model output and the liquid water entropy θ_l is computed from equation (1.48) using p, the model output temperature T and specific water content q_T. The phase space θ_l' represents the projection onto an isentropic grid generated by equation (3.13). This expression differs from the formulation of the streamfunction (2.2) in the time integral. Previously, the streamfunction was created with a temporal mean but here the time integral is not fixed and we have not divided by the time. The cumulative streamfunction is therefore a measure of how much *mass* has been transported by the life cycle.

3.4.1 Control Run

3.4.1.1 Dry Isentropic Analysis

The cumulative streamfunction[2] (3.13) is plotted in Figure 3.5 for three times. A thick black line was added to indicate the $\theta_l = 310$K isentrope for which the dynamic was described in Figure 3.2, Figure 3.3 and Figure 3.4. The moist run exhibits deformations in its poleward branch as well as changes in its magnitude. At 144h, its circulation has one more contour than the dry run but later, at 168h, they both have the same number of contours and finally, at 192h, the dry run's circulation has more contours than the moist run.

At 144h, the moist run circulation second contour first crosses the $\theta_l = 310$K isentrope at low latitudes, indicating that early times cross isentropic fluxes favor the upper tropospheric circulation. At later times, on the same isentrope, the moist run circulation becomes more important at higher latitudes. At 192h, this is illustrated by the fifth contour crossing the isentrope at 50°N. The vertical derivative of the circulation being related to meridional mass fluxes, the fact that the moist run circulation is flatter than the dry run circulation at that latitude indicates that at that latitude convection of $\theta_e \approx 310$K air effectively weakens the circulation. As a consequence, it displaces mass fluxes to higher θ_l, which is made possible by the poleward flux of moist air in the frontal region. As described previously, the frontal moist air with very high θ_e is lifted to isentropic levels much higher than $\theta_l = 310$K. This is nevertheless insufficient to compensate

[2]The cumulative streamfunction has been created by calculating first the cumulative mass flux joint distribution that we introduce later in subsection 3.4.2.

the weakening of the circulation caused by the large amount of convected $\theta_e \approx 310$K that rushes back equatorward along the $\theta_l = 310$K isentrope.

These subtleties can be better understood by considering the isentropic layer thicknesses. Equation (3.11) relates the dry circulation to a reorganization of air masses, $\langle \rho_{\theta_l} \rangle_t - \langle \rho_{\theta_l} \rangle_0$, and to the diabatic heating $\langle \rho_{\theta_l} \dot{\theta}_l \rangle_t$. In the dry run, the diabatic heating vanishes and the circulation is determined by the reorganization. In the moist run, we have seen that diabatic heating can become as important as the reorganization and since the culmulative circulation does not account for mass displacements in the vertical these motions are not captured by the circulation. One can analyze changes in $\langle \rho_{\theta_l} \rangle_t$ to infer the circulation for both moist and dry simulations as long as one only looks at horizontal reorganizations. Because ρ_{θ_l} is not conserved on parcels, convergences and divergences can create variations in ρ_{θ_l} values that are not related to mass transports.

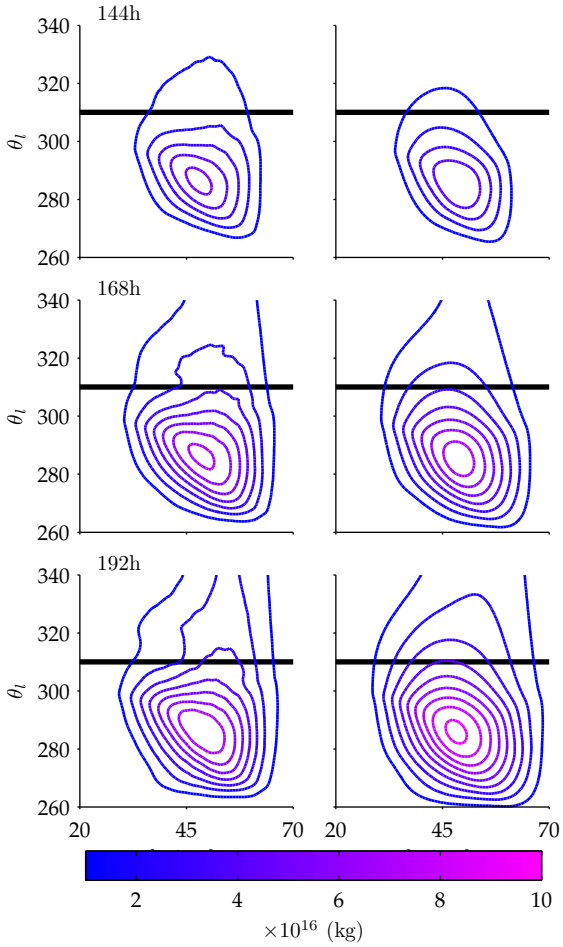

FIGURE 3.5. Comparison of circulation on dry isentropes for $\mathcal{H}_{\max} = 60\%$ on the left and dry on the right. The thick black line indicates the $\theta_l = 310$K isentrope previously discussed.

In Figure 3.6, we show the isentropic zonal average of $\langle \rho_{\theta_l} \rangle_t$ for the same case study as in Figure 3.2, Figure 3.3 and Figure 3.4. At first glance, it appears that the isentropic thicknesses are not too diffused by the motions and therefore a useful tool to track parcels motion. At 108h, both the dry and moist runs are similar. Both have thick layers at 30°N, 300K and 65°N and 265K, two regions that are joined by a strip of 1200 kg m^{-2} K^{-1} thickness layers. At 132h, this strip has already been quite deformed by 270K air at 60°N that has moved equatorward and 300K air at 45°N that has moved poleward, producing a patch of thick isentropic layers from 50°N and 280K to 60°N and 300K. In addition, the moist run exhibits air masses at around 45°N and 310K that appear to have been brought from 300K by convection.

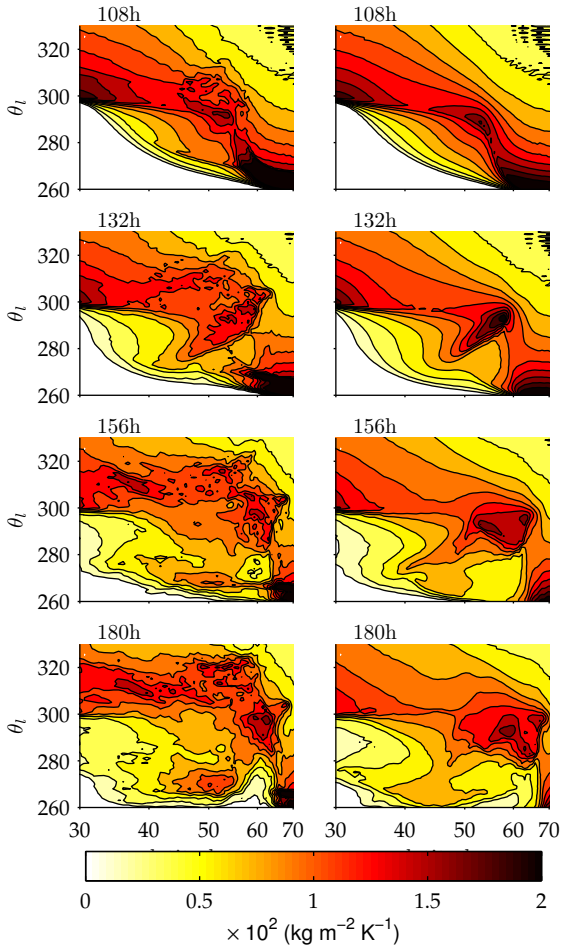

FIGURE 3.6. Comparison of zonal-mean dry isentropic layer thickness $\langle \rho_{\theta_l} \rangle_t$ on dry isentropes for $\mathcal{H}_{\max} = 60\%$ on the left and dry on the right. Contours are in 200 kg m^{-2} K^{-1} increments. The latitude axis is cosine-spaced, indicating that mass can be tracked by simple area integrals.

At 156h, the moist run have lifted most of the 1200 kg m^{-2} K^{-1} thicknesses between 40°N and 55°N to 310K but a noticeable patch of 1200 kg m^{-2} K^{-1} and higher thicknesses remains at 60°N and 300K. A similar

patch with even higher thicknesses can be found in the same region of the dry run from which a tongue of 800 kg m^{-2} K^{-1} thicknesses has been extracted and brought equatorward at 280K in the dry run. The corresponding mass transport in the moist run occurs at a lower potential temperature and seems to originate from higher latitudes. At this point in the life cycle, the moist run lowest contour reaches farther equatorward than the dry run lowest contour, an indication that the moist run has been subjected to a more vigorous circulation, consistent with our previous observations.

At 180h, the moist run has transported a substantial amount of 270K air from 60°N to 50°N and has been depleted of its 280K at that latitude. This air has been lifted through moist convection to higher potential temperatures. The dry run, on the other hand, has kept on pushing 280K air equatorward and its lowest contour now reaches out of our axes, which is not true for the moist run. This means the dry circulation equatorward branch has transported more mass than the moist run, once more a observation consistent with a weakening of the circulation due to moisture.

3.4.1.2 Moist Isentropic Analysis

If one wants to carry a similar analysis using θ_e instead of θ_l, one has to take into account that θ_e is not a stratified quantity in our simulations. Its isentropic layer mass, ρ_{θ_e}, therefore does not obey a mass conservation equation similar to equation (3.10). For the same reason, ρ_{θ_e} does not have a simple mathematical representation. Instead, one has to compute its zonal

average using a distribution definition:

$$\langle \rho_{\theta_e} \rangle_{\theta_e t} = \frac{1}{2\pi} \int_0^{2\pi} \int_0^{p_s} \delta(\theta_e' - \theta_e) \frac{dp}{g} d\lambda, \tag{3.14}$$

and similarly for its cumulative moist circulation, $\tilde{\Psi}_{\theta_e}$,

$$\tilde{\Psi}_{\theta_e}(\phi, \theta_e', t) = a \cos\phi \int_0^t \int_0^{2\pi} \int_0^{p_s} v H(\theta_e' - \theta_e) \frac{dp}{g} d\lambda dt. \tag{3.15}$$

The good news is that these two quantities can be studied in the same way as their dry counterparts as long as one does not insist in considering θ_e as a vertical coordinate. An advantage of using θ_e instead of θ_l is that since in our experiments θ_e is preserved by the dynamics to a high order, reorganizations of $\langle \rho_{\theta_e} \rangle_{\theta_e t}$ will occur along surfaces of constant θ_e. We plot the moist cumulative streamfunction (3.15) in Figure 3.7 and the zonal-mean moist isentropic mass distribution in Figure 3.8 for the same time series as for the dry analysis. We have not included the dry run diagnostics because since $\theta_e = \theta_l$ in this run the resulting plots would be the same as in Figure 3.5 and Figure 3.6.

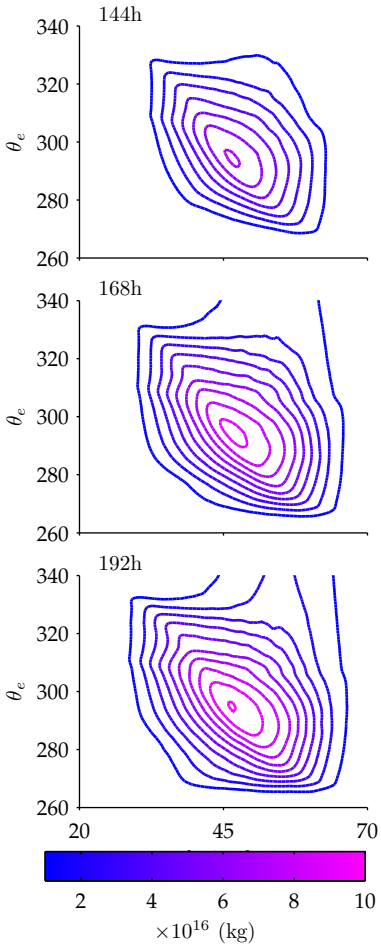

FIGURE 3.7. Moist circulation for $\mathcal{H}_{\max} = 60\%$.

The cumulative moist streamfunction appears to be very different from the dry circulation in Figure 3.5, reaching deep in the subtropics at $\theta_e \approx 330$K and 30°N. Already at 144h, moist surface subtropical air has been displaced

and because it has been replaced by drier midlatitudes air, the cumulative moist circulation takes place over a broad range of θ_e. As time progresses, the shape of the cumulative moist circulation does not change much but its maximum value increases monotonically and is always $\approx 2 \times 10^{16}$ kg higher than the corresponding dry circulation in the right panels of Figure 3.5. The most distinguishing features of the cumulative moist circulation are the nearly horizontal streamlines in the poleward branch between $\theta_e = 320$K and $\theta_e = 330$K. This is an indication that moist air parcels preserve their θ_e as they are transported poleward.

It is interesting to see how these features appear in the reorganization of $\langle \rho_{\theta_e} \rangle_{\theta_e t}$ in Figure 3.8. Because of the intimate link between the cumulative circulation and the isentropic circulation, one expects to see subtropical high-θ_e air being transported poleward horizontally. This is indeed happening with great amounts of $\theta_e \approx 320$K at 35°N being spread poleward all the way to 60°N at 180h. The late-time distribution of $\langle \rho_{\theta_e} \rangle_{\theta_e t}$ has a rather peculiar shape. It consists of a big patch of 1200 kg m^{-2} K^{-1} going from 30°N to 60°N at $\theta_e \approx 320$K that is somewhat disconnected from a patch of 1600 kg m^{-2} K^{-1} air with $\theta_e = 300$K at 60°N. Finally, there is a 800 kg m^{-2} K^{-1} patch of air cold $\theta_e \approx 270$K air between 45°N and 55°N. This distribution is very similar to the 180h distribution of $\langle \rho_{\theta_l} \rangle_t$ for the moist run of Figure 3.6. This indicates that the vast majority of moist ascents took place before 180h. This shows that while the implied circulation on dry isentropes can be weakened by moisture effects, important vertical mass fluxes on dry isentropes lead to large displacements. To study these moist ascents in detail we will use the mass flux joint distribution and the

techniques presented in chapter 2.

3.4.2 Net Isentropic Circulations

The discussion of the cumulative dry circulation based on Figure 3.5 showed an increasing function of time. It increases because it is related to the net meridional sensible heat flux, which never reverses during the evolution of the life cycle. While it does not reverse, it will come to a stop when the life cycle reaches its final stable balanced state. We therefore expect that the cumulative dry circulation will equilibrate rapidly after the long wave breaking.

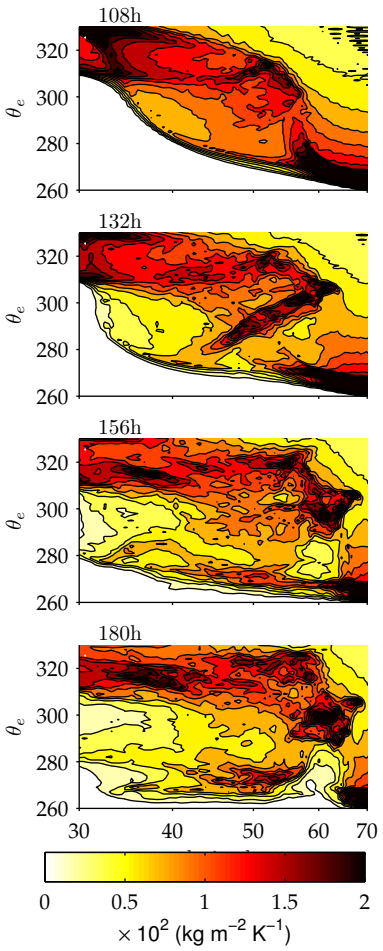

FIGURE 3.8. Zonal-mean moist isentropic mass $\langle \rho_{\theta_e} \rangle_{\theta_e t}$ on moist isentropic layers.

Computing time-averaged quantities in a transient system can prove to be tricky since one has to pick rather arbitrarily the time-scale of interest. When the transient system is a life cycle that transforms an unbalanced state into a balanced state, the net amount of reshuffling is expected to be unambiguously quantifiable. This net effect can indeed be analyzed with the help of the joint isentropic analysis, which records meridional mass fluxes according to which thermodynamical state they are occurring. The advantage of using the net isentropic analysis is that it removes the need to pick an averaging time-scale: the meridional masses fluxes are initially zero and slowly return

to a uniform vanishing value at the end of the life cycle, producing net mass fluxes that depend only on the final balanced state.

Due to this observation, we do not have to worry about all the details of the transient flow and we can describe meridional transports by investigating properties of the cumulative dry circulation at the end of our 20 days simulations. At that point, the wave is completely broken and all of the baroclinic adjustments have been accomplished. We will not restrain ourselves to the study of the cumulative dry circulation but will also investigates properties of the cumulative moist circulation as well as some features of the cumulative mass fluxes joint distribution. The method used to compute the mass flux joint distribution was presented in chapter 2 and a similar calculation is reproduced here. The only differences are that *1*) we do not have to interpolate in the vertical given our high resolution; *2*) we use θ_l instead of θ; *3*) we multiply the mass flux joint distribution by τ_{sim}, the simulation time. We use θ_l here because it is the true adiabatic invariant for a moist system, that reduces to θ wherever the air is unsaturated. In reanalysis data of chapter 2, large-scale condensation was not included and therefore θ_l and θ were interchangeable . In the simulations presented in this chapter, large-scale condensation makes the two potential temperatures slightly different. Because the difference makes θ_l an exact adiabatic invariant, we use this quantity. It moreover has the advantage that it would be conserved even if the precipitation time-scale was increased to large values. The mass flux joint distribution can then be used to compute the dry and moist circulations, the MR and the direction θ_e profiles. We integrated the simulations for twenty days with 3 hourly outputs, computed the mass flux

joint distribution (2.1) for each of these outputs and then summed then over the whole simulation. The life cycles eddy kinetic energy peaks around day 7 and slowly decays through day 15 and has essentially vanished at day 20. We begin by studying the impact of the boundary layer relative humidity and depth on the characteristics of the dry and moist circulations.

3.4.2.1 Change in Relative Humidity

Figure 3.9 shows the dry circulation, left, and the moist circulation, right, with varying relative humidity in a layer two and a half kilometers deep over a restricted the region of interest 20°N-70°N. Relative humidity increases from 20% to 80% from top to bottom and we consider potential temperatures from 260K to 350K for the dry circulation and the same range of equivalent potential temperatures for the moist circulation.

At 20% humidity, the dry circulation is made of a single overturning cell that peaks at 45°N and $\theta = 290$K for a value of 9×10^{16} kg. The streamlines are not closed for high θ_I, an indication that over the life cycle a net amount of mass is transported equatorward. With increasing relative humidity, the dry circulation begins to be deformed so much that it hints at an equatorward flow at 320K for 40%, 330K for 60% and 340K for 80%. This is accompanied by a steady weakening of the transport, that still peaks at 9×10^{16} kg in the 40% run but at 8×10^{16} kg and 7×10^{16} kg in the 60% and 80% runs, respectively.

The moist circulation peaks at 40°N for 20%, 60% and 80% but peaks at 35° for 40%. This peak increases from 11×10^{16} kg to 13×10^{16} kg as the relative humidity increase from 20% to 60% but is reduced to 12×10^{16} kg

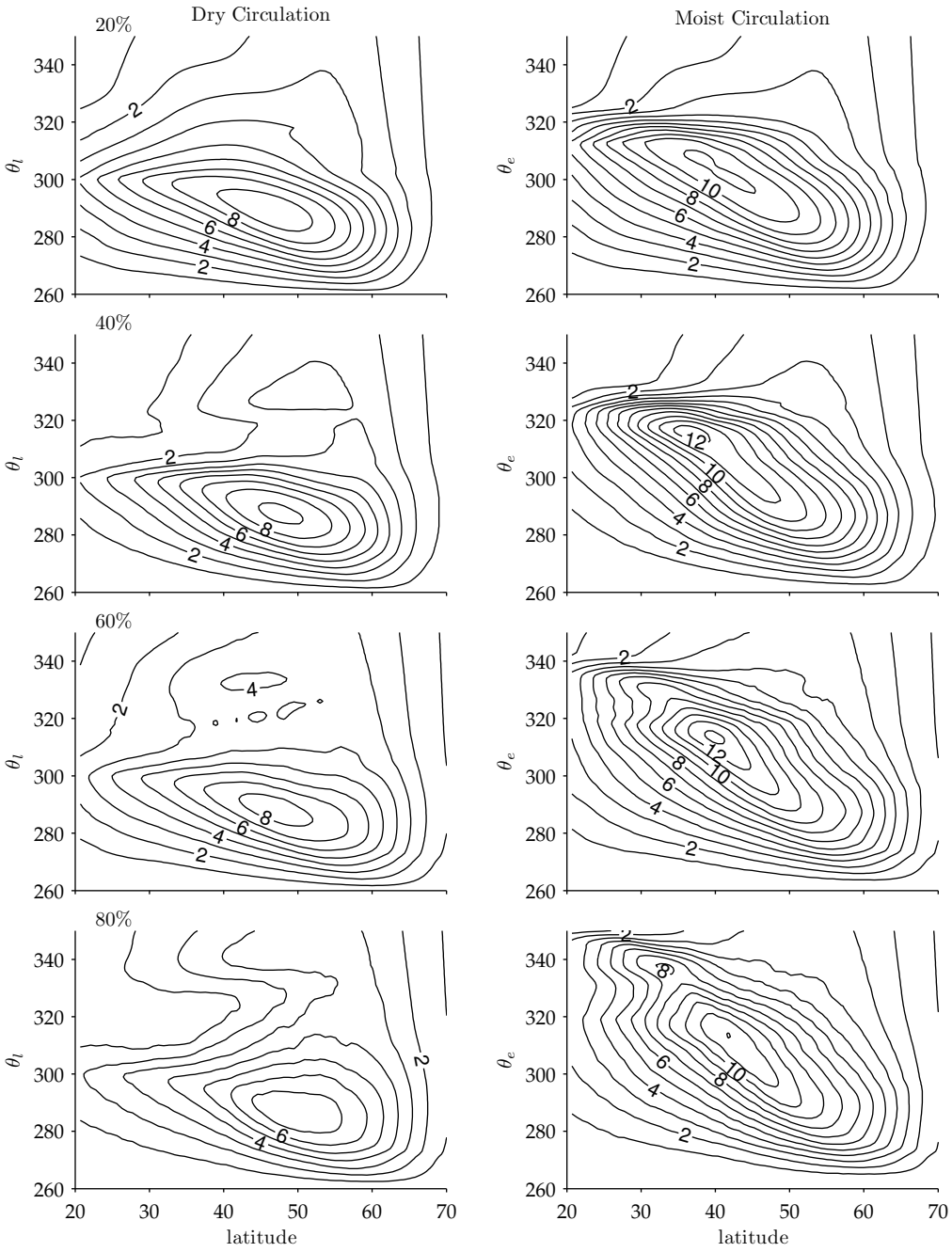

FIGURE 3.9. Dry and Moist Circulations for changing $\mathcal{H}_{\max}$ and fixed $\bar{z} = 2.5$ km. Contours are in 10^{16} kg increments.

when the relative humidity is further increased to 80%. The 20% peaks at 300K but all three other runs peak at 320K. The moist circulation extends to higher θ_e as relative humidity increases, getting as high as 340K at 80% between 30° and 40°.

The dry circulations in runs with 40% to 80% relative humidity have a complicated vertical profile that suggests a net equatorward flows in the free troposphere. These equatorward flows are taking place at $\theta_l \approx 320$K, between 40°N and 50°N. Considering that moist circulations are peaking at $\theta_e \approx 320$K, 40°N this is unlikely to be a pure coincidence. As described earlier using PV dynamics, as moist air ascends, it will settle on the θ_l surface corresponding to its θ_e. After it settles, this air will return southward, effectively creating a net equatorward flow in the free troposphere. Because these runs moist circulation peak at $\theta_e \approx 320$K the dry isentrope that will be the most influenced by this effect will be the $\theta_l \approx 320$K isentrope. This shows the non-trivial interaction between the dry and the moist circulations.

3.4.2.2 Change in Moist Layer Depth

In Figure 3.10, we show the same plots as in Figure 3.9 but for a varying moist layer depth, keeping the relative humidity fixed at 60%. The dry circulation for the 0.5, 1.5 and 5 km runs peak at 9×10^{16} kg while the 3.75 km run peaks at 10×10^{16} kg and the 2.5 km run peaks (third panel in the left column of Figure 3.9) at 8×10^{16} kg. Their peak is attained between 45°N and 50°N at $\theta_l \approx 290K$. From these observations, no clear trend strengthening trend with increased moisture can be deduced. Notwithstanding these ambiguous results, there are significant changes appearing in the

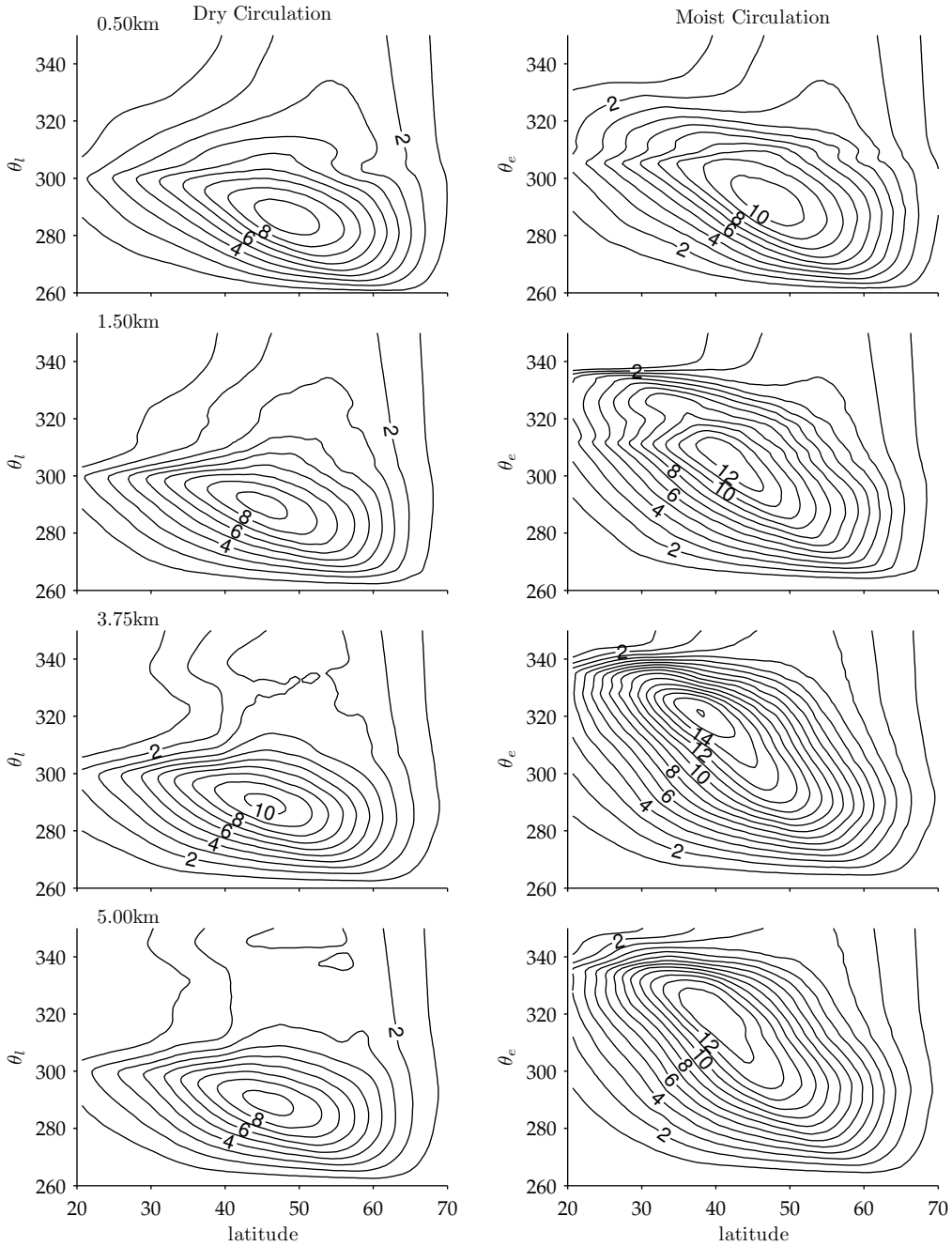

FIGURE 3.10. Same as Figure 3.9 but with varying $\bar{z}$ and fixed $\mathcal{H} = 60\%$.

free troposphere as the boundary layer is deepened. The presence of a net equatorward flow in the free troposphere was previously observed for the 40% to 80% runs. The addition of water vapor by increasing the moist layer depth appears to have a very different impact than the addition of water vapor through an changing relative humidity on the strength of the free tropospheric equatorward flow. Indeed, deformations in the dry circulation appear with increasing layer depth but it never becomes as dramatic as for the 80% case in Figure 3.9.

By contrast, the moist circulation is very sensitive to an increase in moist layer depth. The run with a moist layer 0.5 km deep and 60% relative humidity has a moist circulation that is very similar to its dry circulation but as the layer is deepened all of these similarities disappear. While the moist circulation did exhibit a clear dependence on relative humidity in Figure 3.9, it appears to be much more affected by a change in the moist layer depth, as depicted in Figure 3.10. The peak values attained go from 10×10^{16} kg at 0.5 km to 16×10^{16} kg at 3.75 km and then down to 13×10^{16} kg for a 5 km moist layer depth. The peak location is also sensitive to the layer depth as it tends to move equatorward and to higher equivalent potential values with increasing depth. At 0.5 km, the peak is attained at 45°N and θ_e =295K and at 3.75 km it is attained at 40°N and θ_e =320K. Its location for the 5 km simulation is more ambiguous. Considering that 5 km is almost twice the scale height for moisture, it suggests that deepening the moist layer beyond this level only adds little initial water vapor. This would explain why deepening the some moist layer further would not strenthen the moist circulation.

In this sequence of simulations, by keeping the relative humidity fixed at 60%, we are fixing the highest equivalent potential temperature to $\approx$ 340K. As we increase the moist layer depth, we are increasing the efficiency at which this moist air with a high θ_e can undergo moist slantwise convection. For a 0.5 km layer the moist circulation seems only slightly skewed toward higher θ_e at 30°N but for a 1.5 km layer there is clear extension of the moist circulation to $\theta_e = 340$K. This extension is not vigorous enough to directly affect the moist circulation peak but it is key in displacing this peak equatorward. At 2.5 km the moist circulation, which can be found in the third plot of the right panels in Figure 3.9, possesses some but not all of its poleward mass fluxes taking place at the highest θ_e. At 3.75 km the moist circulation now forms a single cell structure that remains relatively unchanged as the layer depth is increased to 5 km. For the two deepest layers, the poleward branch of the moist circulation from 20°N to 50°N is completely horizontal, which was previously identified as an indication that poleward flows of moist air takes place along slanted moist isentropes.

3.4.2.3 Indices

We extract several bulk measures from the dry and moist circulations by defining their average mass transports (Pauluis et al., 2010a), $\overline{\Delta\tilde{\Psi}_{\theta_l}}^N$ and $\overline{\Delta\tilde{\Psi}_{\theta_e}}^N$, as

$$\overline{\Delta\tilde{\Psi}_{\theta_l}}^N = \overline{\max_{\theta_l}\{\tilde{\Psi}_{\theta_l}(\phi,\theta_l)\}}^N - \overline{\min_{\theta_l}\{\tilde{\Psi}_{\theta_l}(\phi,\theta_l)\}}^N, \tag{3.16a}$$

$$\overline{\Delta\tilde{\Psi}_{\theta_e}}^N = \overline{\max_{\theta_e}\{\tilde{\Psi}_{\theta_e}(\phi,\theta_e)\}}^N - \overline{\min_{\theta_e}\{\tilde{\Psi}_{\theta_e}(\phi,\theta_e)\}}^N, \tag{3.16b}$$

where the operation $\overline{(\cdot)}^N$ is an average over the 25°N to 60°N latitudes. It is simply a uniform integral since $\tilde{\Psi}_{\theta_l}$ and $\tilde{\Psi}_{\theta_e}$ explicitly include the metric term $\cos\phi$. These quantities yield a measure of how much mass crossed a typical latitude. It will depend on the circulation peak and on its meridional extent.

Similarly, on could define the average meridional potential temperatures fluxes $\overline{\tilde{F}_{\theta_l}}^N$:

$$\overline{\tilde{F}_{\theta_l}}^N = 2\pi a \tau_{\text{sim}} \overline{\left[\int_0^{p_s} \theta_l v \frac{dp}{g}\right] \cos\phi}^N , \tag{3.17}$$

which instead of measuring how much mass crossed a typical latitude, measures how much potential temperature — or internal energy — has crossed a latitude.

For a fixed average mass transport, a circulation that has a narrower potential temperature extent will have a weaker flux and vice versa. This relationship works only when all of the circulation's streamlines are closed, which is generally true in midlatitudes climates (Pauluis et al., 2010a) but fails for our simulations. This shortcoming can however be fixed if we restrict ourselves to the lower part of the atmosphere and assume that all the relevant fluxes are realized between 260K and 350K, the region used in Figure 3.9 and Figure 3.10. In this case, one obtains after an integration by

parts[3]:

$$\begin{aligned}\tilde{F}_{\theta_l} &\approx \int_{260\mathrm{K}}^{350\mathrm{K}} \theta_l \partial_{\theta_l} \tilde{\Psi}_{\theta_l} d\theta_l, \\ &= \left[\theta_l \tilde{\Psi}_{\theta_l}\right]_{260\mathrm{K}}^{350\mathrm{K}} - \int_{260\mathrm{K}}^{350\mathrm{K}} \tilde{\Psi}_{\theta_l} d\theta_l. \end{aligned} \tag{3.18}$$

The first term would vanish is the circulations were closed but the second term would not. This second term can thus be understood as a measure of net fluxes associated with the shape of the circulation. Therefore, in order to quantify the heat transport with our open circulations, instead of (3.17), we use

$$\overline{\tilde{F}_{\theta_l}}^N = -\overline{\int_{260\mathrm{K}}^{350\mathrm{K}} \tilde{\Psi}_{\theta_l} d\theta_l}^N , \tag{3.19a}$$

$$\overline{\tilde{F}_{\theta_e}}^N = -\overline{\int_{260\mathrm{K}}^{350\mathrm{K}} \tilde{\Psi}_{\theta_e} d\theta_e}^N . \tag{3.19b}$$

This relationship between the mass transport and the potential temperature fluxes is shown in Figure 3.12 for the dry and moist circulations. In (i), we are plotting changes relative changes of $\overline{\tilde{F}_{\theta_l}}^N$ against relative changes of $\overline{\Delta\tilde{\Psi}_{\theta_l}}^N$. The reference values are the corresponding for the dry control run. Important negative variations in θ_l fluxes appear for all runs except for the lowest relative humidity and lowest moist layer thickness. Variations can be as large as -20%, indicating that in some of the moister and deeper runs the net flux of θ_l can be substantially reduced. The dry circulation, on the other hand, does not show a clear trend with increasing moisture. It confirms our observation that the dry circulation is only slightly affected by

[3]The approximation comes about only because we restrict ourselves to a limited region in θ_l space

the moisture. This reduction in flux and the limited influence of moisture on the dry circulation suggests that the circulation is acting over a narrower band of θ_l, in accordance with our previous analysis that the dry circulation appeared to be relatively unaffected below the $\theta_l = 300K$ isentrope.

The moist circulation offers a more robust dependence on moisture, with a strengthening of its mass transport consistent with a strong increase in fluxes of θ_e. As the θ_e flux increases by 100% for the moistest run, the moist mass transport increases by as much as 80% for our runs. This is in line with our observations that the moist circulations were broadening in the θ_e direction with increasing moisture content. Fixing a relative humidity, one observe that increasing the layer depth changes the moist entropy fluxes more than the moist circulation. On the opposite, by fixing the moist layer depth one sees that increasing the relative humidity does not change the moist entropy fluxes as much while increasing the moist circulation substantially. This indicates that the moist stratification is increasing faster for a changing moist layer depth than for a changing relative humidity.

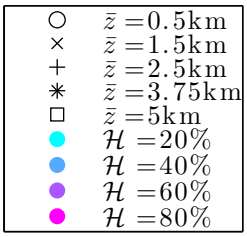

FIGURE 3.11. Legend for Figure 3.12, Figure 3.15 and Figure 3.17.

It is also interesting to note that the moist circulation does not increase by more than 80% as the moist layer approaches high relative humidity values. This seems to suggests that the heuristic picture presented in subsection 2.5.4 still holds for idealized baroclinic eddies. In this argument, we explained why the moist circulation should be at most twice as vigorous as the dry circulation. This conclusion held for a circulation with strong

eddies and weak eulerian-mean circulation, as it is the case for an isolated eddy life cyle.

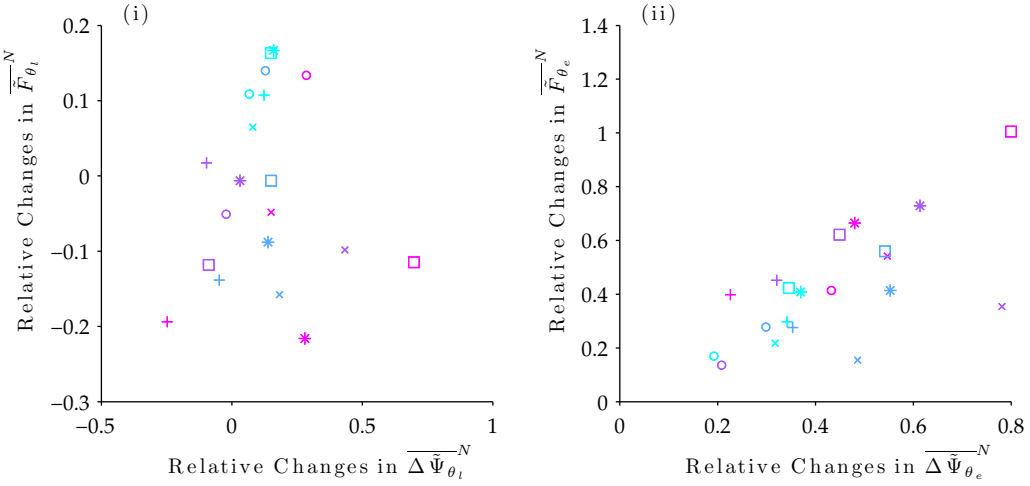

FIGURE 3.12. Comparison between entropy fluxes and isentropic circulation strength. (i) Relative changes in $\overline{\tilde{F}_{\theta_l}}^N$ against relative changes in $\overline{\Delta\tilde{\Psi}_{\theta_l}}^N$. (ii) Relative changes in $\overline{\tilde{F}_{\theta_e}}^N$ against relative changes in $\overline{\Delta\tilde{\Psi}_{\theta_e}}^N$. Legend is provided in Figure 3.11.

3.4.3 Moist Recirculation, Difference Circulation and EKE

In chapter 2, we have argued that the difference between the moist circulation and the dry circulation can be explained by using the decomposition of the joint distribution into its directional mass fluxes and their θ_e profiles. The directional mass fluxes are an important diagnostic tool since they allow one to observe on which dry isentropes the mass fluxes contributing to the moist circulation take place. This is a useful perspective because while θ_e is a good proxy for moist static energy, it is usually not stratified and therefore holds little information about the vertical position.

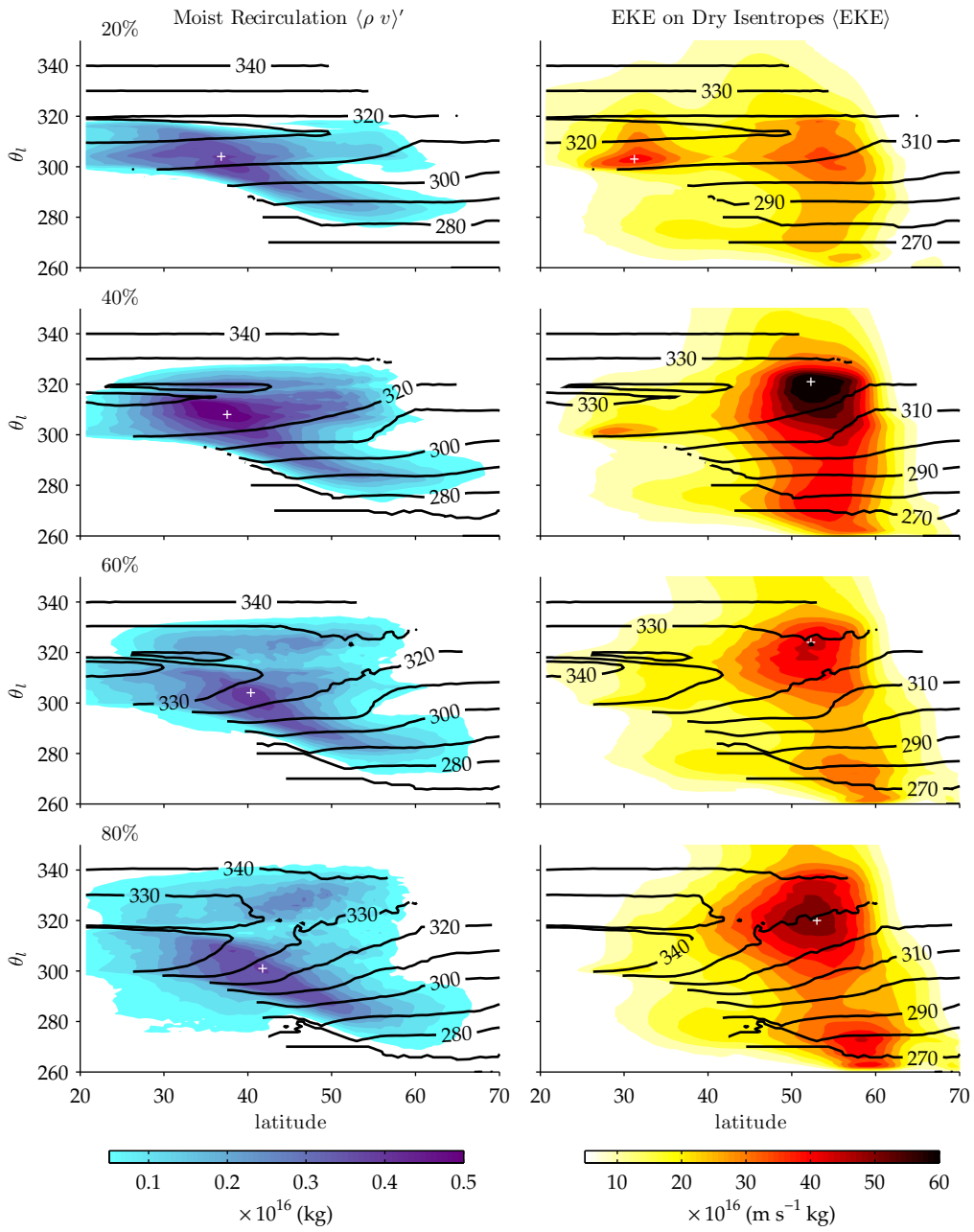

FIGURE 3.13. Moist Recirculation, left, and EKE, right, on dry isentropes for changing $\mathcal{H}_{\max}$. Solid black contours indicate $\langle \theta_e \rangle^+$ in 10K increments and are the same in the left and right panels for a fixed $\mathcal{H}_{\max}$.

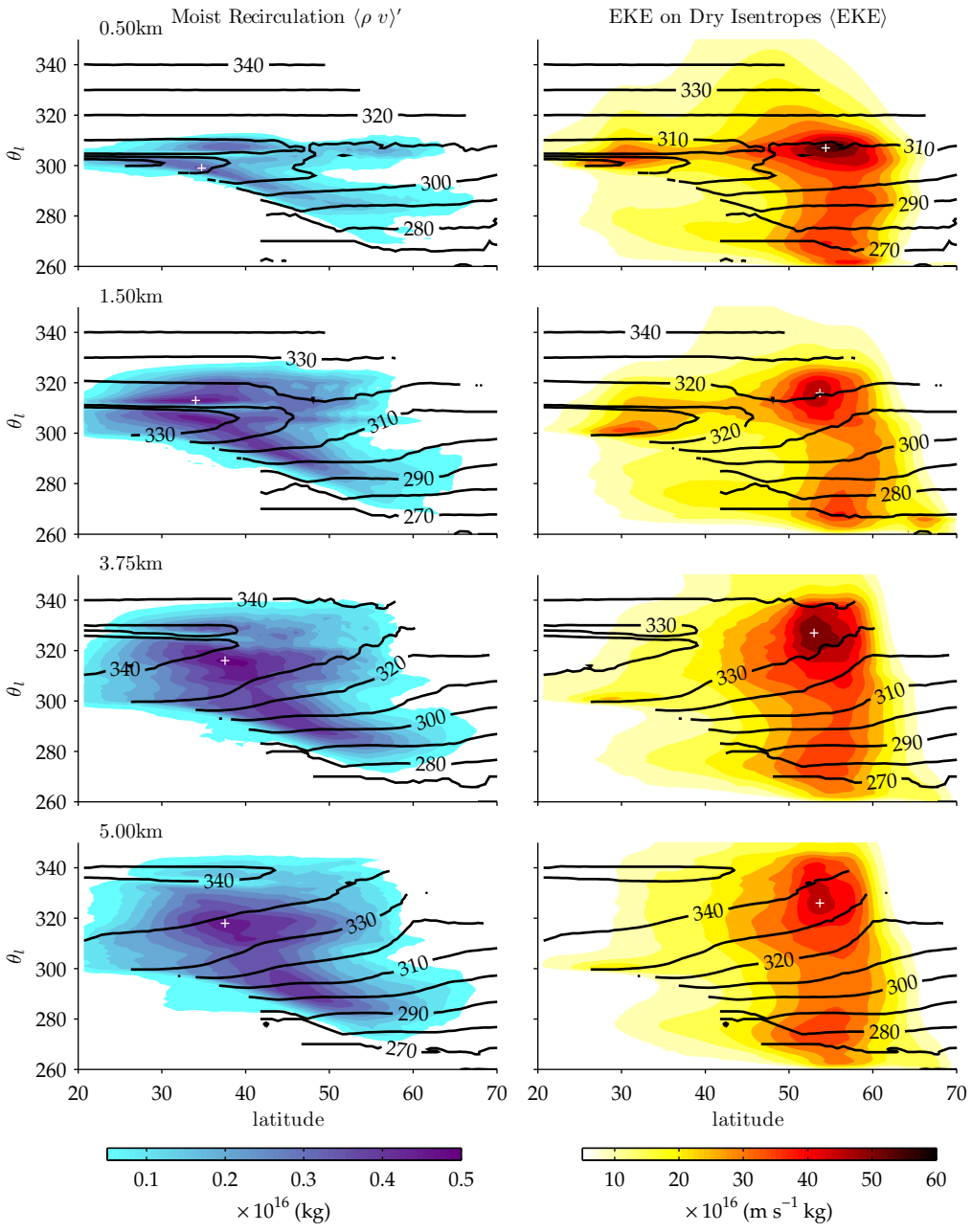

FIGURE 3.14. Recirculation, left, and EKE, right, on dry isentropes for changing $\bar{z}$. Same as Figure 3.9 but with varying $\bar{z}$.

In subsection 2.3.2, we have introduced the MR $\langle \rho v \rangle'$ as a way to quantity the added mass fluxes that contribute towards the moist circulation strength. Wherever the MR becomes significant, it is related to an important poleward flux of moisture on dry isentropes. Since there is a large difference of moisture content between the poleward branch and the equatorward branch of the MR, it was assumed that each of them were taking place at the θ_e of their corresponding directional mass flux. It was observed that the equatorward θ_e profile was mostly dry in the free troposphere and moist within the planetary boundary layer. The cause for such a moist equatorward flow in the boundary layer was explained by a re-moistening of the lower tropospheric air once it gets reinjected in the boundary layer. Considering that we do not have surface fluxes in our life cycle experiments, the equatorward flow does not get substantially remoistened and can thus be assumed to be dry.

All these considerations explain suggests that the MR and the poleward θ_e profile are the most relevant for the study presented in this chapter. We plot these two quantities for varying relative humidity in the left panels of Figure 3.13 and for increasing moist layer depth in the left panels Figure 3.14. The MR extends from about 30°N to 55°N with strong fluxes extending high in the free troposphere between 30°N to 45°N. The θ_e profiles have slanted moist isentropes connecting the 300K dry isentrope at 20°N to the upper troposphere at 60°N. The value of this moist isentrope depends on the surface relative humidity.

Changing the relative humidity does not appear to change the θ_l extent of the MR, which remains located between 300K and 320K at 40°N in

every plots of Figure 3.13. Increasing the layer depth, on the other hand, has an important effect, making the MR occupy an ever broader θ_l extent: between 300K and 305K for 0.5 km and between 300K and 340K for 4.5 km. These observations are consistent with the fact that the moist circulation θ_e extent is only marginally affected by changes in relative humidity but is substantially impacted by an increase in layer depth.

In all simulations except the ones with layer depth of 5 km, there is a mid tropospheric maximum of $\langle\theta_e\rangle^+$ equatorward of 40°N. When an air parcel from this region is pushed poleward by the underlying MR it will have to follow a discontinuous path, which means that it will be become convectively unstable. Such a motion was attributed to deep convection in chapter 2 and here it will lead to grid scale deep convective events. Fortunately, except for the 60% simluation of Figure 3.13 and the 2 km simulation shown in Figure 3.14, such poleward-moving air masses with this type of convective instability are not co-located with the regions of strong MR. In all other simulations, the poleward-moving air masses can follow their moist isentropes smoothly and, hence, will be predominantly driven by slantwise convection.

As it we have seen earlier from Figure 3.12, the moist circulation mass transport is correlated with θ_e fluxes, which is not true for the dry circulation and θ_l fluxes. One could then conclude that by adding moisture, we increase the moist circulation while slightly affecting the dry circulation. While this could be the end of the story, it proves more enlightening to consider changes of the moist circulation as compared to changes in the dry circulation. The difference between the two is expected to be related to

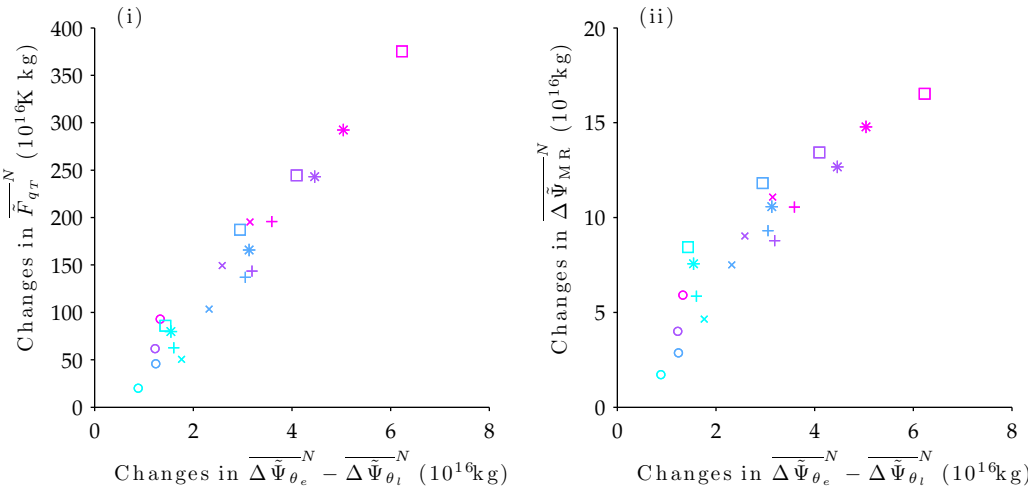

FIGURE 3.15. On the left, comparison between changes in moist fluxes and changes in difference circulations. On the right, correlation between the moist recirculation and the difference circulations. Legend is provided in Figure 3.11.

changes in poleward water vapor transport because the latent heat release during moist ascents is the only forcing that can strengthen the moist circulation. To verify this claim, we define the average difference mass transport, $\overline{\Delta\tilde{\Psi}_{\theta_e}}^N - \overline{\Delta\tilde{\Psi}_{\theta_l}}^N$ and define the average meridional moisture flux $\overline{\tilde{F}_{q_T}}^N$:

$$\overline{\tilde{F}_{q_T}}^N = 2\pi a \tau_{\mathrm{sim}} \overline{\left[\int_0^{p_s} (\theta_e - \theta_l) v \frac{dp}{g}\right] \cos\phi}^N , \tag{3.20}$$

where we have used the fact that $\theta_e - \theta_l \propto \theta q_T$. As such, $\overline{\tilde{F}_{q_T}}^N$ is not strictly speaking a moisture flux but it is nevertheless more convenient to use this approximation because it allows us to be consistent with our previous analysis in terms of θ_l and θ_e. Unlike the potential temperatures fluxes (3.19), the moisture flux (3.20) is not sensitive to whether the circulations are closed or not. Indeed, because q_T vanishes at the top of the atmosphere,

the open streamlines at the top of our domain do not transport any moisture.

One expects that as more moist air is being transported poleward, the moist and dry circulations adapt to account for the added latent heat release. This is indeed the case, as it can be observed in Figure 3.15(i), where we have plotted the changes in moisture flux versus the changes in difference circulation. The more a life-cyle transports moisture poleward, the stronger the moist circulation is with respect to the dry circulation. The discrepancy between the circulation can be understood in terms of the MR, for which we can compute the average, $\overline{\Delta\tilde{\Psi}_{\mathrm{MR}}}^{N}$:

$$\overline{\Delta\tilde{\Psi}_{\mathrm{MR}}}^{N} = \overline{\int_{260\mathrm{K}}^{350\mathrm{K}} \langle \rho v \rangle' \, d\theta_l}^{N} \, . \tag{3.21}$$

We plot in Figure 3.15(ii) the relationship between this quantity and the difference circulation. For every fixed moist layer depth, both appear to be related by a simple linear relationship that has an increasingly steeper slope with increasing moist layer depth. This comparison confirms that the difference circulation is set by the MR and therefore both concepts are interchangeable.

To understand the MR in terms of more typical measures of dynamical activity, we plot the cumulative eddy kinetic energy on dry isentropes. This quantity is computed in a same way as the dry cumulative circulation:

$$\langle \mathrm{EKE} \rangle = 2\pi a \tau_{\mathrm{sim}} \cos\phi \left\langle \frac{1}{2}(\mathbf{u} - \overline{\mathbf{u}})^2 \right\rangle , \tag{3.22}$$

where $\overline{\mathbf{u}}$ is the zonal-mean velocity on pressure surfaces[4]. The result is a

[4] As a reminder, $\langle \cdot \rangle$ represents a zonal and temporal mean on isentropic surfaces.

net EKE on isentropic surfaces and, because the EKE is a positive quantity, this is a fairly unambiguous construction. The right panels of Figure 3.13 and Figure 3.14 show this quantity with the corresponding MR in the left panels. For most simulations, it is confined between 45°N and 60°N, with a vertical extent comprised between 260K and 350K. The low moisture simulations, 0.5-1.5 km and 20%-40%, exhibit important $\langle \text{EKE} \rangle$ at 30°N and 300K, a feature that disappears for moister runs.

The $\langle \text{EKE} \rangle$ has a maximum between 300K and 340K, between 50°N and 60°N that we have indicated using a white plus sign (+). We have marked the MR's maximum in a similar way and one can see that it is a well-defined quantity for all simulations except for the 20% run in Figure 3.13. As the relative humidity increases, this maximum moves slightly to high potential temperature and towards lower latitudes. Increasing the moist layer depth, on the other hand, appears to primarily move the maximum to higher potential temperatures. One striking feature is that the $\langle \text{EKE} \rangle$ maximum occurs almost on the same moist isentrope as the MR maximum. The relation between θ_e at the $\langle \text{EKE} \rangle$ maximum and the θ_e at the MR maximum is shown in Figure 3.16. The correlation between the two is robust (apart from some outliers) and it appears that there is a systematic bias of $\langle \text{EKE} \rangle$ maximum being at θ_e slightly lower than the θ_e of MR maximum.

This hints at a possible correlation between high latitudes EKE and the lower latitudes MR. To quantify this correlation, one can construct a quantity that compares to (3.21) but using $\langle \text{EKE} \rangle$. This results in the peak

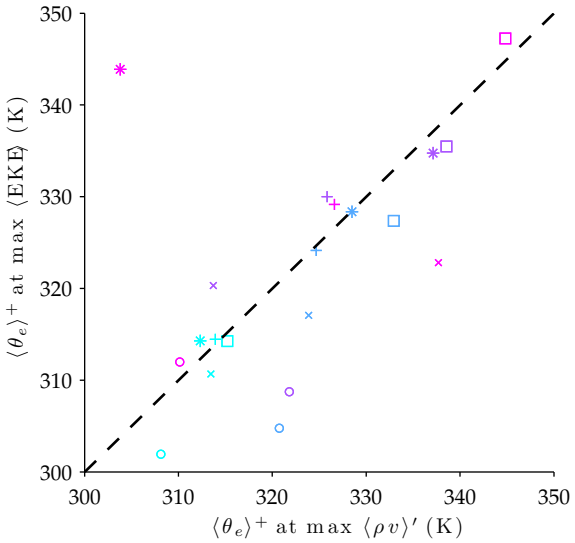

FIGURE 3.16. Comparison between the maximum EKE poleward θ_e and the maximum MR poleward θ_e. The equivalent potential temperatures are taken from Figure 3.13 and Figure 3.14 at the position of the white plus sign (+). Legend in Figure 3.11.

column-integrated EKE,

$$\overline{\overline{\text{EKE}}^N} = \overline{\int_{260\text{K}}^{350\text{K}} \langle \text{EKE} \rangle d\theta_l}^N \ , \tag{3.23}$$

which is a construction similar to equation (3.21). This comparison is shown in Figure 3.17(i) and shows a correlation between the increase in EKE and the increase in MR, the correlation being dependent on the layer depth. Indeed, it appears that at a fixed moist layer depth, as the relative humidity is reduced, the MR is not reduced as much as the EKE. This can be understood as an extreme sensitivity of the MR at low moisture contents. In low humidity runs, moist air masses and dry air masses are recorded differently by the joint distribution but are close in the (θ_l, θ_e) phase-space. This leads to a relatively strong MR that is associated with a relatively weak

transport of θ_e. To remove this effect, we plot in Figure 3.17(ii) the changes in MR from the 20% run at the same moist layer depth versus the same changes in EKE. While the correspondence is not perfect, it is much better, indicating a substantial correlation between the MR and the EKE.

The MR tracks the poleward moisture fluxes, the associated mass fluxes and the θ_e at which they occur. These are very important in the lower troposphere, equatorward of the jet, because this is where moisture is found. The moist air displacements diagnosed by the MR lead to slantwise convection along the moist isentropes defined by the poleward $\langle\theta_e\rangle^+$. Along the way, they perturb the PV dynamics which enhances the wave breaking processes. This enhancement is turns increases the amount EKE generated at the wave breaking. The MR is thus diagnosing the mass fluxes that are driving the EKE at higher latitudes. This shows a clear connection between moist ascents, increased dynamical activity and a resulting strengthened circulation.

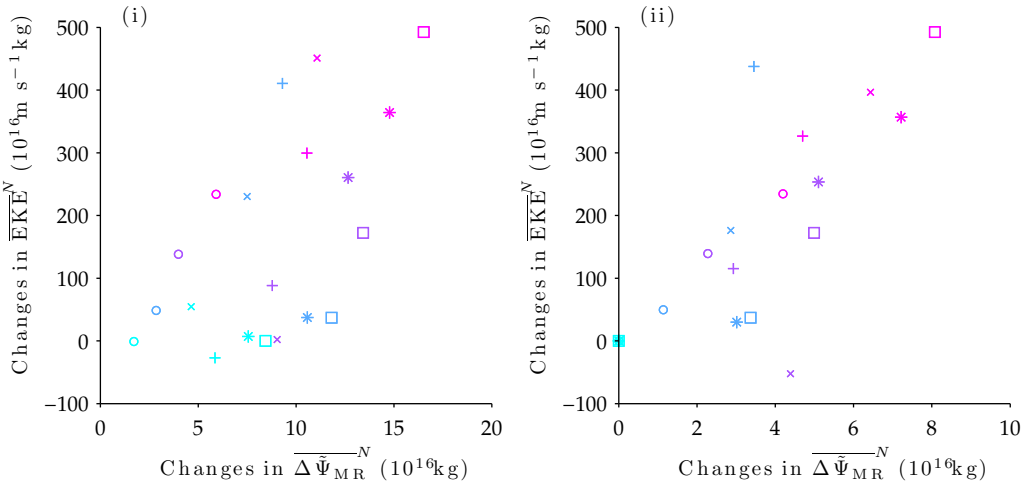

FIGURE 3.17. Comparison between the MR and EKE. In (i), differences from the dry run. In (ii), differences from the run at 20% with the same moist layer depth. Legend is provided in Figure 3.11.

3.5 Summary

Using an idealized atmospheric model, we conducted transient life cycle experiments to understand the moist isentropic circulations induced by an eddy taken in isolation. In our experimental setting, we have used idealized moist thermodynamics and have removed all diabatic forcings except those related to latent heat release. We thus have neither parametrized radiative cooling nor specified surface heat fluxes. Moreover, to ensure that moist entropy is conserved on fluid parcels we have not included any convective parametrizations. In summary, we have produced experiments with tractable physics that can used to check that the physical interpretations of chapter 2 for isolated baroclinic eddies hold.

First, we compared the dynamical evolution of a moist simulation with the evolution of a dry simulation. This exercise helped highlight important differences in the isentropic dynamics of the two paradigms. The moist simulation was shown to exhibit large upward mass fluxes that bring low-level moist air to the mid troposphere. When these convected air masses come from the midlatitudes surface, they create mid tropospheric negative PV anomalies. Because the convection occurs at higher latitudes, these anomalies tend to enhance the baroclinic wave strength. These negative PV anomalies were produced by vortex stretching and therefore associated with thick isentropic layers. The enhancement of the baroclinic wave tends to facilitate the equatorward transport of these air masses, essentially bringing low-PV air equatorward. When, on the other hand, the convected air masses come from the subtropical surface, they create mid tropospheric PV anomalies dipoles at the front. This effect was shown to be important

because it resulted in an eastward displacement of the baroclinic wave front. This displacement, it was argued, results in a positive feedback that end up increasing the baroclinic wave's zonal speed in the high latitudes. This increase in zonal wave speed shortens the growth phase of the wave thus making the baroclinic wave breaking happen earlier in the simulation. This wave braking phase is associated with a strong secondary eddy in the high latitudes, an eddy that was observed to be quite different in the moist run.

To understand the effect of these dynamical features on the heat transport, we have compared the cumulative circulation on dry isentropes for a moist simulation with the same circulation for dry simulation. In a development that parallels to the development of the PV dynamics that was just described, the circulation on dry isentropes for the moist simulation was shown to strengthen faster but ultimately result in less meridional mass transports. By further comparing the isentropic layer thickness for the two simulations, we demonstrated the important role diabatic heating has on reorganizing air masses from low isentropes to high isentropes. We concluded that moisture effects have a strong effect on the meridional redistribution of mass in dry isentropic coordinates, suggesting that a moist isentropic analysis should be used as presented in chapter 2.

The circulations on dry and moist isentropes were computed for a variety of simulations with a surface moist layer of uniform depth and uniform relative humidity. By varying the relative humidity, we varied the surface equivalent potential temperature and by changing the layer depth, we changed level at which moisture was active. The results were summarized by comparing the effects of moisture on the dry and moist circulation for a

fixed layer depth and varying relative humidity and vice versa. Increasing the relative humidity and deepening the moist layer was shown to weaken the dry circulation and strenghten the circulation on moist isentropes.

Added moisture was observed to weaken the circulation on dry isentropes mostly in the mid troposphere. In light of the comparative study between the moist and dry dynamics, this feature was attributed to the thick isentropic regions with negative PV anomalies moving back equatorward. The circulation on moist isentropes was not only strengthened but also shifted equatorward, towards the region where the frontal convection is the most important.

The strength of the two circulations were compared to their respective potential temperatures meridional fluxes. This analysis indicated that while there is robust reduction in meridional sensible heat fluxes it is accompanied with very weak changes in the dry circulation strength as more moisture is included. On the other hand, the moist circulation was observed to strengthen proportionally to the increase in equivalent potential temperature fluxes.

Using the theory developed in chapter 2, we were able to attribute most changes to the moist recirculation. We moreover used the poleward θ_e to assess which moist isentrope was followed by the poleward branch of the recirculation. Within this theoretical framework, we confirmed that for moist baroclinic eddies the moist recirculation could be quantified by the difference between the moist and dry total transport. In addition, we could show that the moist recirculation strength was directly correlated to moisture fluxes generated by the moist recirculation.

This assessment enabled us to relate changes in the isentropic circulations to changes in the moist recirculation. Following this connection, we set to study the relationship between the moist recirculation and eddy kinetic energy. To do this, we plotted the EKE on dry isentropes and noticed that its strength and position in the latitude-potential temperature plane was affected by moisture. In particular, we showed that the EKE maximum and the moist recirculation maximum in that plane was occurring on the same poleward θ_e. This suggests a connection between the two: for a fixed layer depth, the peak EKE increases with an increasing peak of recirculation.

The simulations created in the context of this chapter helped verify the dynamical assumptions invoked in chapter 2 to justify the physical interpretation of our results. The joint isentropic analysis had been previously justified because of the key role moist midlatitude eddies play in setting the circulation. While there was no doubts that this was true, it had not been clearly settled which features of the eddies the moist circulation was diagnosing that the dry circulation could not. By considering eddies in isolation with very simple physics, this role, and its dependence on the moisture content, could be investigated. In doing so, we observed that the two circulations reacted very differently to an increase in moisture, thus indicating that the moist circulation could indeed better capture the ascending motions than the dry circulation.

By adding moisture, we could see the moist circulation strengthen by the action of slantwise convection, which connects the tropical surface equivalent potential temperature with the poleward branch of the eddies,

all the way to high latitudes. Moist air was seen to be advected along dry isentropes in the frontal zone and subsequently brought to higher dry isentropes. This process was associated with important dynamical effects on the baroclinic wave, effectively causing a vigorous mixing zone on moist isentrope followed by poleward-moving air.

These observations are fundamental because they highlight the non-local role of moisture in changing the dynamics of moist baroclinic eddies. While many previous studies investigated normal modes with saturated initial conditions, in this study we began with moist initial conditions that were conditionally unstable to slantwise convection. This setting created simulations that begin as dry long baroclinic waves but that transform into smaller-scale disturbances that create important PV anomalies.

Even thought the eddies studied in this chapter are idealized, they are exhibiting sensitivities to moisture that are expected to transpose to eddies in a moister climate. For instance, it appears clear from this study that the dry circulation induced by baroclinic eddies is a poor proxy for the actual eddy activity in midlatitudes. The moist recirculation and the moist circulation seem to be a better indicators of the dynamical activity produced by the eddies. Because of the observed connection between EKE at the wave breaking and the amount of moist recirculation, an increase in moist recirculation due to a changing climate would suggests that the underlying eddies would become more kinetically active. culation.

Chapter 4

Moist Eddies in a Global Warming Scenario

Partially Reproduced from Laliberté and Pauluis (2010) by permission of American Geophysical Union.

4.1 Context

Climate change through this century is expected to be associated, among other things, with a change in the atmospheric energy, entropy and water vapor transports. A fundamental issue is to understand how such changes in atmospheric transports are tied with changes in the atmospheric circulation itself. For example, a larger energy transport can be associated with an increase in the overall mass transport or, alternatively, with an increase in the energy transported per unit mass of air. Several studies (Held and Soden, 2006; Mitas and Clement, 2006; Vecchi and Soden, 2007; Chou and

Chen, 2010, etc.) have investigated changes in the tropical circulation due to global warming. Using twentieth century and A1B scenario twenty-first century model runs, Held and Soden (2006) observe that the increase in atmospheric water lead to a rapid increase in the tropical stratification, of approximately 7%/K, consistent with the Clausius-Clapeyron (CC) relationship. In contrast, the poleward energy transport by the circulation only increase by 2%, which thus imply a reduction of the mass transport in the Hadley cell by about 5%. With the use of a different ensemble of models, Mitas and Clement (2006) show trends for the twentieth century indicating a statistically significant weakening of the winter Hadley cell.

The arguments presented by Held and Soden (2006) are valid for the tropical regions where the mean overturning circulation dominate the energy transport. However, the same transport in the midlatitudes is dominated by large-scale eddies. In this chapter, we use the diagnostics developed in chapter 2 to characterize the changes in mass and entropy transports, with the later being viewed here as an ersatz for the energy transport. We compare the circulation on dry isentropes, similar to surfaces of constant potential temperature θ, with that on moist isentropes, similar to surfaces of constant equivalent potential temperature θ_e. As shown in the chapter 2, the two circulations differ in their strength, with the moist circulation being more vigorous in the midlatitudes due to the ascent of moist air within the stormtracks (Pauluis et al., 2008, 2010a). We view the circulations evolution under climate change with the perspective that moist baroclinic eddies will be the midlatitudes features that are the most affected by warming surface temperatures. Because of this approach, the moisture

influence on the eddies dynamic discussed in chapter 3 will provide a basis for the physical interpretations described in this chapter.

We further investigate the impact of the climate scenario on the meridional overturning circulation by studying the model-averaged mass flux joint distribution. We favor the diagnostics tools developed for the reanalyses in chapter 2. In our study, we replicate most of the figures found in that chapter to relate changes in surface temperature to changes in the vertical profile of MR and directional moist stratification. In the next section, section 4.2, we describe our diagnostics, which differ slightly from those presented in earlier chapters, and in section 4.3 we present our results.

4.2 Analysis

4.2.1 Data and Methodology

We use outputs from the World Climate Research Programme (WCRP) Coupled Model Intercomparison Project phase 3 (CMIP3) multi-model dataset, based on the Intergovernmental Panel on Climate Change (IPCC) Fourth Assessment Report (AR4) A1B scenario. The data was acquired from the CMIP3 archive of daily outputs for the 20$^{\text{th}}$ century and the A1B scenario (Meehl et al. (2007)). The NCAR CCSM3 daily model output is an exception: it was obtained from the NCAR data repository (runs 030e and 040e). Some models were removed from our analysis, in all cases for technical reasons, including missing data. A list of the included models is made available in Table 4.1.

In this chapter, we somewhat depart from the conventions of previous chapters and follow Pauluis et al. (2010a) to process our data using the dry entropy, s_l[1], and the moist entropy, s_m. From equations (1.48) and (1.56) it is clear that s_l and s_m are functionally equivalent to θ_l and θ_e, respectively. We can thus use either the entropies or the potential temperatures to process the data, without affecting the results. On a qualitative level, dry isentropes are close to surfaces of constant dry static energy and moist isentropes are close to surfaces of moist static energy, and the dry and moist entropy transports are similar to the dry and moist static energy transports. One could use the static energy instead of entropy, as in Czaja and Marshall (2006), though this comes at the cost of losing the exact conservation of

[1]We use the expression (1.45) with $e_0 = \frac{1}{2}p_0 = 10^5$Pa. Note that some of the results that follow can be affected by this choice.

TABLE 4.1. List of analyzed models with daily output

Laboratory	Model
GFDL, USA	cm 2.0
GFDL, USA	cm 2.1
CNRM, France	cm 3
CSIRO, Australia	mk 3.5
GISS, USA	Model ER
MIROC, Japan	3.2 Medres
MIROC, Japan	3.2 Hires
MIUB, Germany	echo G
MPI, Germany	echam 5
MRI, Japan	cgcm 3.2.2a
CCCMA, Canada	cgcm 3.1 t63
IPSL, France	cm 4
INGV, Italy	echam 4
NCAR, USA	ccsm 3.0

Models are listed by their laboratory of origin and their model numbers.

entropy for reversible adiabatic motions.

Using the moist entropy and the liquid water entropy instead of the potential temperature and the equivalent potential temperature is somewhat arbitrary due to the correspondences described by equations (1.48) and (1.56). Moreover, Pauluis et al. (2010a) showed that the mass fluxes joint distribution, which has been used to produce our analysis is insensitive to such a change of variables.

We define the dry streamfunction, $\Psi_d(\phi, s_l)$, and the moist streamfunction, $\Psi_m(\phi, s_m)$, using a formulation similar to equations (2.2) and (2.10) of

chapter 2:

$$\Psi_d(\phi, s_l) = \int_0^{s_l} \int_{-\infty}^{\infty} M(\phi, s_l', s_m') ds_m ds_l, \tag{4.1a}$$

$$\Psi_m(\phi, s_m) = \int_0^{s_m} \int_{-\infty}^{\infty} M(\phi, s_l', s_m') ds_l ds_m. \tag{4.1b}$$

The mass flux joint distribution $M(\phi, s_l, s_m)$ is presented in section 2.2 and the method used for its computation is described in the appendix. Before we computed M, we preprocessed the model outputs by linearly interpolated them on a fine pressure grid of $\approx$ 1kPa spacing. This was necessary to prevent the appearance of layered features in the joint distribution.

In order to compute the model-averaged mass flux joint distribution, M_{avg}, we have spline-interpolated the mass flux joint distribution onto 128 equally-spaced latitudes between 85°S and 85°N. The resulting ensemble of joint distributions was added to give

$$M_{\text{avg}}(\phi, s_l, s_m) = \frac{1}{\#\text{ of model}} \sum_{\text{model}} M(\phi, s_l, s_m), \tag{4.2}$$

which will be used to analyze changes in the directional quantities of chapter 2. Because different models have a different warming rates, the model average mass flux joint distribution is not expected to represent all features accurately. An alternative, that we will not investigate in this thesis, would be to use M_{avg} for the twentieth century and compute the model average change in joint distribution, weighted by the expected surface warming.

To ensure a strict mass conservation at each latitude we have have applied a filter that makes the joint distribution sums to zero. At a given

latitude, the exact procedure depends on whether M sums to a positive or to a negative number. If it is negative (positive, resp.), then we multiply the positive (negative, resp.) part of M by the appropriate factor to make the joint distribution sum to zero. This process can be described with the following filter:

$$M(\phi, s_l, s_m) = \max\{A(\phi), 1\} \max\{M(\phi, s_l, s_m), 0\} + \dots \\ \max\{A(\phi)^{-1}, 1\} \min\{M(\phi, s_l, s_m), 0\},$$

$$A(\phi) = \left(\int_{-\infty}^{\infty} \int_{-\infty}^{\infty} - \min\{M(\phi, s_l, s_m), 0\} ds_l ds_m \right) \Big/ \dots \\ \left(\int_{-\infty}^{\infty} \int_{-\infty}^{\infty} \max\{M(\phi, s_l, s_m), 0\} ds_l ds_m \right).$$

4.2.2 Circulation indices

We mimic the analysis used in chapter 3 and synthesize some features of the circulation by extracting a small number of indices from the full streamfunctions Ψ_d and Ψ_m. The total mass transport on s_l, $\Delta\Psi_d$, and the total mass transport on s_m, $\Delta\Psi_d$ is defined by:

$$\Delta\Psi_d(\phi) = \max_{s_l}\{\Psi_d(\phi, s_l)\} - \min_{s_l}\{\Psi_d(\phi, s_l)\}. \tag{4.3}$$

The dry entropy transport is given by[2] :

$$F_{s_l}(\phi) = -\int_{-\infty}^{\infty} \Psi_d(\phi, s_l) ds_l. \tag{4.4}$$

A similar expression can be found for $\Delta\Psi_m$ and F_{s_m} by replacing s_l with s_m in (4.3) and (4.4). We have chosen to rely on bulk quantities averaged over the regions 25°N-60°N and 60°S-25°S. As presented in Pauluis et al. (2010a), in these regions $\Delta\Psi_m$ dominates $\Delta\Psi_d$. We define the *total circulation index* as the average value

$$\overline{\Delta\Psi_m}^N = \frac{1}{35}\int_{25°\mathrm{N}}^{60°\mathrm{N}} \Delta\Psi_m(\phi)\, d\phi. \tag{4.5}$$

Note that the differential area element is implicitly included in (4.1), making this average area-weighted. This is the same average used in chapter 3. For our analysis, we also require a measure of the entropy transport, F_{s_m}, over these regions. Using the same average as for (4.5), we define

$$\overline{F_{s_m}}^N = \frac{1}{35}\int_{25°\mathrm{N}}^{60°\mathrm{N}} F_{s_m}(\phi) d\phi, \tag{4.6}$$

which, in turn, enables us to find a related hemisphere-wide *effective stratification* in a way that mimics a similar quantity described in Pauluis et al. (2010a), $\overline{\Delta s_m}^N$:

$$\overline{\Delta s_m}^N = \frac{\overline{F_{s_m}}^N}{\overline{\Delta\Psi_m}^N}. \tag{4.7}$$

[2]This quantity was actually computed as $F_{s_l}(\phi) = 2\pi a \cos\phi \left[\int_0^{p_s} s_l v \frac{dp}{g}\right]$, which was shown in section 3.4 to be equivalent.

The effective stratification (4.7) measures the difference of s_m between the poleward branch and the equatorward branch of the circulation. It depends not only on vertical stratification, but also on horizontal fluctuations of s_m in the midlatitude eddies. Quantities (4.5), (4.6) and (4.7) can be extended for the dry circulation and the southern hemisphere. We will refer to $\overline{\Delta\Psi_d}^N$ and $\overline{\Delta\Psi_d}^S$ as the *dry branch indices*.

Pauluis et al. (2010a) show that the difference between the transport on s_m and on s_l is associated with a poleward mass flow of warm subtropical air that ascends through the stormtracks. The enhanced mass transport on s_m, $\Delta\Psi_m(\phi) - \Delta\Psi_d(\phi)$, is used here to quantify the ascent of moist air within the stormtracks. The difference $F_{s_m}(\phi) - F_{s_l}(\phi)$ is proportional to the difference of q_T between the poleward flow and the equatorward flow, multiplied by the mass transport within the moist branch. Finally, an effective moisture stratification is defined as

$$\overline{\Delta q_T}^N = \frac{\overline{F_{s_m}}^N - \overline{F_{s_l}}^N}{\overline{\Delta\Psi_m}^N - \overline{\Delta\Psi_d}^N}, \tag{4.8}$$

an expression that is proportional to the difference in specific humidity between the poleward and equatorward flows.

4.2.3 Moist Recirculation Indices

In equation (2.6) of chapter 2 we proposed a precise measure of the MR. It represents the cancellations within the dry isentropic average and is responsible for the enhanced circulation on moist isentropes. For this

reason, its total value at each latitude,

$$\Delta\Psi_{\mathrm{MR}}(\phi) = \int_0^{\infty} \langle \rho v \rangle' \, d\theta, \tag{4.9}$$

is expected to be related to difference $\Delta\Psi_m(\phi) - \Delta\Psi_d(\phi)$, as was shown in chapter 3 for isolated eddies. One of the assumption underlying equation (4.8) is that all of the moisture transport occurs within the MR, which is not necessarily true given the large moisture fluxes taking place in the mixed layer. The mass fluxes associated with the MR circumvent this problem by excluding the surface equatorward flows. Therefore, if one quantifies moisture fluxes at each latitude $F_{q_T}^{\mathrm{MR}}$ related to the MR, one explicitly removes these equatorward moisture transports:

$$F_{q_T}^{\mathrm{MR}} = \int_{-\infty}^{\infty} \left(\langle s_m \rangle^{+} - \langle s_m \rangle^{-} \right) \langle \rho v \rangle' \, ds_l. \tag{4.10}$$

Since within the MR the equatorward s_m is mostly dry, this moist entropy flux is equivalent to the MR moisture flux. After averaging the total MR (4.9) and the MR moisture fluxes (4.10) over the midlatitudes as in equation (4.5) and equation (4.6), we can obtain a MR moisture stratification $\overline{\Delta q_T^{\mathrm{MR}}}^N$,

$$\overline{\Delta q_T^{\mathrm{MR}}}^N = \frac{\overline{F_{q_T}^{\mathrm{MR}}}^N}{\overline{\Delta\Psi_{\mathrm{MR}}}^N}, \tag{4.11}$$

and similarly for the southern hemisphere.

The circulation indices presented in this section are providing an extension to the circulation indices of subsubsection 3.4.2.3 that is applicable to the IPCC model outputs.

4.3 Results

Seasonal averages of (4.5) and (4.6) were computed for the twentieth century 1961-2000 and A1B scenario twenty-first century 2046-2065 and 2081-2100 periods. Changes between 2046-2065 and 1961-2000 as well as between 2081-2100 and 1961-2000 were computed. In Figure 4.2, Figure 4.3, Figure 4.4 and Figure 4.5, we present our results as scatter plots for both hemispheres and both solstice seasons, JJA and DJF. For each analyzed model, two data points will appear in each plot, one — filled — for the change between 1961-2000 and 2046-2065, and a second — not filled — for the change between 1961-2000 and 2081-2100, and the numerical values for the mean and variance of the model ensemble are presented in Table 4.2.

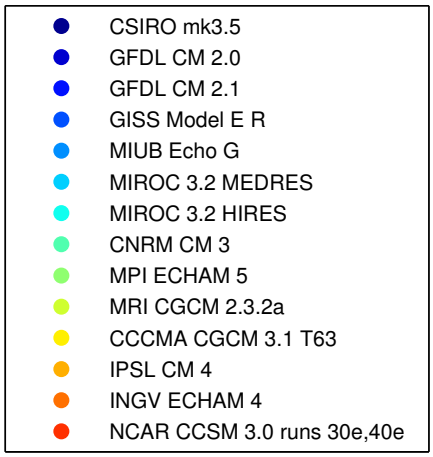

FIGURE 4.1. Legend for Figure 4.2 to Figure 4.5.

4.3.1 Changes in Indices

Figure 4.2 show the changes in dry entropy transport versus changes in the dry circulation for DJF and JJA of both hemispheres. In all cases, most models are found in the third quadrant, corresponding to a reduction in dry entropy transport and a reduction in mass transport by the dry branch. The mass transport weakens with changes between -1.7%/K and -5.3%/K. The weakening is less pronounced in the Winter hemispheres. There is also a large inter-model spread in the prediction for the northern summer

TABLE 4.2. Summary of statistics from figures Figure 4.2, Figure 4.3, Figure 4.4 and Figure 4.5.

Quantity		DJF		JJA	
		North	South	North	South
Dry	Circulation	**-1.7**±0.8	**-2.4**±2.3	**-4.1**±1.7	**-5.3**±1.5
	s_l Stratification	0.7± 0.8	-2.1±3.1	-5.9±8.9	**3.4**±2.0
	s_l Fluxes	**-1.0**±0.9	**-4.5**±2.0	**-9.9**±8.6	**-1.9**±1.5
Moist Branch	Circulation	**3.8**±1.4	-2.7±3.2	0.7±2.2	**1.8**±1.2
	q_T stratification	**1.9**±1.0	**10.4**±3.8	**4.9**±2.0	**6.0**±2.2
	q_T Fluxes	**5.7**±1.5	**7.7**±2.4	**5.5**±1.8	**7.8**±1.9
MR	Mass Fluxes	**3.9**±1.5	0.3±1.5	-1.0±1.5	**4.0**±1.3
	q_T Stratification	**4.3**±2.1	-0.9±2.0	-0.1±1.2	0.7±1.2
	q_T Fluxes	**8.3**±3.4	-0.7±3.0	-1.2±2.6	**4.6**±1.7
Total	Circulation	0.5±0.8	**-2.5**±2.0	-1.0±1.2	**-1.4**±1.0
	s_m Stratification	**0.9**±0.4	**5.2**±2.1	**2.2**±0.6	**4.1**±1.7
	s_m Fluxes	**1.4**±0.9	**2.7**±1.3	1.2±1.5	**2.7**±1.3

The numbers listed indicate the ensemble average of the quantity in the first column. The error is the standard deviation from the model ensemble. We have indicated in **bold** the results that fall outside one standard deviation of no changes.

(Figure 4.2), which is explained in part by the fact that the circulation on s_l is at its weakest during this season, and is thus most sensitive to large fluctuations. The dry entropy transport only weakens significantly during the summer season (-9.9%/K in the North and -4.5%/K in the South), and much less (-1.0%/K and -1.9%/K, respectively) during the winter.

The change in effective stratification can be obtained by subtracting changes in mass transport from changes in dry entropy transport:

$$\frac{1}{\overline{\Delta s_l}^N}\frac{\delta\overline{\Delta s_l}^N}{\delta T} = \frac{1}{\overline{F_{s_l}}^N}\frac{\delta\overline{F_{s_l}}^N}{\delta T} - \frac{1}{\overline{\Delta\Psi_d}^N}\frac{\delta\overline{\Delta\Psi_d}^N}{\delta T}. \tag{4.12}$$

In equation (4.12), $\delta(\cdot)$ refers to the value in one of the period of the twenty-first century minus the corresponding value in the twentieth century. The temperature T corresponds to the area-weighted average surface temperature over the the same regions (60°S-25°S and 25°N-60°N).

In Figure 4.2, the diagonal line with slope unity indicates the mean value for the change in stratification, which can be read at its intersection with the ordinate axis. The stratification increases in the Southern hemisphere by 3.4%/K in the summer, and decreases by -2.1%/K during the winter. Changes in the stratification are less pronounced during Northern winter (increasing by 0.7%/K) and unreliable during the Northern summer, where the dry circulation is particularly weak. In all cases, these changes are significantly less than the expected changes in tropical stratification associated with CC scaling. In contrast to the changes in the tropical circulation noted by Held and Soden (2006), the weakening of mass transport on dry isentropes in the midlatitudes appears to primarily due to a reduction of the poleward transport of dry entropy, with a lesser impact from changes

in stratification.

Figure 4.3 shows changes in the moisture transport $\overline{F_{s_m}} - \overline{F_{s_l}}$, versus changes in the moist branch index $\overline{\Delta\Psi_m} - \overline{\Delta\Psi_d}$. The multi-model ensemble mean shows a marked increase in moisture transport in the North at 5.7%/K in DJF and 5.5%/K in JJA, and in the South at 7.7%/K in DJF and 7.8%/K in JJA. The mass transport by the moist branch increases also significantly during the winter, by 3.8%/K in the North and 1.8%/K in the South, but decreases in the Southern summer by -2.7%/K while remaining almost unchanged (increasing by 0.7%/K with a standard deviation of 2.2%/K) during the Northern summer. The diagonal line shows the mean change in effective moisture stratification. In both hemispheres, summer eddies have a higher moisture stratification change than the winter eddies' (4.9%/K vs 1.9%/K for the north and 10.4%/K vs 6.0%/K for the south).

During summer, the increase in water vapor transport can be associated with an increase in humidity content between the dry equatorward and moist poleward flow that is roughly consistent with the CC scaling, associated with a small weakening of the mass transport. In contrast, relative changes in moisture content are smaller during winter, and the increase in water vapor transport is tied to an increase in the mass flow of warm moist air into the stormtracks. This increase in the mass transport by the moist branch of the circulation during the winter is remarkable, given that the dry circulation on s_l is expected to weakens in both the tropics and the midlatitudes. Based on these diagnostics, it is expected that through the next century, midlatitudes eddies will extract a larger amount of warm, moist subtropical air that will rise within the stormtracks. This analysis points

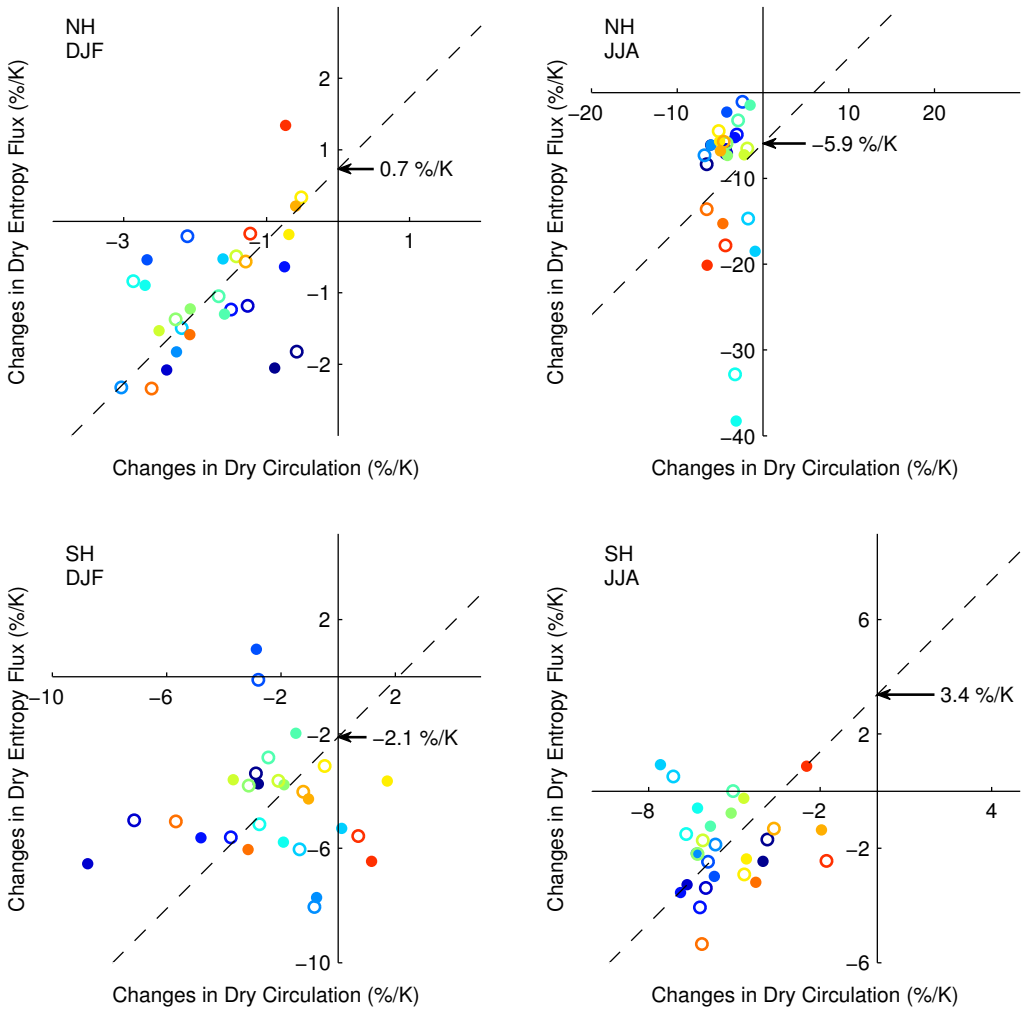

FIGURE 4.2. Relative changes in the dry transport. On the ordinate are plotted changes in fluxes while on the abscissa are plotted changes in circulations. On each graph, the arrow indicates the mean relative changes in stratification as defined by (4.7), which can be read off the intersection of the dashed line with the ordinate. Filled dots correspond to changes between 1961-2000 and 2046-2065 while empty dots correspond to changes between 1961-2000 and 2081-2100. See Table 4.2 for ensemble averages and standard deviations.

not only to an increase in the winter precipitation in the midlatitudes, but also to an increase in the amount of air that ascends within winter storms.

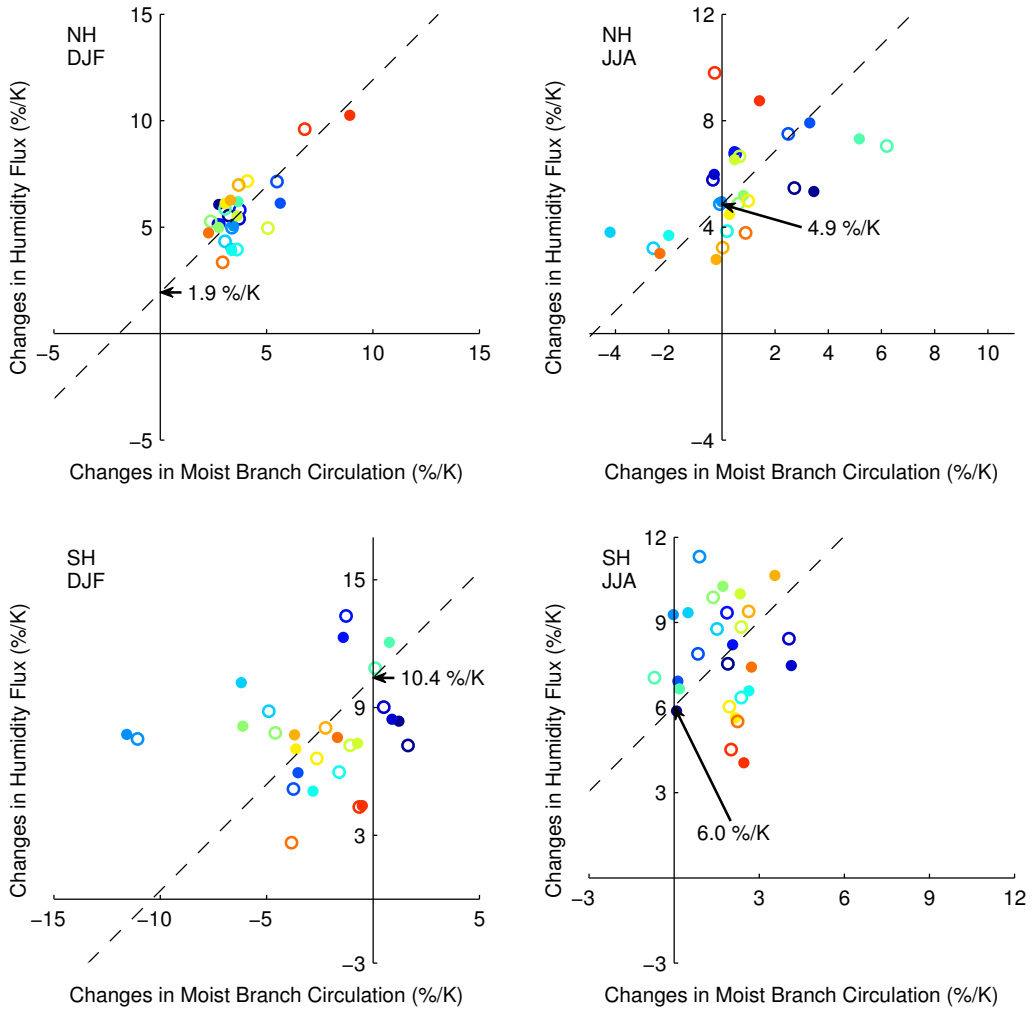

FIGURE 4.3. Relative changes in the moist branch transport. Same as in Figure 4.2 but for the moist branch transport. The stratification is defined by (4.8).

Figure 4.4 shows the changes in the MR moisture fluxes (4.10) versus the MR (4.9). Once more, the dashed line of slope unity gives the MR moist entropy stratification equation (4.11) at its intersection with the ordinate. The MR moisture fluxes differ from the total moisture fluxes of Figure 4.3 in

that they do not include transport of moisture taking place in the planetary boundary layer. For this reason, the MR moisture fluxes will not change in the same way as the total moisture fluxes. During NH DJF and SH JJA, both change in similar ways under climate change. During NH JJA and SH DJF however, the MR moisture fluxes are reduced while the total moisture fluxes increase. This means that, as the climate warms, the moisture fluxes associated with moist ascents in the MR increase only during the winter and not during the summer. During the summer, all of the increase in moisture fluxes take place in the planetary boundary layer.

The summer hemispheres both show a scatter about the origin, meaning weak changes in moisture fluxes (-1.2%/K NH and -0.7%/K SH), weak changes in mass fluxes (-1.0%/K NH and 0.3%/K SH) and weak change in stratification (-0.1%/K NH and -0.9%/K SH). All of these results fall within one standard deviation of the origin and as such do not indicate a clear trend. The winter hemispheres, on the other hand, exhibit robust changes. The MR increases by about 4%/K in both hemispheres and lie at more than two standard deviations of no changes. Associated with these increases in MR are strong increases in MR moisture fluxes of 8.6%/K NH and 4.6%/K, both results being as robust as the increase in MR. The increase in stratification is reliable in the northern winter at 4.3%/K$\pm$1.7%/K but is not during the southern winter with 0.7%/K$\pm$1.2%/K.

The southern winter increase in MR moisture fluxes is thus mostly caused by an increase in MR and not to an increase in the moisture difference across eddies. This is also the case in the NH JJA and SH DJF, the two summer hemispheres, where the increase in moisture stratification is very

close to 0%/K. This means that during NH JJA, SH DJF and SH JJA the difference of moisture between the poleward and the equatorward branch stays the same. Because in summer hemispheres the moisture transported by the MR does not increase, it implies that the MR is not strengthened. It therefore appears from this analysis that during the summer, there is not a substantial increase in mass flux associated with moist ascents.

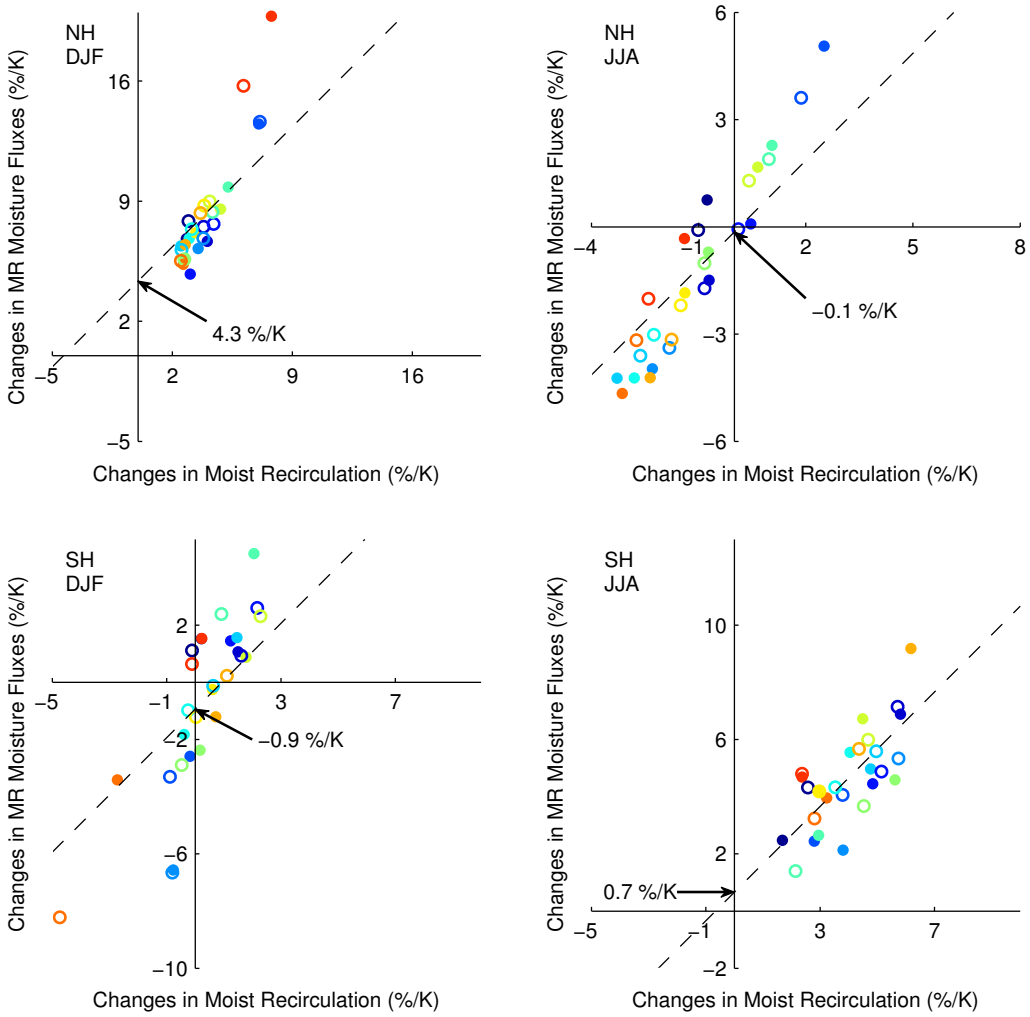

FIGURE 4.4. Relative changes in the MR. Same as in Figure 4.2 but for the MR.

In Figure 4.5, we plot changes in the moist entropy fluxes $\overline{F_{s_m}}$ versus

changes in $\overline{\Delta\Psi_m}$, the total mass transport on s_m. The change in total mass transport decreases for the Northern summer (by -1.0%/K) and for the Southern hemisphere (by -2.5%/K for DJF and -1.4%/K for JJA, respectively), but increases slightly during the northern winter (by 0.5%/K, with a standard deviation of 0.8%/K). The effective stratification increases in both hemispheres and both seasons with ensemble means ranging from 0.9%/K to 5.2%/K. The changes in total circulation are thus the result of the weakening of the dry circulation and the intensification, at least during the winter season, of the moist branch. The total circulation only increases during the Northern winter where the intensification of the moist branch more than compensate for the weakening of its dry branch.

4.3.2 Changes In Model Average

In this section, we apply the diagnostics of chapter 2 to the model average mass flux joint distribution (4.2). In light of the important scatter observed for the circulation indices, we do not necessarily expect the model average to accurately depicts changes in any given model. It can however provide us with an improved perspective on the meridional and vertical distribution of those changes, helping us in interpreting the observations made using the indices. In this section we compare the twentieth century 1961-2000 with the end of the twenty-first century 2081-2100. We also revert to using θ and θ_e instead of s_l and s_m. We are in fact still using s_l and s_m but

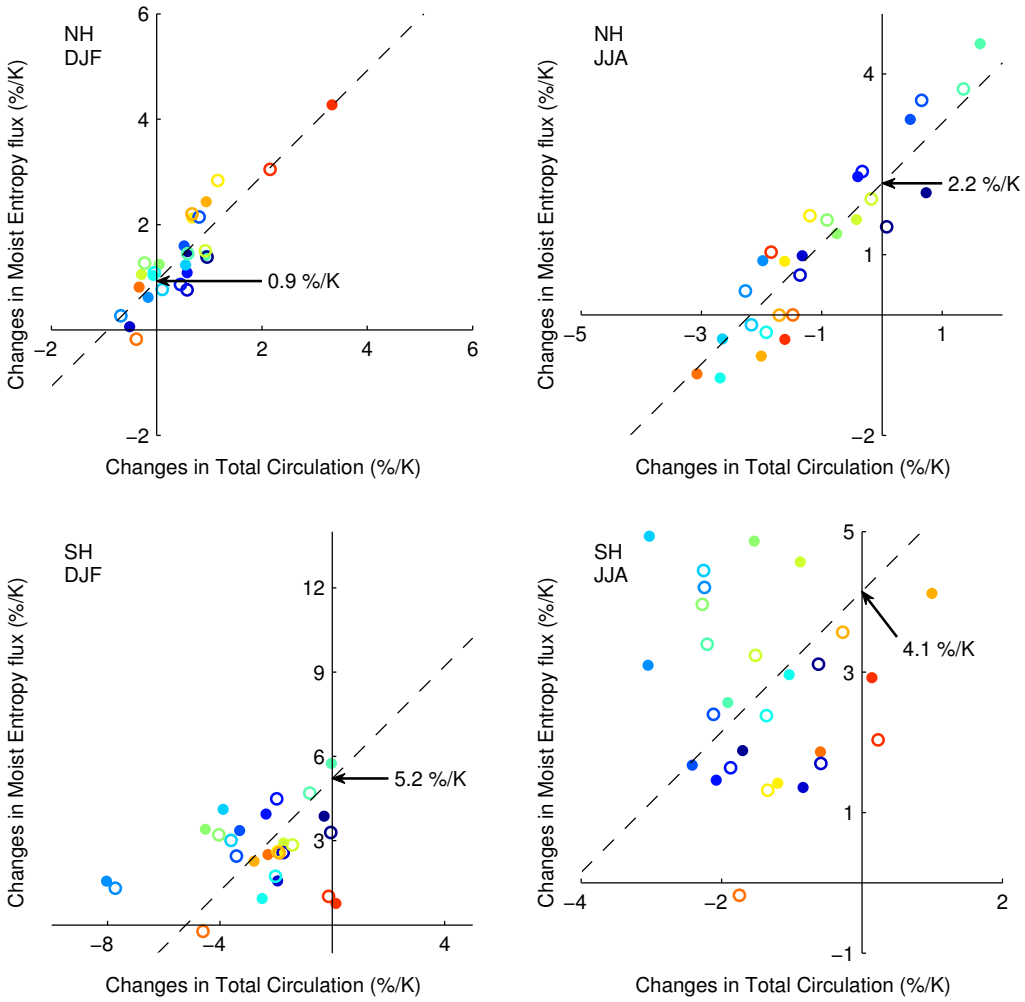

FIGURE 4.5. Relative changes in the total transport. Same as in Figure 4.2 but for the total transport.

we are converting them to θ and θ_e by using the approximations

$$\theta \approx T_0 e^{\frac{s_l}{c_{pd}}}, \tag{4.13}$$

$$\theta_e \approx T_0 e^{\frac{s_m}{c_{pd}}}, \tag{4.14}$$

which can be obtained[3] from equations (1.48) and (1.56). Using these coordinates allow us to compare our results with the theory in chapter 2 more effectively.

4.3.2.1 Circulations on Dry and Moist Isentropes

We begin by plotting changes in the circulations on dry and moist isentropes in Figure 4.6 and Figure 4.7, respectively. In both plots, black contours represent the twentieth century values. Solid contours are positive and dashed contours are positive, starting at 20 Sv in magnitude with 20 Sv increments. The color contours represent the changes between the last two decades of the 21$^{\text{st}}$ and the last four decades of the 20$^{\text{th}}$ century, sharing the same contour increments as the unfilled contours. Warm colors are positive and cold are negative. Without these changes, these figures correspond to Figure 2.2 and Figure 2.9 but using the model average joint distribution instead of the one recovered from the ERA40 dataset.

The dry circulations in Figure 4.6 depict most of the previous observations made using indices. The southern summer's circulation is weakened

[3] The approximation for θ is not completely right and could have been made more accurate if we had used $e_0 = e_s(T_0)$ instead of $e_0 = 10^5$Pa. The error has the effect of lifting the lower part of the circulation on dry isentropes by about 10K at the equator but much less in the midlatitudes. The approximation for θ_e does not depend on e_0 and is thus unaffected by this choice.

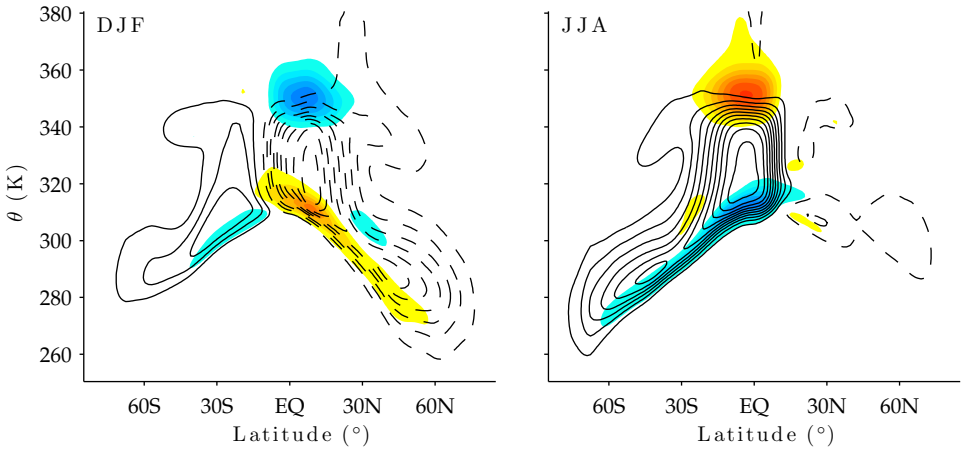

FIGURE 4.6. Twentieth century model-average dry Circulation and changes in the twenty-first century. The black contours correspond to the dry circulation for the 20^{th} century model average. The solid line are positive values and dashed lines are negative. The filled contour correspond to the changes between the 21^{st} and 20^{th}. The warm colors and positive and the cool colors are negative. Filled and unfilled contours start at 20 Sv with 20 Sv increments.

by the blue contour that touches the streamfunction's maximum value. No warm contours are visible, which confirms that the predominant change in the circulation is a weakening and not a translation to higher θ values. The northern summer is as pathological as previously described: it is weak and has little structure. While few changes are observable, some warm contours are noticeable and are in line with the previous untrustworthy observations using the circulation indices.

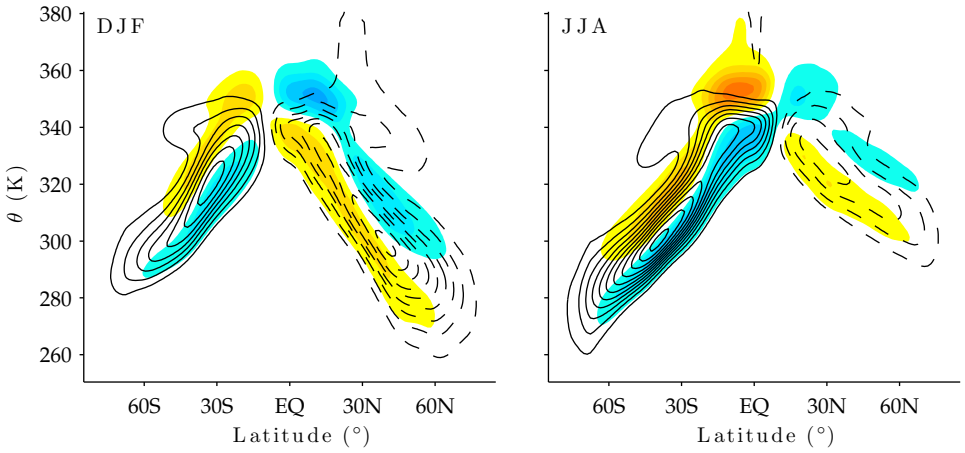

FIGURE 4.7. Twentieth century model-average moist circulation and changes in the twenty-first century. Same as Figure 4.6 but for the circulation on moist isentropes.

The winter circulations are elongated and translated towards higher θ in the subtropics, in accordance with earlier studies (eg Held and Soden, 2006) that focused on these regions. In both hemispheres, the winter circulation changes are very similar, with a weakening across the midlatitudes for low θ values and only some strengthening at around 30° latitude in the mid troposphere. The observed weakening has the effect of lifting the equatorward return flow of the circulation and thus reduces the dry entropy

flux. Because the changes should sum to zero at each latitude, the fact that only a weakening appears means that the strengthening is spread over a broad θ region. This would be consistent with an increase in the dry stratification identified using the circulation indices.

In Figure 4.7, we show a similar diagnostic but for the circulation on moist isentropes this time. In all seasons except the northern winter, a clear weakening affects the circulation's peak for most of the midlatitudes. It is accompanied by a strengthening at higher θ_e, which indicates a translation to higher θ_e values as well as a broadening of θ_e extent, in accordance with the systematic increase in stratification observed in the previous section for these regions. The northern winter circulation changes are similar but its peak value does not seem to be affected directly by a substantial weakening. This suggests the changes produces mostly a translation of the circulation towards higher θ_e values, with limited spreading and change in stratification. The northern winter moist circulation consequently appears to be neither strengthened nor weakened, which was already observed using the circulation indices.

4.3.2.2 Directional Mass Fluxes and their θ_e Profiles

These changes in the circulations on moist and dry isentropes can also be understood in terms of the directional mass fluxes presented in section 2.3. The advantage is that they allow us to recover in addition their directional θ_e profile, which indicates the stability properties of the motions. In the left and right panels of Figure 4.8 we show the Northward mass fluxes $\langle \rho v \rangle^+$ and the Southward mass fluxes $\langle \rho v \rangle^-$, respectively. The black contours are

used for the 20th century, solid for positive values and dashed for negative values. The color contours are used for the 21th century, green for positive values and orange for negative values. As observed using the circulations on dry isentropes, the most obvious changes occur in the subtropics with the poleward branch of the Hadley being lifted by approximately 10K. The NH JJA $\langle \rho v \rangle^+$ is lifted by a similar amount while its $\langle \rho v \rangle^-$ is lifted by a little less. Every other mass fluxes are lifted by less than 5°K, which compares to the 3°K to 4°K surface warming over the same period.

Beyond a translation towards higher θ values, the most notable effect of surface warming appears within the equatorward summer mass fluxes, namely in the NH JJA $\langle \rho v \rangle^-$ (lower right) and in the SH DJF $\langle \rho v \rangle^+$ (upper left). In both of these flows, the reduction in strength is clear with the highest contour level being substantially reduced in size or outright removed. Given the relative weakness of the circulation during the summer season, these changes can have a great impact on the MR strength. Understanding why these mass fluxes are reduced is the key to understanding the difference between summer eddies and winter eddies sensitivity.

To make some progress in that direction, we want to understand the thermodynamical structure of the flow. We plot in Figure 4.9a and Figure 4.9b the directional vertical profiles θ_e of chapter 2 for DJF and JJA, respectively. Thin black contours represent the 20th century MR and the thicker black lines indicate that century direction θ_e. The color contours indicate the 21st century MR, with the same color code as for Figure 4.8. The blue dashed lines show the 21st century directional θ_e curves. Note that some but not all of the changes for these curves is the result of the MR

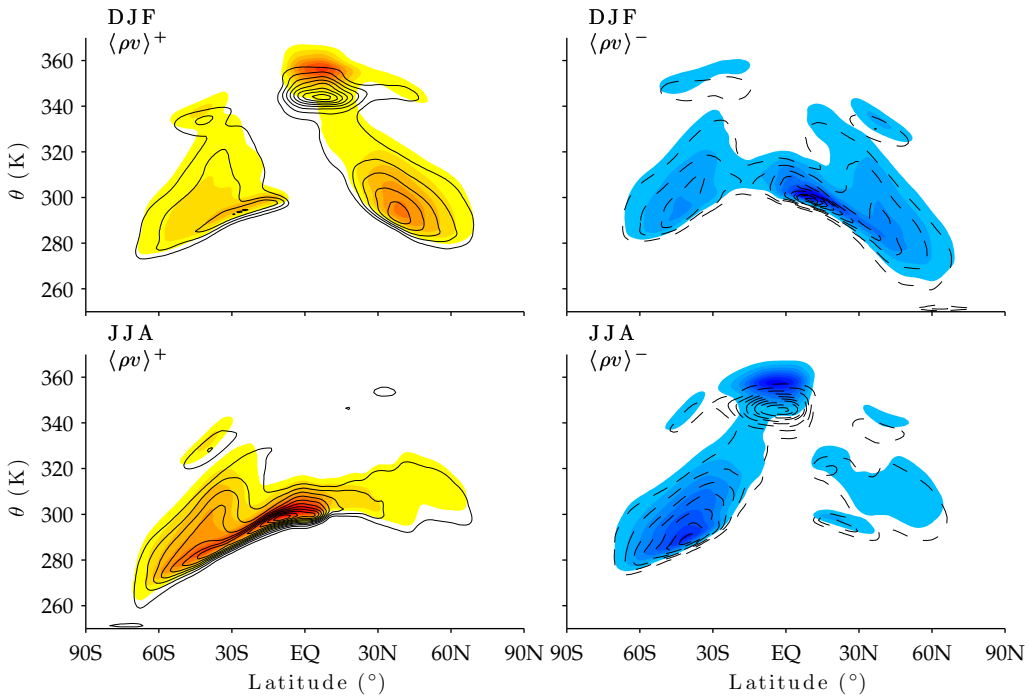

FIGURE 4.8. Changes in Directional Fluxes. The black contours correspond to mass fluxes for the 20th century model average. Solid contour are positive and dashed contours, negative. The filled contour correspond to the mass fluxes for the 21st century. The orange colors and positive and the green colors are negative. All contours start at 2 Sv/K with 2 Sv/K increments.

being lifted to higher θ values.

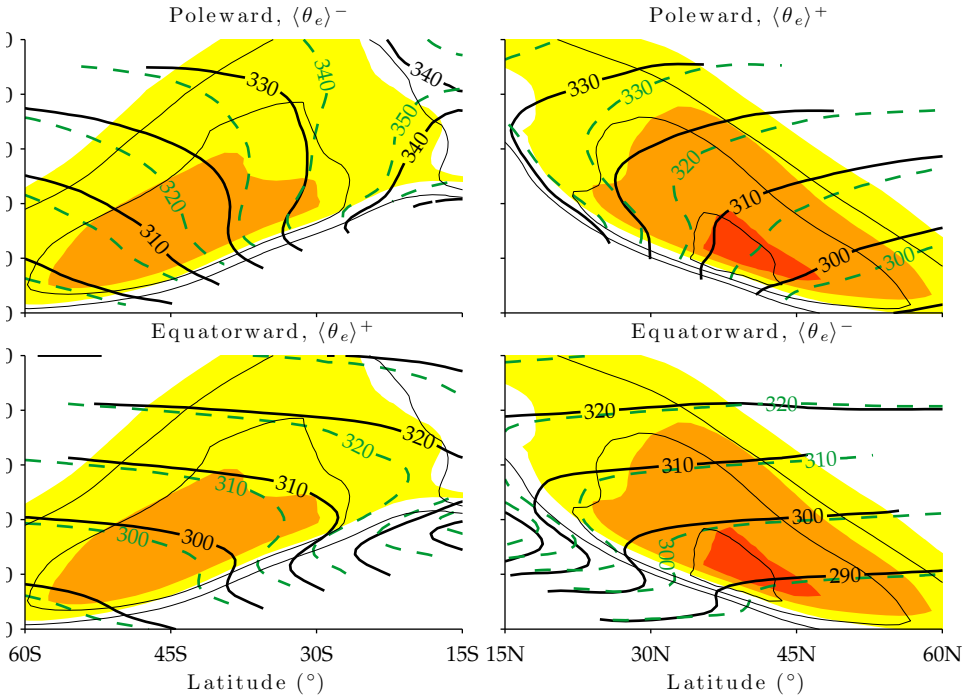

FIGURE 4.9A. DJF Changes in directional θ_e. We plot the MR using the same contours as in Figure 4.8. The directional θ_e for the 20th century are shown in labeled black contours. The directional θ_e for the 21st century are in dashed unlabeled blue lines and have the same value as the next labeled black contour above it.

The MR is indeed seen to be lifted to higher θ in all seasons but this translation appears to be the most important during the northern summer. During the summer seasons, the MR appears to be reduced while during the winter seasons the MR appears to be extended along the θ direction which suggests a strengthening of its total mass flux.

The poleward flows (upper panels of both figures) all exhibit an increase in their directional θ_e. This implies an increase in the poleward transport of θ_e by the poleward branch for both seasons and both hemispheres. As the surface temperatures increase, the surface θ_e increases exponentially

according to the CC scaling. This means that even thought the MRs are lifted to higher θ values, the θ_e in their poleward branch is carrying is even higher θ_e, resulting in an increase in moist entropy transport.

This brings an apparent paradox. It was observed in Figure 4.4 that a significant increase in the net transport of θ_e by the MR occurs only within the winter hemispheres, implying that the equatorward θ_e fluxes must compensate the poleward θ_e fluxes within the summer hemispheres. It can indeed be seen that near the base of the MR in the summer equatorward flows (lower left panel of Figure 4.9a and lower right panel of Figure 4.9b) there is a substantial increase in θ_e, unlike in the winter equatorward flows. Since the base of the eddies is the most intense, this small increase translates into an important cancellation in the net transport of θ_e by the MR. It thus appears that summer MR θ_e transport is reduced because too much of the increase in their poleward θ_e occurs at high θ.

The intriguing case of the northern summer displays once more its marked difference from the other hemipheres. One immediately notices how horizontal the lower part of its moist isentropes are. From what can be seen in Figure 4.9b, a surface parcel at 30°N in the 20$^{\text{th}}$ century will follow a dry isentrope until about 40°N, after which it will follow a moist $\langle\theta_e\rangle^+ = 320$K moist isentrope. A similar parcel in the 21$^{\text{st}}$ century will travel even farther north before it starts following its $\langle\theta_e\rangle^+ = 330$K moist isentrope. But moving along this curve, because of its "S" shape, would require a discontinuous path, a situation that we have associated with the need for the parcel to undergo a deep convective adjustment.

This poleward displacement of the "S" shaped moist isentrope seems to

also occur in the upper left panel of Figure 4.9a, which corresponds to the poleward θ_e in the southern summer. While it is ambiguous for the southern winter in the upper left panel of Figure 4.9b, it clearly does not happen during the northern winter (upper right panel of Figure 4.9a). This is yet another hint that the increase in surface moisture enhances the circulation only if it leads to predominantly slantwise convective motions.

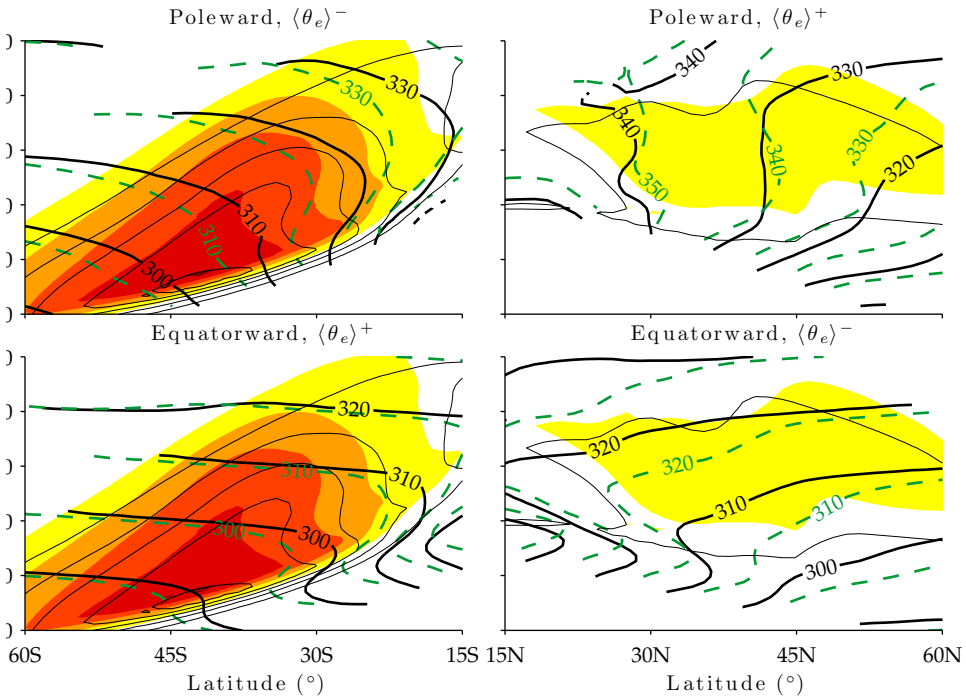

FIGURE 4.9B. JJA Changes in directional θ_e. Same as in Figure 4.9a.

4.4 Summary

We analyzed a subset of model outputs for the IPCC AR4 to identify changes in the midlatitude circulation. A set of indices has been introduced to characterize the mass and entropy transport by the dry and moist branch of the circulation separately, and to estimate how these would be affected by climate change over the next century. These diagnostics offer the advantage that they incorporate in a physically consistent manner the eddy transport into the overall circulation. This complements other studies such as Teng et al. (2008), Bengtsson et al. (2009) focused on changes in individual storms, by offering an integrated assessment of the changes over many storms.

In accordance with previous studies, we found that the mass transport by the dry branch weakens as temperatures increase. This behavior is qualitatively similar, although not as pronounced as the changes in the tropical Hadley circulation discussed in Held and Soden (2006). We also found that the mass transport by the moist branch circulation, identified as the difference between the circulation on moist and dry isentropes, intensifies during the winter months but not during the summer months. Physically, this can be interpreted as an increase in the mass of air ascending within midlatitude winter storms.

Our analysis also indicates that a weakening of the dry branch of the circulation can be in part balanced by a strengthening of the moist branch. As the dry circulation becomes inhibited by enhanced dry stratification and weaker Equator-to-Pole temperature gradients, the moist branch can become more active, thus extracting more moist air from the subtropical regions. This suggests that in a warmer planet, even as the atmosphere be-

comes more stable for dry baroclinic instability, moist processes play a more significant role in the maintenance of the stormtracks. Understanding the exact nature of this compensation between the dry and moist branches remains an open question that is central to our ability to predict the evolution of midlatitudes climate over the next century.

To begin answering this question, we have used the model-averaged mass flux joint distribution to apply the concepts developed in chapter 2. This simplification allowed us to gain a sense of vertical and meridional distribution of changes responsible for the evolution of circulation indices. The analysis of changes in the circulation on dry isentropes between the twentieth and the twenty-first century showed that most changes occurred in the subtropics and in the midlatitudes equatorward flow.

Changes in the circulation on moist isentropes are more widespread and generally correspond to a simple translation to higher θ_e values. This is not surprising considering that the circulation peaks at the median θ_e surface value (see section 2.5). Also, the total circulation indices in Figure 4.5 tend to predict the strengthening and weakening behavior of the model average's circulations on moist isentropes. Similarly, the fact that changes are uniform across midlatitudes reinforces the relevance of the latitude-averaged indices.

To understand changes in the moist branch circulation, we made use of the directional θ_e in relation to the moist recirculation. As increasingly moist air is extracted from the low midlatitudes, the poleward θ_e increases accordingly. In the summer hemispheres, however, this is not sufficient to increase the net meridional transport of θ_e. This moister air changes the

stability of the poleward moving air, making it more convectively unstable, which sends higher θ_e air to higher vertical levels quicker, where the moist recirculation is not as strong. Because the equatorward θ_e is increasing slightly in the lower part of the moist recirculation where it is the strongest, the small increase amounts to important equatorward transports of θ_e, thus mitigating the increase in the poleward moist recirculation branch.

Chapter 5

Conclusion

5.1 Discussion

The main result of this thesis could almost be summarized with only two figures: Figure 2.8 and Figure 2.13. Both of these figures relate the θ_e climatology on dry isentropes to the directional profiles obtained from the mass flux joint distribution. In Figure 2.8, it is shown that an average of the two directional θ_e profiles is equivalent to the mean θ_e profile. Because directional θ_e profiles represent two opposites states of the atmosphere it was concluded that the midlatitudes climate should not be construed as a mean state onto which turbulent disturbances evolved. Instead, we argued that the midlatitudes climate should be pictured as being only populated by those disturbances and that the mean state does not reflect a typical atmospheric state.

This argument was further strengthened with the help of Figure 2.13, a figure that compares the difference between the two directional θ_e profiles

and the standard deviation of θ_e on dry isentropes. The impressive relationship between the two — almost everywhere in midlatitudes, the two directional profiles are separated by 2.2 to 2.6 times the standard deviation — indicates that these directional fluxes occur at extremal values of the θ_e distribution. From these two figures, one must conclude that midlatitudes turbulent disturbances are *1*) larges variations that occurs far away from the mean state, and *2*) that mean state is an average of disturbances, not a typical atmospheric state. This observation should however come with one caveat. While we are effectively arguing that eddies should not be seen as weak turbulence that enhances diffusion but rather strong large-variation features, this applies *only* to the moist effectively stability as felt by the different branch of the midlatitudes circulation. Therefore, we are not ruling out the possibility that other features of this circulation can indeed be considered weak and acting in a diffusive way (see Hwang and Frierson, 2010, for a recent example).

These observations form one basis of this thesis and are fundamental to appreciate many of the results we have presented. In particular, they permitted the development of a simple moist theory of the low-level flow in section 2.5 which served to explain Figure 2.12, a typical mass flux joint distribution that exhibit a clear distinction between the poleward and equatorward flows. They also allowed the interpretation that linked the moist recirculation and the EKE through moist ascents along the poleward moist isentrope alone in Figure 3.16. This interpretation was made possible because we knew that the two directional flows had drastically different moisture contents and that therefore the latent heat release effects could be

diagnosed from a poleward directional θ_e profile.

In addition, this perspective confirmed that we should resort to techniques that can account for large variations if we want to quantify the midlatitudes overturning circulation. This means that any technique that fundamentally assumes a weak interaction of turbulence and mean state, like for instance TEM, should only used with circumspection. As a consequence and based on the new diagnostics described in this thesis, we suggest that one should use techniques that can account for at least some of the large variability in moist effects within midlatitudes disturbances. That does not rule out approximate techniques based on climatological statistics as in Pauluis et al. (2010b).

This argument is one of the reason why we have used the moist circulation as a diagnostic for climate changes in midlatitudes. By using the moist circulation, we ensured that increases in θ_e variability were properly incorporated in our analysis. By showing in section 2.4 that the moist circulation could be understood in terms of directional fluxes and directional θ_e profiles, we have provided a canonical decomposition of the effects of global warming. The theoretical model of section 2.5 showed that the poleward θ_e profile depended on both the mean surface temperature and its zonal variance. Because the poleward θ_e profile also determines the moist circulation effective stratification, we know that increases in stratification depicted by Figure 4.5 are in fact directly related to an increase in surface temperature statistics.

But that was not the sole focus of chapter 4. Our goal was to use the joint isentropic analysis to quantify how midlatitudes eddies were changing with

global warming. To do so, we used our results of chapter 3 to deduce the impact of increased surface moisture on the dynamics and on the induced isentropic circulations of idealized baroclinic eddies. Because our results confirmed the hypothesis about the role of moist baroclinic eddies stated in chapter 2, we were able to relate eddies moist isentropic motions with their dynamics. In particular, we were able to demonstrate a strong correlation between widespread slantwise convection, moist recirculation equatorward of the jet and eddy kinetic energy at higher latitudes.

In the same chapter, we verified that for a moist baroclinic eddy in isolation the bulk moist recirculation could be inferred by the difference between the moist and the dry circulation, also called the moist branch in chapter 4. This correspondence did not come as a surprise since we already knew that by folding the directional fluxes we could recover the moist circulation. And since the added moist circulation transport has to come from the directional fluxes, it has to be found within the cancelled portions that otherwise disappear in the dry circulation. This meant that the moist branch of the circulation was conceptually similar to the moist recirculation.

This constituted the missing link. The mass fluxes captured by the moist circulation but not by the dry circulation are thus related to the moist recirculation. This moist recirculation and the EKE at high latitudes were shown in chapter 3 to be connected by slantwise convection along the lines of constant θ_e in the poleward profile. The more vigorous the recirculation, the more moist air is transported poleward, a transport that occurs along poleward moist isentropes. As they follow a slanted path, they

provoke diabatic disturbances in potential vorticity dynamics that enhance the baroclinic wave strength and result in a stronger long wave breaking.

In the context of the analysis ofchapter 4, we observed a robust increase in the moist branch circulation for the winter hemispheres only. With the support of the preceding arguments, we concluded that within the winter hemispheres the strength of individual eddies as measured by their eddy kinetic energy will increase due to a lower moist stratification of the poleward component. This is why we could predict that winter storms triggered by baroclinic instability should strengthen with global warming. This simple result exposes the power of using the full mass flux joint distribution to quantify the midlatitudes climatology.

5.2 Future Work

The theory developed in chapter 2, by requiring the full joint distribution, makes it an unlikely candidate for widespread use. This is why it would be important to devise an computational technique that could forego the requirement of daily data processing and manage to recover an approximate joint distribution by using monthly eddy statistics. Such computational techniques have been developed for the dry and moist circulations by Pauluis et al. (2010b) but it remains unclear if use a similar approach to approximate accurately the full joint distribution. Until such an approximate solution is found, it is expected that the theory and most of the discussion in this thesis will rarely be used for casual climatological diagnostics.

The moist life-cycles in chapter 3 were mostly studied in terms of their induced isentropic circulations and their signature within those isentropic analyses. While these methods assume that they are tracking parcels due to their semi-lagrangian coordinates, it would be relevant to exploit the high resolution available in such controlled experiments to track air masses and to actually observe how motions change due to the input of moisture. This study would provide a natural moist extension to a similar dry studies (Polvani and Esler, 2007, for example).

The climate change study in chapter 4 offers even more opportunities for future work. For example, our hemisphere-averaged diagnostics showed a large spread among models, a spread that manifests itself as important disparities in the isentropic circulations of different models. Understanding these disparities would improve our understanding of thermodynamical

biases created by various physical parametrization. In turn this could impact how we interpret the outputs of GCMs used for global warming studies.

A fundamental observation of this work is the direct relationship between surface temperature, surface moisture and the poleward θ_e. In a warming climate, it is expected that both the surface temperature and the surface moisture content will change depending on land/sea exchange properties. Because these changes will prescribe a new poleward θ_e profiles, the surface processes are expected to influence greatly midlatitudes eddies characteristics. Understanding the interactions between the two could potentially explain why in global warming simulations summer hemispheres have a reduced moist branch while the winter hemispheres have a strengthened moist branch. This question is of fundamental importance since it concerns extreme weather patterns that are related to activity within the stormtracks. Stronger storms, we all know, can have a profound impact on a wide range of policy decisions ranging from building code to water management. A proper understanding of climate extremes along with a reasonable estimate of sea level rise are the two most critical problems in climate changes for which no simple answer exists.

Appendices

Appendix A

Computing the Joint Distribution

Interpolating to θ surfaces

The transformation of a flow from pressure coordinates — a true vertical coordinate — to surfaces of constant potential temperature θ — a pseudo-vertical coordinate — is a well-documented procedure. We refer the reader to Johnson (1989) for an extensive description. It relies on the fact that θ is mostly stratified so that the transformation $p \to \theta$ is well-defined in the zonal mean. As we would like to accomplish this transformation before taking a zonal mean for reasons that will become clear later, this is insufficient. To circumvent issues related to the overturning of isentropic surfaces, we define the transformation onto isentropic surfaces the following way:

$$\rho_\theta(\lambda, \phi, \theta, t) = \int_0^{p_s} \delta(\theta - \theta(\lambda, \phi, p, t)) \frac{dp}{g}, \tag{A.1a}$$

$$v_\theta(\lambda, \phi, \theta, t) = \frac{1}{\rho_\theta} \int_0^{p_s} v\delta(\theta - \theta(\lambda, \phi, p, t)) \frac{dp}{g}, \tag{A.1b}$$

$$q_{T\theta}(\lambda, \phi, \theta, t) = \frac{1}{\rho_\theta} \int_0^{p_s} q_T\delta(\theta - \theta(\lambda, \phi, p, t)) \frac{dp}{g}. \tag{A.1c}$$

We would like to avoid discarding the zonal variations in moisture and, instead of taking a zonal average, we undertake a similar procedure as in (A.1) but with θ_e. In order to do this, we have to recover the pressure assume that the atmosphere is stratified. This is done by defining:

$$p_\theta(\lambda, \phi, \theta, t) := g \int_\theta^\infty \rho_\theta(\lambda, \phi, \theta', t) d\theta', \tag{A.2}$$

which then allows us to recover the temperature on θ surfaces by inverting $\theta = \theta(T_\theta, p_\theta, q_{T\theta})$ for $T_\theta(\lambda, \phi, \theta, t)$. Finally, we can recover the equivalent potential temperature $\theta_{e\theta} = \theta_e(T_\theta, p_\theta, q_{T\theta})$.

Using this quantity, one can transform the zonal direction into a θ_e axis and take a time average:

$$M(\phi, \theta, \theta_e) = \left\langle \rho_\theta v_\theta \delta(\theta_e - \theta_{e\theta}(\lambda, \phi, \theta, t)) \right\rangle . \tag{A.3}$$

If the flow is always stably stratified, (A.3) can be rewritten as

$$M(\phi, \theta, \theta_e) = \left[\int_0^{p_s} v \delta(\theta_e - \theta_e(\lambda, \phi, p, t)) \delta(\theta - \theta(\lambda, \phi, p, t)) \frac{dp}{g} \right], \tag{A.4}$$

which is the form found in Pauluis et al. (2010a). This discussion interprets the joint distribution as a way to retain the latent heat fluctuations within the zonal mean.

Computational Methods

The mass flux is computed on a grid indexed by k in the vertical on which the meridional velocity v_k, the potential temperature θ_k, the equivalent potential temperature θ_{ek} and the layer pressure difference Δp_k are defined. The δ functions are converted to their discrete equivalents as presented in section 5.2:

$$M(\phi, \theta', \theta'_e) = 2\pi a \cos\phi \left[\sum_{k=1}^{N_{\text{lev}}} v_k(\phi, \lambda, t) \delta_{\Delta\theta}(\theta_k - \theta') \delta_{\Delta\theta_e}(\theta_{ek} - \theta'_e) \frac{\Delta p_k}{g} \right],$$

where N_{lev} is the number of vertical levels and $\Delta\theta$, $\Delta\theta_e$ are the phase-space grid spacing.

The discrete δ function guarantees that the approximate joint distribution preserves the exact joint distribution's first moment:

$$\sum_{\theta'} \sum_{\theta'_e} \theta' M(\phi, \theta', \theta'_e) \Delta\theta \Delta\theta_e = 2\pi a \cos\phi \left[\sum_{k=1}^{N_{\text{lev}}} \theta_k v_k(\phi, \lambda, t) \frac{\Delta p_k}{g} \right],$$

and similarly if we replace θ' by θ'_e in front of M and θ_k by θ_{ek} in front of v_k. The index k in this expression refers to the interpolated vertical levels. This numerical representation ensures that the resulting joint distribution accurately captures the fluxes. The exact definition of the discrete δ function is provided in the next section.

In chapter 2 and chapter 3, we have used a uniform target grid (θ', θ'_e) spacing corresponding to $\Delta\theta = \Delta\theta_e = 1\text{K}$. The grid was restricted to $250\text{K} \leq \theta', \theta'_e \leq 379\text{K}$, yielding a 130×130 thermodynamic phase-space for each latitude. In chapter 4, we have have substituted s_l for θ and s_m for θ_e

and have used a uniform target grid (s'_l, s'_m), on a 130×130 rectilinear grid $c_{pd} \ln \frac{250K}{T_0} \leq (s'_l, s'_m) \leq c_{pd} \ln \frac{380K}{T_0}$. The resulting grid has an approximately 1K in grid spacing in each direction.

The Discrete δ-function

In this work, we use two different formulations of the discrete δ function, both having very similar properties. They both specify a function $\phi(r)$ that reproduces some of the properties of the δ function. Once this function is chosen, one can define the discrete δ function as:

$$\delta_{\Delta\theta}(\theta_k - \theta') = \frac{1}{\Delta\theta}\phi\left(\frac{1}{\Delta\theta}(\theta_k - \theta')\right). \tag{A.5}$$

The Roma et al. (1999) version For chapter 2 and 3 we use a 3-points variant presented by Roma et al. (1999) in the description of the immersed boundary method. It is defined with the help of a function $\phi(r)$ with the following properties:

$$\phi(r) \text{ is continuous for all } r, \tag{A.6a}$$

$$\phi(r) = 0, \quad \text{for } |r| \geq 1.5, \tag{A.6b}$$

$$\sum_j \phi(r - j) = 1 \text{ for all } r, \tag{A.6c}$$

$$\sum_j (r - j)\phi(r - j) = 0 \text{ for all } r, \tag{A.6d}$$

$$\sum_j (\phi(r - j))^2 = C \text{ for all } r. \tag{A.6e}$$

where the sum is always over integers j and C is independent of r. The third property guarantees that its sum over integers is 1 while the fourth property guarantees that its first moment is conserved. The fifth property is mainly in there for numerical integration stability. Note that this will yield a δ function that has a length 3 stencil in the thermodynamic phase-space.

It can be shown that there exists a unique such function:

$$\phi(r) = \begin{cases} \frac{1}{6}\left(5 - 3|r| - \sqrt{1 - 3(1-|r|)^2}\right), & 0.5 \leq |r| \leq 1.5, \\ \frac{1}{3}\left(1 + \sqrt{1 - 3|r|^2}\right), & |r| < 0.5, \\ 0, & \text{otherwise.} \end{cases} \tag{A.7}$$

The Peskin (2002) version In chapter 4, we use the 4-points variant presented by Peskin (2002). Similarly, one tries to find a function $\phi(r)$ with the following properties:

$$\phi(r) \text{ is continuous for all } r, \tag{A.8a}$$

$$\phi(r) = 0, \quad \text{for } |r| \geq 2, \tag{A.8b}$$

$$\sum_{j \text{ even}} \phi(r-j) = \sum_{j \text{ odd}} \phi(r-j) = \frac{1}{2} \text{ for all } r, \tag{A.8c}$$

$$\sum_j (r-j)\phi(r-j) = 0 \text{ for all } r, \tag{A.8d}$$

$$\sum_j (\phi(r-j))^2 = C \text{ for all } r. \tag{A.8e}$$

where the sum is always over integers j and C is independent of r.

The third property guarantees that its sum over integers is 1 while the fourth property guarantees that its first moment is conserved. Splitting

the sum in the third property is important when used in conjunction with finite difference numerical schemes The fifth property is mainly in there for numerical integration stability. Note that this will yield a δ function that has a length 4 stencil in the thermodynamic phase-space.

It can be shown that there exists a unique such function:

$$\phi(r) = \begin{cases} \frac{1}{8}\left(5 - 2|r| - \sqrt{-7 + 12|r| - 4|r|^2}\right), & 1 \leq |r| \leq 2, \\ \frac{1}{8}\left(3 - 2|r| + \sqrt{1 + 4|r| + 4|r|^2}\right), & |r| < 1, \\ 0, & \text{otherwise.} \end{cases} \tag{A.9}$$

Appendix B

Baroclinic Initialization

Given the zonal velocity profile (3.6) and the relative humidity profile (3.8), one initialize a balanced flow with an extension of the procedure presented in Polvani and Esler (2007) for a dry model. Polvani and Esler used their initialization method over that discussed in Hoskins and Simmons (1975) for its ease of portability to models with different underlying numerical schemes. Here, we adopt the same approach and strive to make our experiments as reproducible as possible.

Virtual Temperature Profile

Given a zonal flow, one can use the meridional momentum balance in pressure coordinates

$$-\partial_\phi \Phi = (af + u\tan\phi)u, \tag{B.1}$$

and integrate it along pressure surface to recover the geopotential, Φ,

$$\Phi(p,\phi) = \Phi_r(p) - \int_0^\phi (af + u\tan\phi)u\, d\phi', \tag{B.2}$$

up to a reference geopotential profile $\Phi_r(p)$. This reference profile represents the geopotential at the equator. It can alternatively be specified as a virtual temperature reference profile, T_{vr}, thanks to the hydrostatic equation $\partial_{\ln p}\Phi_r = R_d T_{vr}$. Differentiating equation (B.2) by $\ln p$, we can recover the balanced virtual temperature T_v in terms of the reference T_{vr}:

$$T_v(p,\phi) = T_{vr}(p) - \frac{1}{R_d}\int_0^\phi (af + 2u\tan\phi)\partial_{\ln p}u\, d\phi'. \tag{B.3}$$

For a dry system, the virtual temperature is equal to temperature and equation (B.3) reduces to the balanced temperature profile of Polvani and Esler. Since we will only consider balanced states containing no condensate, the initial virtual temperature will correspond to the density temperature; there is thus no ambiguity as to which one of the two should be appropriate.

Reference Temperature Profile

Unlike in Polvani and Esler (2007), where the temperature profile was chosen to be a smoothed piecewise linear function, here we will define the reference profile to be the equatorial surface moist adiabat with temperature $T_0 = 300°\mathrm{K}$ and surface saturated specific humidity

$$q_{T0} = \frac{R_d e^*(T_0)}{R_v p_0 - \epsilon R_d e^*(T_0)}. \tag{B.4}$$

The surface moist entropy can thus be computed by using equation (1.51):

$$s_{m0} = s_m(p_0, T_0, q_{T0}) \tag{B.5}$$

and the moist adiabat, our reference profile, will be recoverable by inverting

$$s_{m0} = s_m(p, T_a(p), q_{T0}), \tag{B.6}$$

which can be done to high accuracy using Newton's method. In order to have a tropopause, we combine the moist adiabatic reference profile with the simple reference profile in Polvani and Esler (2007),

$$T_r(p) = \max\left\{T_0 + \frac{\Gamma_0}{(z_T^{-\alpha} + z^{-\alpha})^{1/\alpha}}, T_a(p)\right\}. \tag{B.7}$$

One can then compute water vapor profile $q_{vr}(p)$ corresponding to the reference temperature and the reference relative humidity at the equator:

$$q_{vr}(p) = \frac{R_d \mathcal{H}(p) e^*(T_r(p))}{R_v p - \epsilon R_d \mathcal{H}(p) e^*(T_r(p))}, \tag{B.8}$$

which allows to recover the equatorial virtual temperature profile $T_{vr}(p) = (1 + \epsilon q_{vr}(p))T_r(p)$ that enters in equation B.3.

This profile almost guarantees that no CAPE exists at the equator, no matter the relative humidity. It is only almost because a parcel lifted adiabatically will usually have a profile of water vapor that is strictly larger than (B.8). This means that if we initialize a flow with a surface equatorial relative humidity too close to 100%, some CAPE could appear. This is the

reason why we did not conduct experiments with relative humidity above 80%.

Meridional Temperature Profile

With a specified temperature reference profile equation (B.3) provides a balanced meridional virtual temperature that cannot be inputed directly in an atmospheric model. Instead, one has to recover the corresponding meridional temperature profile and the corresponding specific water content profile. Since humidity is specified as a distribution of relative humidity $\mathcal{H}(p)$, it complicates the recovery of T from T_v and $\mathcal{H}$. Using the CC equation, we must solve the following non-linear equation:

$$\begin{aligned} q_T(\phi, p) &= \frac{R_d \mathcal{H}(p) e^*\left(T(\phi, p)\right)}{R_v p - \epsilon R_d \mathcal{H}(\phi, p) e^*\left(T(\phi, p)\right)}, \\ T(\phi, p) &= \frac{T_v(\phi, p)}{1 + \epsilon q_T(\phi, p)}, \end{aligned} \tag{B.9}$$

a system that is easily inverted for $q_T(p, \phi)$ and $T(\phi, p)$ given a relative humidity profile $\mathcal{H}(\phi, p)$ and the virtual temperature profile (B.3). The inversion was done by a simple fixed-point iteration that is made efficient thanks to the relative smallness of ϵ. This makes the setup for the moist problem of similar complexity and with the same portability as the dry balanced flow.

Initial Perturbation

If we were to leave the initial conditions in this state, it would take a long time before enough numerical errors destabilize the balanced initial flow. One option is to perturb the solution along the most unstable mode (Simmons and Hoskins, 1977) but this proves to be cumbersome and difficult to reproduce. Instead, we once more follow Polvani and Esler (2007) and add to the initial temperature field a small perturbation T':

$$T'(\lambda, \phi) = \hat{T} \cos(m\lambda) \text{sech}^2 \left(m \left(\phi - \hat{\phi} \right) \right), \tag{B.10}$$

where λ is the longitude and all other parameters can be found in Table 3.3. This perturbation was not balanced as it is assumed (Polvani et al., 2004; Polvani and Esler, 2007) that the most unstable will be excited by the perturbation.

Bibliography

Andrews, D. and McIntyre, M. (1976). Planetary waves in horizontal and vertical shear: The generalized eliassen-palm relation and the mean zonal acceleration. *J. Atmos. Sci.*, 33(11):2031–2048.

Andrews, D. and McIntyre, M. (1978). Generalized eliassen-palm and charney-drazin theorems for waves oin axismmetric mean flows in compressible atmospheres. *J. Atmos. Sci.*, 35(2):175–185.

Bengtsson, L., Hodges, K., and Keenlyside, N. (2009). Will extratropical storms intensify in a warmer climate? *J. Clim.*, 22(9):2276–2301.

Bengtsson, L., Hodges, K., and Roeckner, E. (2006). Storm tracks and climate change. *J. Clim.*, 19(15):3518–3543.

Bjerknes, J. and Solberg, H. (1922). Life cycle of cyclones and the polar front theory of atmospheric circulation. *Geof. Publ.*, 3(1):18.

Charney, J. (1947). The dynamics of long waves in a baroclinic westerly current. *J. Meteorology*, 4(5):136–162.

Chou, C. and Chen, C.-A. (2010). Depth of convection and the weakening of tropical circulation in global warming. *J. Clim.*, 23(11):3019–3030.

Czaja, A. and Marshall, J. (2006). The partitioning of poleward heat transport between the atmosphere and ocean. *J. Atmos. Sci.*, 63(5):1498–1511.

Durran, D. R. (1999). *Numerical Methods for Wave Equations in Geophysical Fluid Dynamics*. Springer-Verlag.

Eady, E. (1949). Long waves and cyclone waves. *Tellus*, 1(3):33–52.

Eady, E. (1950). The cause of the general circulation of the atmosphere. *Centen. Proc. Roy. Meteor. Soc*, pages 156–172.

Eliassen, A. and Palm, E. (1961). On the transfer of energy in stationary mountain waves. *Geofys. Publ.*, 22(3):1–23.

Emanuel, K. (1983). The lagrangian parcel dynamics of moist symmetric instability. *J. Atmos. Sci.*, 40(10):2368–2376.

Emanuel, K. (1994). *Atmospheric convection*. Oxford University Press.

Fantini, M. (1999). Linear evolution of baroclinic waves in saturated air. *Quart. J. Roy. Meteor. Soc.*, 125(555):905–923.

Fantini, M. (2004). Baroclinic instability of a zero-pve jet: Enhanced effects of moisture on the life cycle of midlatitude cyclones. *J. Atmos. Sci.*, 61(11):1296–1307.

Ferrel, W. (1856). An essay on the winds and the currents of the oceans. *Nashville Journal of Medicine and Surgery*, 11(4):7–19.

Frierson, D. (2006). Robust increases in midlatitude static stability in simulations of global warming. *Geophys. Res. Lett.*, 33(24):L24816.

Frierson, D. (2008). Midlatitude static stability in simple and comprehensive general circulation models. *J. Atmos. Sci.*, 65(3):1049–1062.

Frierson, D., Held, I., and Zurita-Gotor, P. (2006). A gray-radiation aquaplanet moist gcm. part i: Static stability and eddy scale. *J. Atmos. Sci.*, 63(10):2548–2566.

Gutowski, W., Branscome, L., and Stewart, D. (1992). Life cycles of moist baroclinic eddies. *J. Atmos. Sci.*, 49(4):306–319.

Hadley, G. (1735). Concerning the cause of the general trade winds. *Philosophical Transactions of the Royal Society*, 34:58–62.

Held, I. and Schneider, T. (1999). The surface branch of the zonally averaged mass transport circulation in the troposphere. *J. Atmos. Sci.*, 56(11):1688–1697.

Held, I. and Soden, B. (2006). Robust responses of the hydrological cycle to global warming. *J. Clim.*, 19(21):5686–5699.

Hoskins, B. and Simmons, A. (1975). A multi-layer spectral model and the semi-implicit method. *Quart. J. Roy. Meteor. Soc.*

Hwang, Y. and Frierson, D. (2010). Increasing atmospheric poleward energy transport with global warming. *Geophys. Res. Lett.* in press.

Johnson, D. (1989). The forcing and maintenance of global monsoonal circulations: An isentropic analysis. In *Adv. Geophys.*, volume 31, pages 43 – 316. Elsevier.

Juckes, M. (2000). The static stability of the midlatitude troposphere: The relevance of moisture. *J. Atmos. Sci.*, 57(18):3050–3057.

Karoly, D., McIntosh, P., Berrisford, P., McDougall, T., and Hirst, A. (1997). Similarities of the deacon cell in the southern ocean and ferrel cells in the atmosphere. *Quart. J. Roy. Meteor. Soc.*, 123(538):519–526.

Korty, R. and Schneider, T. (2007). A climatology of the tropospheric thermal stratification using saturation potential vorticity. *J. Clim.*, 20(24):5977–5991.

Laliberté, F. and Pauluis, O. (2010). Winter intensification of the moist branch of the circulation in simulations of 21st century climate. *Geophys. Res. Lett.*, 37(20):L20707. Copyright 2010 American Geophysical Union.

Lin, S.-J. and Pierrehumbert, R. (1988). Does ekman friction suppress baroclinic instability? *J. Atmos. Sci.*, 45(20):2920–2933.

Lin, S.-J. and Pierrehumbert, R. (1993). Is the midlatitude zonal flow absolutely unstable? *J. Atmos. Sci.*, 50(4):505–517.

Lindzen, R. and Fox-Rabinovitz, M. (1989). Consistent vertical and horizontal resolution. *Mon. Wea. Rev.*, 117(11):2575–2583.

McIntosh, P. and McDougall, T. (1996). Isopycnal averaging and the residual mean circulation. *J. Phys. Oceanogr.*, 26(8):1655–1660.

Meehl, G., Covey, C., Taylor, K., Delworth, T., Stouffer, R., Latif, M., McAvaney, B., and Mitchell, J. (2007). The wcrp cmip3 multimodel dataset: A

new era in climate change research. *Bull. Amer. Meteor. Soc.*, 88(9):1383–1394.

Mitas, C. and Clement, A. (2006). Recent behavior of the hadley cell and tropical thermodynamics in climate models and reanalyses. *Geophys. Res. Lett.*, 33(1):L01810.

Montgomery, M. and Farrell, B. (1991). Moist surface frontogenesis associated with interior potential vorticity anomalies in a semigeostrophic model. *J. Atmos. Sci.*, 48(2):343–368.

Moore, R. and Montgomery, M. (2005). Analysis of an idealized, three-dimensional diabatic rossby vortex: A coherent structure of the moist baroclinic atmosphere. *J. Atmos. Sci.*, 62(8):2703–2725.

O'Gorman, P. and Schneider, T. (2008). Energy of midlatitude transient eddies in idealized simulations of changed climates. *J. Clim.*, 21(22):5797–5806.

Parker, D. and Thorpe, A. (1995). Conditional convective heating in a baroclinic atmosphere: A model of convective frontogenesis. *J. Atmos. Sci.*, 52(10):1699–1711.

Pauluis, O., Czaja, A., and Korty, R. (2008). The global atmospheric circulation on moist isentropes. *Science*, 321(5892):1075–1078.

Pauluis, O., Czaja, A., and Korty, R. (2010a). The global atmospheric circulation in moist isentropic coordinates. *J. Clim.*, 23(11):3077–3093.

Pauluis, O. and Garner, S. (2006). Sensitivity of radiative–convective equilibrium simulations to horizontal resolution. *J. Atmos. Sci.*, 63(7):1910–1923.

Pauluis, O., Shaw, T., and Laliberté, F. (2010b). A kinematic generalization of the transformed eulerian-mean circulation. Submitted for publication to the Journal of Atmospheric Sciences.

Peskin, C. (2002). The immersed boundary method. *Acta Numer.*, 11:479–517.

Pierrehumbert, R. (1998). Lateral mixing as a source of subtropical water vapor. *Geophys. Res. Lett.*, 25(2):151–154.

Pierrehumbert, R. and Swanson, K. (1995). Baroclinic instability. *Annual Review of Fluid Mechanics*, 27(1):419–467.

Plumb, R. and Ferrari, R. (2005). Transformed eulerian-mean theory. part i: Nonquasigeostrophic theory for eddies on a zonal-mean flow. *J. Phys. Oceanogr.*, 35(2):165–174.

Polvani, L. and Esler, J. (2007). Transport and mixing of chemical air masses in idealized baroclinic life cycles. *J. Geophys. Res.*, 112(D23):D23102.

Polvani, L., Scott, R., and Thomas, S. (2004). Numerically converged solutions of the global primitive equations for testing the dynamical core of atmospheric gcms. *Mon. Wea. Rev.*, 132:2539–2552.

Roma, A., Peskin, C., and Berger, M. (1999). An adaptive version of the immersed boundary method. *J. Comput. Phys.*, 153(2):509–534.

Schneider, T., O'Gorman, P., and Levine, X. (2010). Water vapor and the dynamics of climate changes. *Rev. Geophys.*, 48(3):RG3001.

Schneider, T., Smith, K., O'Gorman, P., and Walker, C. (2006). A climatology of tropospheric zonal-mean water vapor fields and fluxes in isentropic coordinates. *J. Clim.*, 19(22):5918–5933.

Simmons, A. and Hoskins, B. (1977). Baroclinic instability on the sphere: Solutions with a more realistic tropopause. *J. Atmos. Sci.*, 34(4):581–588.

Simpson, G. C. (1929). On further studies in terrestrial-radiation. *Quart. J. Roy. Meteor. Soc.*, 55(229):73–79.

Stevens, B. (2005). Atmospheric moist convection. *Annu. Rev. Earth Plan. Sci.*, pages 605–643.

Stone, E., Randel, W., and Stanford, J. (1999). Transport of passive tracers in baroclinic wave life cycles. *J. Atmos. Sci.*, 56(10):1364–1381.

Teng, H., Washington, W., and Meehl, G. (2008). Interannual variations and future change of wintertime extratropical cyclone activity over north america in ccsm3. *Clim. Dynam.*, 30(7):673–686.

Thorncroft, C., Hoskins, B., and McIntyre, M. (1993). Two paradigms of baroclinic-wave life-cycle behaviour. *Quart. J. Roy. Meteor. Soc.*, 119(509):17–55.

Thorpe, A. and Emanuel, K. (1985). Frontogenesis in the presence of small stability to slantwise convection. *J. Atmos. Sci.*, 42(17):1809–1824.

Uppala, S., KÅllberg, P., Simmons, A., Andrae, U., Bechtold, V. D. C., Fiorino, M., Gibson, J., Haseler, J., Hernandez, A., Kelly, G., Li, X., Onogi, K., Saarinen, S., Sokka, N., Allan, R., Andersson, E., Arpe, K., Balmaseda, M., Beljaars, A., Berg, L. V. D., Bidlot, J., Bormann, N., Caires, S., Chevallier, F., Dethof, A., Dragosavac, M., Fisher, M., Fuentes, M., Hagemann, S., Hólm, E., Hoskins, B., Isaksen, L., Janssen, P., Jenne, R., Mcnally, A., Mahfouf, J., Morcrette, J.-J., Rayner, N., Saunders, R., Simon, P., Sterl, A., Trenberth, K., Untch, A., Vasiljevic, D., Viterbo, P., and Woollen, J. (2005). The era-40 re-analysis. *Quart. J. Roy. Meteor. Soc.*, 131(612):2961–3012.

Vallis, G. K. (2006). *Atmospheric and Oceanic Fluid Dynamics*. Cambridge University Press.

Vecchi, G. and Soden, B. (2007). Global warming and the weakening of the tropical circulation. *J. Clim.*, 20(17):4316–4340.

Whitaker, J. and Davis, C. (1994). Cyclogenesis in a saturated environment. *J. Atmos. Sci.*, 51(6):889–908.

Wu, Y., Ting, M., Seager, R., Huang, H.-P., and Cane, M. (2010). *Changes in storm tracks and energy transports in a warmer climate simulated by the GFDL CM2.1 model*. Clim. Dynam. Springer–Verlag.

Yang, H. and Pierrehumbert, R. (1994). Production of dry air by isentropic mixing. *J. Atmos. Sci.*, 51(23):3437–3454.